Searches for Beyond Standard Model Higgs Bosons in *pp* collisions at $\sqrt{s} = 8$ and 13 TeV with the ATLAS detector

Pedro H. Sales de Bruin

A dissertation submitted in partial fulfillment of the
requirements for the degree of

Doctor of Philosophy

University of Washington

2016

Reading Committee:

Anna Goussiou, Chair

Ann Nelson

Shih-Chieh Hsu

Program Authorized to Offer Degree:
Department of Physics

University of Washington

Abstract

Searches for Beyond Standard Model Higgs Bosons in *pp* collisions at $\sqrt{s} = 8$ and 13 TeV
with the ATLAS detector

Pedro H. Sales de Bruin

Chair of the Supervisory Committee:
Professor Anna Goussiou
Department of Physics

The searches for a Beyond Standard Model (BSM) heavy CP-odd Higgs boson A decaying to Zh in the context of two-Higgs-doublet models (2HDM), and Minimal Supersymmetric Standard Model (MSSM) neutral Higgs bosons H/A decaying to a tau pair are presented. The search for the heavy CP-odd Higgs boson, A, is conducted through the $A \rightarrow Zh \rightarrow \ell\ell\tau_{lep}\tau_{had}$ decay channel using 20.3 fb^{-1} of proton-proton collision data collected by the ATLAS detector at a center-of-mass of 8 TeV. The search for the neutral MSSM H/A decaying to a tau pair in the $\tau_{lep}\tau_{had}$ b-veto final state is done using 3.2 fb^{-1} of proton-proton collision data recorded by the ATLAS detector at a center-of-mass of 13 TeV. The observed data agrees with the Standard Model background prediction, and upper limits are set on cross-section times branching ratio of neutral BSM Higgs bosons.

TABLE OF CONTENTS

Page

LIST OF FIGURES

Figure Number Page

LIST OF TABLES

ACKNOWLEDGMENTS

I would first like to thank my advisor, Anna Goussiou, who provided me with precious guidance and support throughout my PhD. Special thanks also to Nikolaos Rompotis, whose constant help has been instrumental in all of the achievements of my graduate career. Many thanks to my colleagues in the Higgs and tau groups, with whom I have had the great fortune of collaborating with. Sincere thanks to my parents, not only for making this possible but also for showing me the value of scientific thought. Lastly, thanks to my wife, Emily, whose constant support helped me endure the stresses of graduate life.

DEDICATION

To my grandparents, Henricus and Iêda.

Chapter 1

INTRODUCTION

The Standard Model (SM) is currently the most complete theory of fundamental particles and their interactions. Despite its success, the SM fails to explain, among other things, the presence of Dark Matter [1], gravity [2] and the matter-antimatter asymmetry of the universe [3], and suffers from severe fine-tuning of some of its parameters [4]. Therefore, it must be extended with a compatible "Beyond Standard Model" (BSM) theory if we are to have a complete and unified description of particle physics.

On July 4th, 2012, the observation of a new particle was announced by the ATLAS and CMS experiments [5, 6]. Subsequent studies done in both ATLAS and CMS have found that the new particle is compatible with the SM Higgs boson, h [7, 8, 9, 10]. The discovery was realized by detecting a 125 GeV resonance in the invariant mass spectrum of diphoton, shown in Figure 1.1, as well as WW and ZZ events. Strong supporting evidence has also been found in the $h \to \tau\tau$ channel [11]. Searches in the $h \to bb$ channel have also been carried out [12, 13], but the large multijet background at the LHC have hindered a discovery in that channel.

The existence of the Higgs field was first predicted in 1964, almost 50 years prior to its discovery, by P. Higgs [14, 15, 16], F. Englert and R. Brout [17], and G. Guralnik, C.R. Hagen and T. Kibble [18]. Their influential work showed that adding a doublet of complex scalar fields leads to the spontaneous breaking of the gauge symmetry of the SM electroweak sector, which in turn explains why the W and Z vector bosons are massive particles. The process of electroweak symmetry breaking (EWSB) through the addition of this Higgs field is known as the "Higgs Mechanism". The observation of the h boson was the last fundamental particle required in the construction of the SM and has become a crowning achievement of

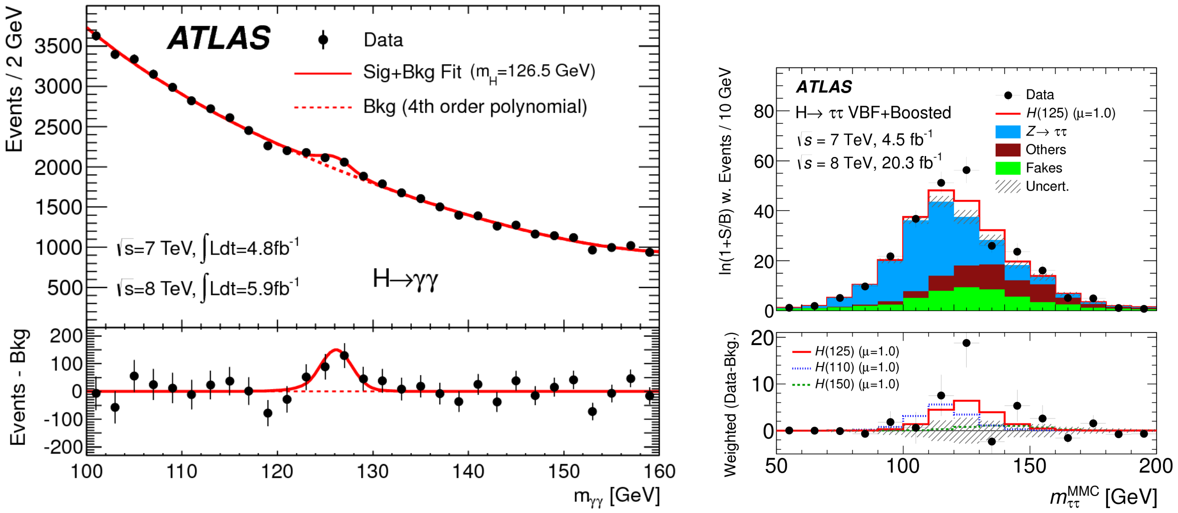

(a)

(b)

Figure 1.1: The reconstructed invariant mass distribution of $\gamma\gamma$ (a) and $\tau\tau$ (b) events, from References [5] and [11], respectively. The solid red line is a fit to the observed data using a SM Higgs signal hypothesis. Events in (b) are weighted according to a measure of the likelihood they correspond to a signal event, as determined by a multivariate classifier.

decades of work from particle theorists and experimentalists.

As we will see in Chapter 2, the Higgs boson has radiative corrections that tend to make it far heavier than its observed mass, necessitating heavy fine-tuning of its parameters to give the observed mass. This is called the naturalness problem. An early proposed solution to it was the imposition of an additional symmetry to the SM called Supersymmetry [19, 20, 21]. The Minimal Supersymmetric Standard Model (MSSM) is a popular theory because it achieves supersymmetry through minimal modifications to the SM [22]. It belongs to a larger class of models that have an extended Higgs sector containing an additional Higgs doublet, named Two-Higgs-Doublet Models (2HDM) [23]. In 2HDM there are five predicted Higgs bosons: two that are CP-even, h and H, one that is CP-odd, A, and two charged scalars, $H^{\pm}$. In this thesis, two BSM Higgs searches are described: the search for a heavy CP-odd neutral Higgs boson, A, decaying to Zh, and the search for heavy neutral MSSM Higgs bosons decaying to a tau pair. The $A \to Zh$ search is conducted in the $Z \to \ell\ell$, $h \to \tau_{lep}\tau_{had}$

final state ($\ell = e,\mu$), where τ_{lep} and τ_{had} denote leptonically and hadronically decaying taus, respectively. The MSSM $H/A \rightarrow \tau\tau$ search is also done in the $\tau_{lep}\tau_{had}$ final state and focuses on events without b-tagged jets.

The layout of this document is as follows: Chapter 2 contains a description of the Standard Model, as well as the BSM theories relevant to the work, Chapter 3 provides details on the Large Hadron Collider and the ATLAS detector, Chapter 4 describes the $A \rightarrow Zh \rightarrow \ell\ell\tau_{lep}\tau_{had}$ analysis, Chapter 5 describes the MSSM $H/A \rightarrow \tau_{lep}\tau_{had}$ analysis, and Chapter 6 contains a short summary. The analysis chapters are further subdivided into subsections concerning (in order of appearance): the data and simulated samples used, the techniques developed by ATLAS to reconstruct particle objects, the event selection criteria used to maximize a potential signal detection, the methods used to describe the background events passing our selection, and finally the search results. Additionally, Appendices A and B describe the τ_{had} identification algorithm and the statistical procedure used to interpret the results.

Chapter 2

THEORY

2.1 The Standard Model

The Standard Model (SM) of particle physics is the prevailing theory of particles and their interactions. It successfully explains and predicts many phenomena of particles physics, a large fraction of which have been experimentally confirmed. The SM is essentially a unified theoretical description of three different forces of nature: the strong force, the weak force, and electromagnetism. The gravitational force has not yet been explained in the context of the SM.

It is illuminating to present the fundamental aspects of the SM in terms of its particle content. All fundamental particles described in the SM can be categorized into the following groups: particles with half-integer spin called fermions (which are divided into leptons and quarks), and particles with integer spin called bosons. There are six types of quarks: the 1st generation *up* (u) and *down* (d) , the 2nd generation *charm* (c) and *strange* (s), and the 3rd generation *top* (t) and *bottom* (b). The lepton group is also composed of three generations: electrons (e), muons (μ), taus (τ), and their respective neutrinos (ν_e, ν_μ, ν_τ). All fundamental particles are also predicted to have antiparticles with opposite electrical charge, effectively doubling the particle content of the SM.

Formally, SM interactions are described by gauge-invariant quantum fields, meaning they are invariant under a continuous group of local transformations. The quanta of the gauge fields are the gauge bosons. These are the photon, γ , the vector bosons W and Z, the gluons g, and finally the Higgs boson, h. For a summary of the SM particles, see Figure 2.1.

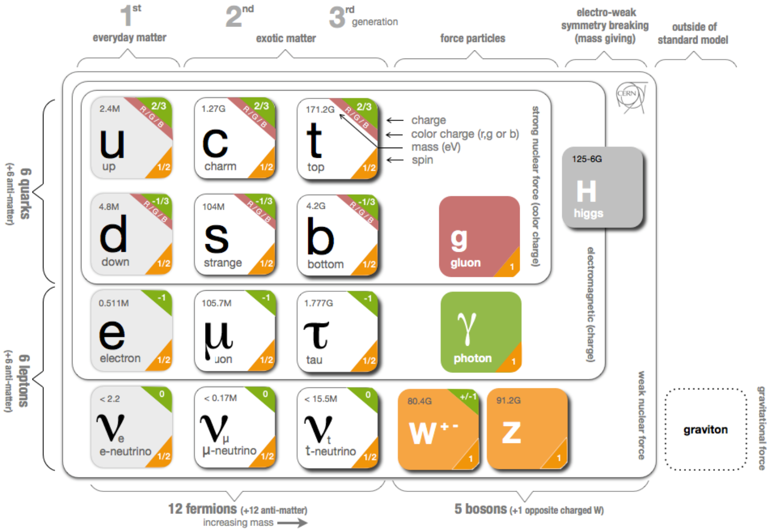

Figure 2.1: The Standard Model of elementary particles.

2.1.1 *The Strong Sector*

The description of strong interactions in the SM is done by Quantum Chromodynamics (QCD), a gauge theory with SU(3) symmetry [24]. The generators of the fundamental representation of SU(3) are the traceless and hermitian matrices, λ^a_{ij}, also known as the Gell-Mann matrices. Only quarks and gluons interact via the strong force. The QCD lagrangian is given by

$$\mathcal{L} = \bar{\psi}^i_q (i\gamma^\mu)(D_\mu)_{ij}\psi^j_q - \frac{1}{4}G^a_{\mu\nu}G^{\mu\nu}_a, \tag{2.1}$$

where ψ^i_q is the field of a quark q with color index i, $\bar{\psi}^i_q \equiv \psi^\dagger\gamma^0$ is its Dirac adjoint, γ^μ are the Dirac matrices, $G^a_{\mu\nu}$ is the gluon field-strength tensor, and a is the color charge ($a = 1$,...,8). The term D_μ is the covariant derivative that maintains gauge invariance under SU(3), given by

$$(D_\mu)_{ij} = \delta_{ij}\partial_\mu - \frac{1}{2}ig_s\lambda^a_{ij}G^a_\mu, \tag{2.2}$$

where g_s is the coupling constant of the strong force and G^a_μ is the field of a gluon with color a.

An interesting property of QCD is how the coupling strength parameter α_s changes (or "runs") with the energy scale (Q), a dependency given by the *beta function*:

$$\beta(\alpha_s) \equiv Q^2 \frac{\partial \alpha_s}{\partial Q^2} = -\alpha_s^2 (b_0 + b_1 \alpha_s + b_2 \alpha_s^2 + ...), \tag{2.3}$$

where b_0, b_1... are the coefficients of processes at leading order (LO), next-to-leading order (NLO), and so on. The b_i parameters depend only on the number of quark states accessible, and the LO and NLO terms are

$$b_0 = \frac{33 - 2n_f}{12\pi} \tag{2.4}$$

and

$$b_1 = \frac{153 - 19n_f}{24\pi^2}, \tag{2.5}$$

where n_f is the number of quark states accessible at the energy scale Q. Note that if $n_f < 16$, then b_0 is positive such that the coupling strength α_S gets progressively smaller as we go to higher energies. This property of QCD is called *asymptotic freedom*. Opposite to this effect is the fact that the interaction energy between quarks does not vanish at large distances but continues to grow, so that it is energetically more favorable for the QCD potential to generate new quark-antiquark pairs than to allow indefinite separation of color-charged particles. This leads to the phenomenon of *confinement*, where quarks and gluons cannot be isolated, but instead decay into collimated showers of colorless hadrons, which are composite particles made of quarks. This process is called hadronization. The top quark is an exception to this rule because it may decay before it hadronizes. The particle system originating from these hadronic decays is typically referred to as *jets*.

2.1.2 The Electroweak Sector

In modern particle theory, electromagnetism and the weak force are unified under the Glashow-Weinberg-Salam (GSW) model [25]. The gauge-covariant formulation of the GSW model is based on the symmetry group SU(2)×U(1). The generator of the U(1) group is the weak hypercharge operator, $\hat{Y}$, and the generators of the SU(2) group are the weak isospin operators, $\hat{\boldsymbol{T}}$. Leptons are represented according to their helicity: right-handed leptons are isospin singlets ($T = 0$), while left-handed leptons are isospin doublets ($T = \frac{1}{2}$, $T_3 = \pm\frac{1}{2}$):

$$L_\ell = \frac{1-\gamma_5}{2}\begin{pmatrix}\psi_{\nu_\ell}\\ \psi_\ell\end{pmatrix},\ R_\ell = \frac{1+\gamma_5}{2}\psi_\ell. \tag{2.6}$$

Requiring the invariance of the theory with respect to gauge transformations leads to the introduction of two isovector fields: the isospin triplet $\boldsymbol{A}_\mu$ and the isospin singlet B_μ. The lagrangian density of the electroweak sector can then be written as

$$\mathcal{L}_{\text{EW}} = \bar{L}_\ell\gamma^\mu iD_\mu L_\ell + \bar{R}_\ell\gamma^\mu iD_\mu R_\ell - \frac{1}{4}\boldsymbol{F}_{\mu\nu}\cdot\boldsymbol{F}^{\mu\nu} - \frac{1}{4}B_{\mu\nu}B^{\mu\nu}. \tag{2.7}$$

In the equation above, γ^μ are the Dirac matrices, and $\boldsymbol{F}_{\mu\nu} = \partial_\mu\boldsymbol{A}_\nu - \partial_\nu\boldsymbol{A}_\mu + g\boldsymbol{A}_\mu\times\boldsymbol{A}_\nu$ and $B_{\mu\nu} = \partial_\mu B_\nu - \partial_\nu B_\mu$ are the field-strength tensors. The covariant derivative is introduced so that the kinetic terms in Equation 2.7 are gauge invariant. It is given by

$$D_\mu = \partial_\mu - ig\hat{\boldsymbol{T}}\cdot\boldsymbol{A}_\mu - i\frac{g'}{2}\hat{Y}B_\mu, \tag{2.8}$$

where g and g' are the coupling strengths to $\boldsymbol{A}_\mu$ and B_μ. The fields for the the photon, $A^{(\gamma)}$ (not to be confused with the isotriplet $\boldsymbol{A}_\mu$ field), and for the physical bosons of the weak interaction, Z and $W^\pm$, are a mixture of $\boldsymbol{A}_\mu$ and B_μ according to the Weinberg angle θ:

$$A^{(\gamma)}_\mu = \cos(\theta)B_\mu + \sin(\theta)A^3_\mu, \tag{2.9}$$

$$Z_\mu = -\sin(\theta)B_\mu + \cos(\theta)A^3_\mu \tag{2.10}$$

and

$$W^\pm_\mu = \frac{1}{\sqrt{2}}(A^1_\mu \mp iA^2_\mu). \tag{2.11}$$

2.1.3 The Higgs Mechanism

Up to now, the electroweak gauge bosons γ, Z and $W^\pm$ have been treated as massless in order to preserve the gauge symmetry. However, the weak force is known to have a very short range, and thus large masses for the particles that propagate it. The solution to this problem is to add a new field that breaks the SU$(2)_L\times$ U$(1)_Y$ gauge symmetry of the GSW model and gives mass to the vector bosons dynamically. This process is known as the Higgs mechanism.

Consider the Higgs field, a weak isospin doublet ($T = \frac{1}{2}$, $T_3 = \pm\frac{1}{2}$) of complex scalar fields

$$\Phi = \begin{pmatrix} \phi^+ \\ \phi^0 \end{pmatrix}, \tag{2.12}$$

where $\phi^{+(0)}$ has a positive (neutral) electric charge and hypercharge $Y = 1$. The Higgs lagrangian is then

$$\mathcal{L}_{\text{Higgs}} = |D_\mu\Phi|^2 - U(\Phi), \tag{2.13}$$

where D_μ is the covariant derivative of Equation 2.8, and the energy potential $U(\Phi)$ is given by

$$U(\Phi) = -\mu^2|\Phi|^2 + h\Phi^4, \tag{2.14}$$

where $\mu^2 > 0$ and $h > 0$. The Higgs potential above has a "Mexican hat" shape, as shown in Figure 2.2. An interesting property of such a potential is that the minima occur for non-zero values of the field. Thus, the Higgs field is said to have a positive *vacuum expectation value* (vev). Without restricting generality, we can set the top isospin component to zero by a suitable gauge choice. In this gauge, the Higgs doublet is given by

$$\phi' = \frac{1}{\sqrt{2}}(\lambda + \chi(x)) \begin{pmatrix} 0 \\ 1 \end{pmatrix}, \tag{2.15}$$

where $\lambda = \sqrt{\frac{\mu^2}{h}}$ is the non-zero vev of the field and $\chi(x)$ are local deviations from it. Thus, Equation 2.14 becomes (dropping constant terms):

$$V(\chi) = h\lambda^2\chi^2 + h\lambda\chi^3 + \frac{h}{4}\chi^4. \tag{2.16}$$

The field $\chi(x)$ corresponds to excitations of the field around the vev, and represents a new boson called the Higgs boson. Equation 2.16 shows the Higgs boson has mass ($m_h = \sqrt{2h\lambda^2}$)

and is self-interacting. The Higgs field vev can be obtained from Fermi's constant and is, approximately, 246 GeV. The electroweak scale is commonly associated with this value.

The lepton masses are generated dynamically by their interaction with the Higgs field:

$$\mathcal{L}_{\ell-\mathrm{Higgs}} = -\sqrt{2}m_\ell(\bar{R}_\ell \Phi^\dagger L_\ell + \bar{L}_\ell \Phi R_\ell), \tag{2.17}$$

where $m_\ell = f_\ell/\lambda$ is the charged lepton mass. The relation shown in Equation 2.17 is called the *Yukawa* interaction for leptons. The Yukawa interaction is a general interaction between a scalar field and a Dirac (fermionic) field, so that there is a corresponding Yukawa term for quarks.

With the addition of this Higgs sector, the combined $\mathcal{L}_{\mathrm{QCD}} + \mathcal{L}_{\mathrm{EW}} + \mathcal{L}_{\mathrm{Higgs}}$ lagrangian becomes

$$\begin{aligned}\mathcal{L}_{\mathrm{SM}} = {} & \bar{\psi}_q^i \gamma^\mu i (D_\mu)_{ij} \psi_q^j - m_q \bar{\psi}_q^i \psi_{qi} - \frac{1}{4} G^a_{\mu\nu} G_a^{\mu\nu} \\ & + \bar{L}_\ell \gamma^\mu i D_\mu L_\ell + \bar{R}_\ell \gamma^\mu i D_\mu R_\ell - \frac{1}{4} \boldsymbol{F}_{\mu\nu} \cdot \boldsymbol{F}^{\mu\nu} - \frac{1}{4} B_{\mu\nu} B^{\mu\nu} \\ & + |D_\mu \Phi|^2 + \mu^2 |\Phi|^2 - h\Phi^4 \end{aligned} \tag{2.18}$$

Using the perturbative expansion of Equation 2.15, combined with Equation 2.8, this becomes

$$\begin{aligned}\mathcal{L}_{\mathrm{SM}} = {} & \sum_q [\bar{\psi}_q^i (i\gamma^\mu)(\delta_{ij}\partial_\mu - \frac{1}{2} i g_s \lambda^a_{ij} G^a_\mu) \psi_q^j - f_q \bar{\psi}_q^i \psi_{qi} (\lambda + \chi)] - \frac{1}{4} G^a_{\mu\nu} G_a^{\mu\nu} \\ & - \sum_q i \left[g \bar{\psi}^L_{qi} \gamma^\mu \left(\frac{g}{6} B_\mu + \frac{g'}{2} \boldsymbol{A}_\mu \right) \psi^L_{qi} - i g \bar{\psi}^R_{qi} \gamma^\mu Y^{\mathrm{R}} g B_\mu \psi^R_{qi} \right] \\ & - \frac{1}{4} \boldsymbol{F}_{\mu\nu} \cdot \boldsymbol{F}^{\mu\nu} - \frac{1}{4} B_{\mu\nu} B^{\mu\nu} - e \sum_\ell \bar{\psi}_\ell \gamma^\mu \psi_\ell A^{(\gamma)}_\mu \\ & + \sum_\ell i [\bar{\psi}_{\nu_\ell} \gamma^\mu \frac{1}{2} (1 - \gamma_5) \partial_\mu \psi_{\nu_\ell} + i \bar{\psi}_\ell \gamma^\mu \partial_\mu \psi_\ell - f_\ell \bar{\psi}_\ell \psi_\ell (\lambda + \chi)] \\ & + \frac{g}{2\sqrt{2}} \sum_\ell [\bar{\psi}_\ell \gamma^\mu (1 - \gamma_5) \psi_{\nu_\ell} W^-_\mu + \bar{\psi}_{\nu\ell} \gamma^\mu (1 - \gamma_5) \psi_\ell W^+_\mu] \\ & + \frac{6}{4 \cos\theta} \sum_\ell [\bar{\psi}_{\nu_\ell} \gamma^\mu (1 - \gamma_5) \psi_{\nu_\ell} - \bar{\psi}_\ell \gamma^\mu (g'_V - \gamma_5) \psi_\ell] Z_\mu \\ & + \frac{h\lambda^4}{4} + \frac{1}{2} (\partial_\mu \chi)^2 - h \lambda^2 \chi^2 - h \chi^2 (\lambda\chi + \frac{1}{4} \chi^2) + \frac{g^2}{8} (2 W^+_\mu W^{-\mu} + \frac{Z_\mu Z^\mu}{\cos^2\theta}) (\lambda + \chi)^2, \end{aligned} \tag{2.19}$$

where ψ_q^{L} and ψ_q^{R} are the left-handed quark doublets and right-handed quark singlets, $Y^{\mathrm{R}} = \frac{4}{3}\,(-\frac{2}{3})$ is the hypercharge of *up*-type (*down*-type) right-handed quarks, $e = g\sin\theta$, $f_\ell = m_\ell/\lambda$ is the coupling of the leptons to the Higgs field, $f_q = m_q/\lambda$ the Higgs coupling to quarks, and $g'_V = 1 - \sin^2\theta$. Notice the coupling of fermions to the Higgs field scales with fermion mass. The last term contains the mass terms for the $W^\pm$ and Z bosons, given by

$$M_W = \frac{g\lambda}{2} \tag{2.20}$$

and

$$M_Z = \frac{M_W}{\cos\theta} \tag{2.21}$$

One last remark is that the Higgs field does not couple with the electromagnetic field $A_\mu^{(\gamma)}$, which leads to the desired result of the photon remaining massless.

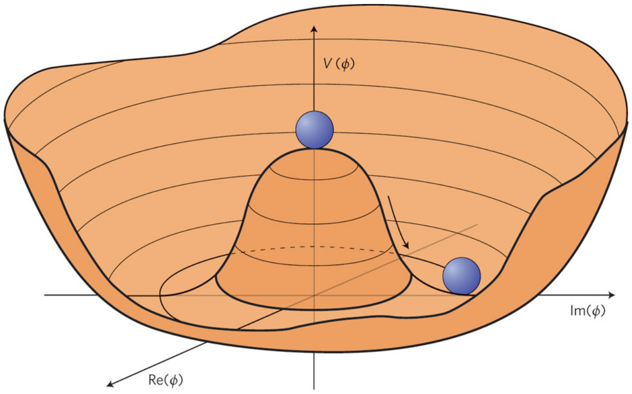

Figure 2.2: The Higgs potential with its non-zero vacuum expectation value. The blue spheres denote excitations of the field around the vev, corresponding to the physical Higgs boson.

2.2 *Two-Higgs-Doublet Models*

The Higgs sector presented in the previous section has the simplest possible structure that solves the issue of massless electroweak gauge bosons, with just a single SU(2) doublet. However, there are many reasons to consider more complex structures.

One of them is the so-called *Hierarchy Problem*, the question of why the electroweak scale is so much lower than the Planck scale (10^{19} GeV). Alternatively, it can be formulated as why is the Higgs mass 125 GeV if the quantum corrections from the Higgs coupling to heavy fermions are so great. For example, the one-loop diagrams from the interaction of the Higgs with fermions will give a correction that goes quadratically with the scale of new physics. If this scale were to be the Planck scale, then the corrections would be $\Delta m_h^2 \sim 10^{38}$ GeV, more than 30 orders of magnitute higher than the physical Higgs mass. This is fixed only by the *unnatural*, fine-tuned solution where the bare mass of the Higgs is also on the order of the Planck scale, leading to large cancellations of these radiative corrections. A more natural way to explain the low value of the Higgs mass is to assume there is a symmetry that stabilizes it, called Supersymmetry (SUSY).

In SUSY, the quantum corrections to the Higgs mass from fermion loops have matching corrections from scalar superpartners that cancel each other, as shown in Figure 2.3. However, the simplest SM-compatible supersymmetric theory requires the addition of a second scalar doublet to the SM Higgs sector, making it part of a larger class of models called two-Higgs-doublet models (2HDM). There are additional motivations for 2HDMs, as they can be used to explain the baryon asymmetry of the universe through new sources of CP-violation [26], and in axion models that solve the strong CP problem [27].

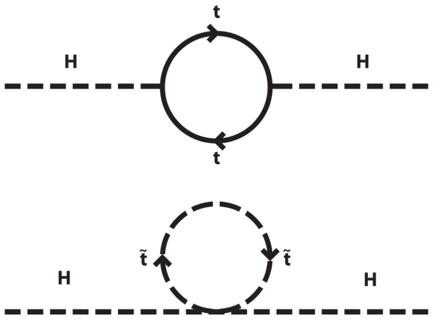

Figure 2.3: One-loop corrections to the Higgs mass from fermions and a supersymmetric scalar.

A general 2HDM scalar sector contains 14 parameters, but for a phenomenologically minded model we can simplify it by requiring it to be CP-conserving and that CP is not spontaneously broken. Another important note on 2HDMs is that, in general, their Yukawa terms allow for flavor-changing neutral currents (FCNC) at tree-level which would not be compatible with experimental observation. However, the FCNC can be naturally suppressed by imposing discrete symmetries to the lagrangian that remove quartic terms with an odd number of either doublet. With those restrictions in mind, the most general 2HDM potential we can build, in terms of the doublets Φ_1 and Φ_2, is

$$\begin{aligned} V = {} & m_{11}^2\Phi_1^\dagger\Phi_1 + m_{22}^2\Phi_2^\dagger\Phi_2 - m_{12}^2(\Phi_1^\dagger\Phi_2 + \Phi_2^\dagger\Phi_1) + \frac{\lambda_1}{2}(\Phi_1^\dagger\Phi_1)^2 + \frac{\lambda_2}{2}(\Phi_2^\dagger\Phi_2)^2 \\ & + \lambda_3\Phi_1^\dagger\Phi_1\Phi_2^\dagger\Phi_2 + \lambda_4\Phi_1^\dagger\Phi_2\Phi_2^\dagger\Phi_1 + \frac{\lambda_5}{2}\left[(\Phi_1^\dagger\Phi_2)^2 + (\Phi_2^\dagger\Phi_1)^2\right]. \end{aligned} \tag{2.22}$$

We can minimize V just as we did in Equation 2.15, obtaining

$$\phi_1' = \frac{v_1}{\sqrt{2}}\begin{pmatrix} 0 \\ 1 \end{pmatrix},\ \phi_2' = \frac{v_2}{\sqrt{2}}\begin{pmatrix} 0 \\ 1 \end{pmatrix}, \tag{2.23}$$

where v_1 and v_2 are the vev's of the two scalar fields. Written as expansions around their equilibria, the two doublets are

$$\phi_a = \begin{pmatrix} \phi_a^+ \\ (v_a + \rho_a + i\eta_a)/\sqrt{2} \end{pmatrix},\ a\text{=}1,\ 2. \tag{2.24}$$

Since we now have two complex scalar doublets, there are a total of eight fields. However, just as in the SM, three of them are replaced by the $W^\pm$ and Z fields, leaving five Higgs fields. Using Equation 2.24 in 2.22, three separate mass terms in the 2HDM lagrangian are obtained

$$\begin{aligned} \mathcal{L}_{\phi^\pm} &= m_{12}^2 - (\lambda_4 + \lambda_5)v_1v_2 \begin{pmatrix} \phi_1^- & \phi_2^- \end{pmatrix} \begin{pmatrix} \frac{v_2}{v_1} & -1 \\ -1 & \frac{v_1}{v_2} \end{pmatrix} \begin{pmatrix} \phi_1^+ \\ \phi_2^+ \end{pmatrix}, \\ \mathcal{L}_\eta &= \frac{m_A^2}{v_1^2 + v_2^2} \begin{pmatrix} \eta_1 & \eta_2 \end{pmatrix} \begin{pmatrix} v_2^2 & -v_1v_2 \\ -v_1v_2 & v_1^2 \end{pmatrix} \begin{pmatrix} \eta_1 \\ \eta_2 \end{pmatrix}, \\ \mathcal{L}_\rho &= -\begin{pmatrix} \rho_1 & \rho_2 \end{pmatrix} \begin{pmatrix} m_{12}^2\frac{v_2}{v_1} + \lambda_1v_1^2 & -m_{12}^2 + \lambda_{345}v_1v_2 \\ -m_{12}^2 + \lambda_{345}v_1v_2 & m_{12}^2\frac{v_1}{v_2} + \lambda_2v_2^2 \end{pmatrix} \begin{pmatrix} \rho_1 \\ \rho_2 \end{pmatrix}, \end{aligned} \tag{2.25}$$

where $\lambda_{345} = \lambda_3 + \lambda_4 + \lambda_5$. The mass matrices for the charged ($\phi^{\pm}$) and pseudoscalars ($\eta_{1,2}$) can be diagonalized by the same angle $\beta \equiv \arctan v_2/v_1$, while the mass matrix for the scalars ($\rho_{1,2}$) is diagonalized by the angle α. Together, α and β will affect the couplings of the Higgs bosons to vector bosons, fermions and each other, and are thus of paramount importance in the phenomenology of a particular 2HDM. The physical fields for the light CP-even, h, heavy CP-even, H, and heavy CP-odd, A, can be written as

$$\begin{aligned} h &= \rho_1 \sin\alpha - \rho_2 \cos\alpha, \\ H &= -\rho_1 \cos\alpha - \rho_2 \sin\alpha, \\ A &= \eta_1 \sin\beta - \eta_2 \cos\beta. \end{aligned} \tag{2.26}$$

The discrete symmetries of the 2HDM lagrangian in Equation 2.22 cause the fermions to couple to the Higgs doublets in specific ways. For models without FCNCs, the different 2HDMs can be categorized as:

- Type-I, where all charged fermions couple only to ϕ_2.
- Type-II, where *up*-type quarks couple to ϕ_2, while *down*-type quarks and charged leptons couple to ϕ_1.
- Lepton-specific, similar to Type-I but has charged leptons coupling to ϕ_1.
- Flipped, similar to Type-II but has charged leptons coupling to ϕ_2.

The couplings of *up* and *down*-type quarks and leptons accross theses types of 2HDMs are summarized in Table 2.1.

2.3 The MSSM

As mentioned before, an important motivation for 2HDMs is the possibility of accounting for naturalness through supersymmetry (SUSY). Supersymmetry states that the SM particles will have supersymmetric partners (spartners) with same quantum numbers, but with spin

	Type-I	Type-II	Lepton-specific	Flipped
y_h^u	$\cos\alpha/\sin\beta$	$\cos\alpha/\sin\beta$	$\cos\alpha/\sin\beta$	$\cos\alpha/\sin\beta$
y_h^d	$\cos\alpha/\sin\beta$	$-\sin\alpha/\cos\beta$	$\cos\alpha/\sin\beta$	$-\sin\alpha/\cos\beta$
y_h^ℓ	$\cos\alpha/\sin\beta$	$-\sin\alpha/\cos\beta$	$-\sin\alpha/\cos\beta$	$\cos\alpha/\sin\beta$
y_h^{VV}	$\sin(\beta-\alpha)$	$\sin(\beta-\alpha)$	$\sin(\beta-\alpha)$	$\sin(\beta-\alpha)$
y_H^u	$\sin\alpha/\sin\beta$	$\sin\alpha/\sin\beta$	$\sin\alpha/\sin\beta$	$\sin\alpha/\sin\beta$
y_H^d	$\sin\alpha/\sin\beta$	$\cos\alpha/\cos\beta$	$\sin\alpha/\sin\beta$	$\cos\alpha/\cos\beta$
y_H^ℓ	$\sin\alpha/\sin\beta$	$\cos\alpha/\cos\beta$	$\cos\alpha/\cos\beta$	$\sin\alpha/\sin\beta$
y_H^{VV}	$\cos(\alpha-\beta)$	$\cos(\alpha-\beta)$	$\cos(\alpha-\beta)$	$\cos(\alpha-\beta)$
y_A^u	$\cot\beta$	$\cot\beta$	$\cot\beta$	$\cot\beta$
y_A^d	$-\cot\beta$	$\tan\beta$	$-\cot\beta$	$\tan\beta$
y_A^ℓ	$-\cot\beta$	$\tan\beta$	$\tan\beta$	$-\cot\beta$
y_A^{VV}	0	0	0	0

Table 2.1: Yukawa couplings of leptons, vector bosons and *up* and *down*-type quarks to the neutral Higgs bosons h, H and A for 2HDMs of type-I and type-II.

that is offset by one half. Particles and their spartners are contained in supermultiplets, made up of a chiral scalar field and a fermionic field. Due to their chirality, two Higgs doublets are required in order for the scalars to couple together in the lagrangian and give the fermions mass. This is also a requirement to avoid introducing chiral anomalies into the theory.

When the symmetry is exact, supersymmetric particles have the same mass as their SM counterparts and all terms in the SUSY lagrangian have predetermined couplings such that the theory has no new adjustable parameter. However, this obviously cannot be the case since new particles with masses equal to their SM partners would have been discovered by now. Thus, there must be a mechanism that breaks the symmetry and pushes the SUSY scale to higher energies, but not so high as to make it yet another unnatural theory. There is currently no completely satisfactory way on how to break SUSY, so a simpler approach is to explicitly add SUSY-breaking parameters to the lagrangian which, together with a few other well-motivated assumptions, lead to a minimal realization of SUSY called the Minimal Supersymmetric Standard Model (MSSM) [22].

The MSSM is a particular case of type-II 2HDM. It has the same gauge symmetry as the SM, i.e. $\mathrm{SU}(3)_C \times \mathrm{SU}(2)_L \times U(1)_Y$. Fermionic superpartners are identified by the letter “s” in front of their names, e.g. *stop*, *stau*, etc., and boson superpartners are identified by appending “ino” to their names. Thus, the gauge bosons superpartners are the bino, the three winos, the eight gluinos and the five higgsinos. The higgsinos and the electroweak partners mix, giving physical mass eigenstates in the two charginos ($\chi^{\pm}_{1,2}$) and four neutralinos ($\chi^{0}_{1,2,3,4}$). To ensure lepton and baryon number conservation in the MSSM, a symmetry is introduced that requires R-parity to be conserved. The R-parity quantum number is defined as

$$R_P = (-1)^{2S+3B+L}, \tag{2.27}$$

where S, B and L are the spin, baryon and lepton quantum numbers, respectively. Due to R-parity conservation, the lightest neutralino will be stable, making it an ideal Dark Matter candidate.

The Higgs sector of the MSSM is very well studied, particularly in the context of the LHC [28, 29]. Because of the necessary introduction of terms that break SUSY into the theory, the general formulation of the MSSM has 105 unknown free parameters, in addition to the SM parameters. However, they can be reduced to just 22 by imposing well motivated constraints, such as requiring no FCNCs at leading order, and that the SUSY-breaking parameters of the theory do not introduce new sources of CP-violation. This 22-parameter set formulation of the MSSM is called the "phenomenological MSSM" (pMSSM) [30], and a description of its parameters is below:

- $\tan(\beta)$: the ratio of the two Higgs doublet vev's;
- m_{H_1} and m_{H_2}: the Higgs mass parameters;
- M_1, M_2, M_3: the bino, wino and gluino mass parameters;
- $m_{\tilde{q}}$, $m_{\tilde{u}_R}$, $m_{\tilde{d}_R}$, $m_{\tilde{l}}$, $m_{\tilde{e}_R}$: the mass parameters for the first two generations of squarks and sleptons;
- A_u, A_d, A_e: the trilinear couplings of the first two generations of squarks and sleptons;
- $m_{\tilde{Q}}$, $m_{\tilde{t}_R}$, $m_{\tilde{b}_R}$, $m_{\tilde{L}}$, $m_{\tilde{\tau}_R}$: the mass parameters of the third generation;
- A_t, A_b, A_τ: the trilinear couplings of the third generation;

It is also interesting to define two parameters that can be written in terms of the above: the stop mixing parameter $X_t \equiv A_t - \mu \cot \beta$, which gives the amount of mixing between left and right-handed stops when computing the stop mass eigenstates, and the SUSY scale $M_S \equiv \sqrt{m_{\tilde{t}_1,\tilde{t}_2}}$ that represents the scale where supersymmetry breaks, usually taken to be around 1 TeV to avoid imposing excessive fine-tuning into the model. The higgsino mass parameter μ is often used when discussing the MSSM Higgs sector, but it is not a free parameter and has its value fixed during electroweak symmetry breaking. It is worth noting that the discovery of the 125 GeV Higgs is still compatible with a large region of the pMSSM parameter space, as shown in Figure 2.4.

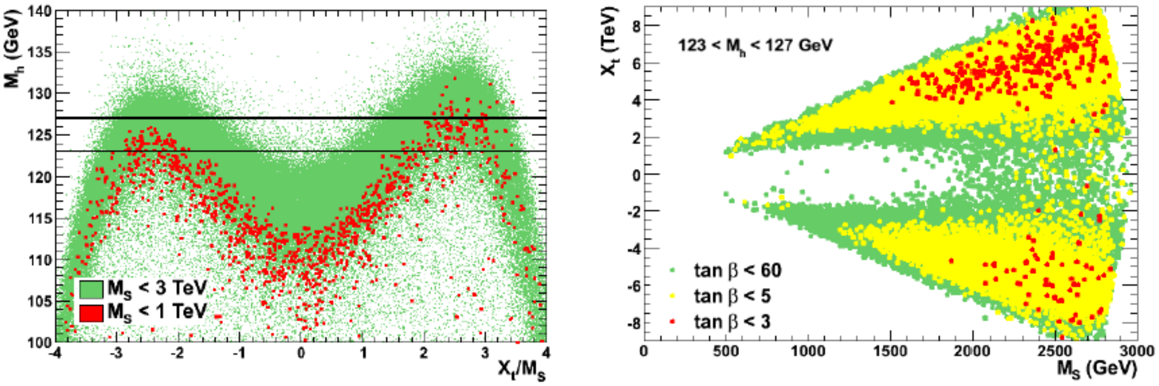

Figure 2.4: The right plot shows the region of the $[X_t, M_S]$ plane of the pMSSM that is compatible with $123 < M_h < 127$ GeV for a range of $\tan\beta$ values, where M_S is the SUSY scale and X_t is the stop mixing parameter. The condition of $X_t/M_S \lesssim 3$ is imposed to avoid a non-viable spectrum of the model. The left plot shows the maximal values of m_h for different X_t/M_S values. Plots from Reference [29].

Though the number of parameters of the pMSSM is much smaller than that of the general formulation of the MSSM, it is still large enough to make interpreting results in the full range of the parameter space cumbersome. Furthermore, at tree-level the MSSM only depends on two parameters, usually taken to be the mass of the CP-odd Higgs boson, m_A, and $\tan\beta$. For example, the masses of the charged and CP-even Higgs bosons (at tree-level) are:

$$\begin{aligned} m_{H^\pm} &= m_A^2 + m_W^2, \\ m_{h,H}^2 &= \frac{1}{2}\left[m_A^2 + m_Z^2 \mp \sqrt{(m_A^2 + m_Z^2)^2 - 4m_A^2 m_Z^2 \cos^2 2\beta}\right], \end{aligned} \tag{2.28}$$

as shown in Figure 2.5. It is therefore convenient to test results against signal hypotheses that are scanned in these leading order terms, while fixing the remaining parameters. This approach leads to the definition of several benchmark scenarios [31]. Figure 2.5 also shows an important feature of the MSSM: the masses of the heavy H, A and $H^\pm$ Higgs bosons are approximately equal for $m_A \gtrsim 130$, and become increasingly degenerate as we proceed to heavier masses. This behavior is observed also for the general FCNC-absent 2HDMs considered in this thesis.

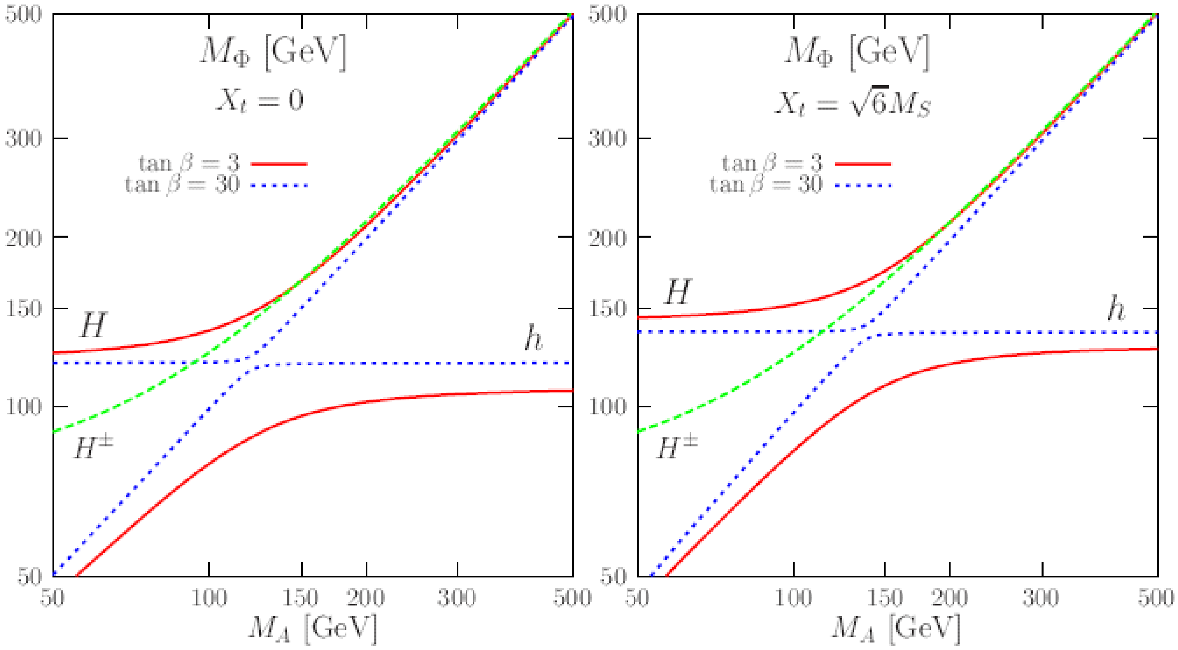

Figure 2.5: Masses of the h, H and $H^\pm$ as a function of the mass of the CP-odd A for stop mixing values $X_t = 0$ (left) and $X_t = \sqrt{6}M_S$ (right). Plots from Reference [28].

A popular MSSM benchmark scenario is the m_h^{max}, where the stop mixing parameter X_t is chosen such as to maximize the mass of the lightest Higgs h, yielding $m_h \sim 135$ GeV for high values of $\tan\beta$ and $M_S \sim 2$ TeV. Though the predicted values of m_h are incompatible with the observation of the 125 GeV h for the majority of the parameter space, the m_h^{max} scenario nevertheless has been extensively studied in the past and remains a reference MSSM benchmark. Another interesting scenario is the m_h^{mod}, which is a modification of the m_h^{max} scenario that gives a lighter Higgs mass prediction consistent with the observed value at the LHC, while maintaining a large region of the tree-level parameter space available. The lower m_h prediction is achieved by reducing the radiative corrections to the Higgs mass from the mixing in the stop sector. The specific term whose reduction gives the correct m_h prediction is X_t/M_S, which can be positive or negative, thus giving two benchmarks called m_h^{mod+} and m_h^{mod-}.

Since the MSSM is a type-II 2HDM, its Higgs sector couplings have already been listed in Table 2.1. Production cross sections for gluon fusion and b-associated production of CP-even (h, H) and CP-odd (A) Higgs bosons at 14 TeV are shown in Figure 2.6. The MSSM search presented in this thesis uses data collected at 13 TeV, and production cross sections for that center of mass energy can be found in Reference [32]. Branching ratios for neutral MSSM Higgs bosons are shown in Figure 2.7.

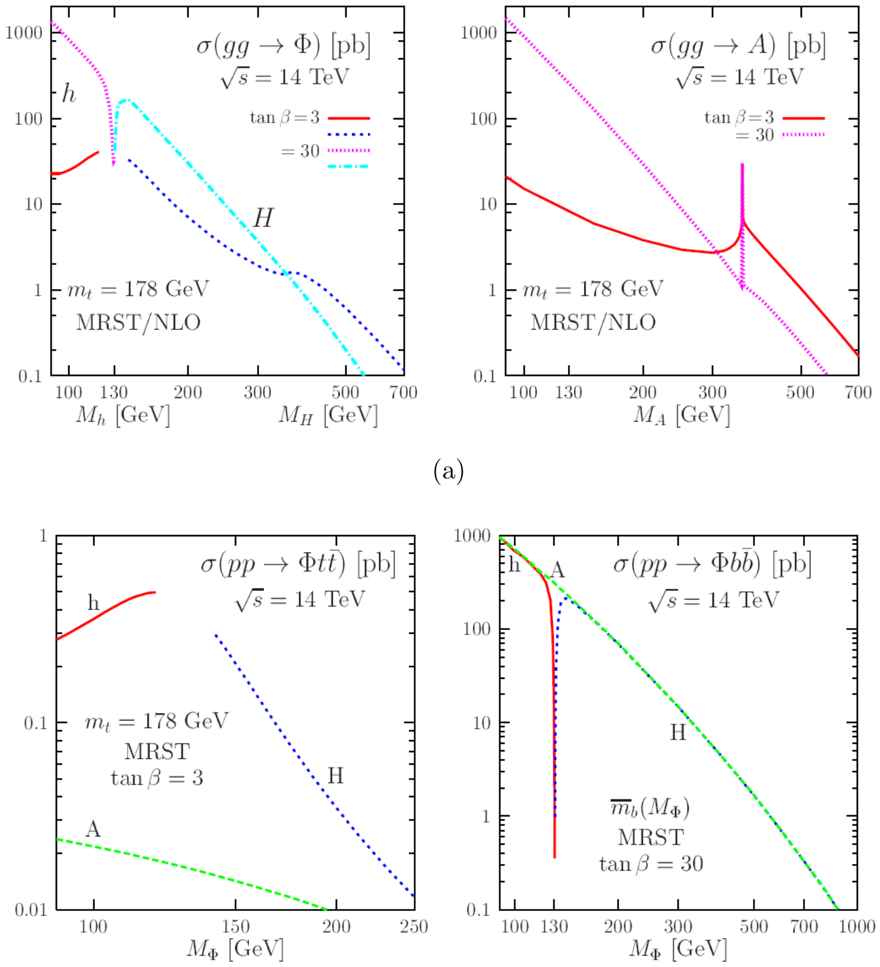

(a)

(b)

Figure 2.6: Production cross sections of neutral Higgs bosons from gluon fusion (a) and b-associated production (b) at 14 TeV. Plots from Reference [28].

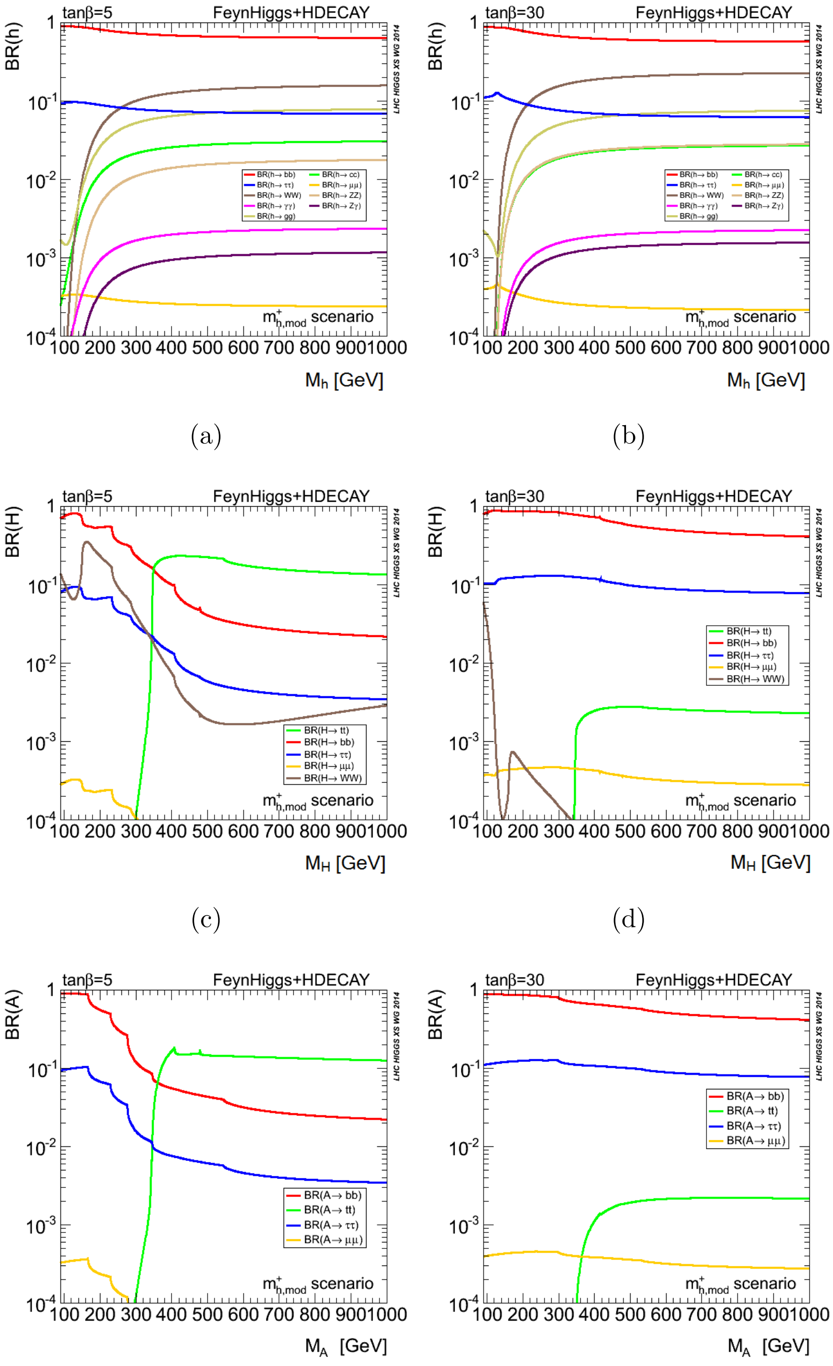

(a) (b)

(c) (d)

(e) (f)

Figure 2.7: Branching ratios of the h, H and A Higgs bosons for $\tan\beta$ values of 5 (left) and 30 (right) in the m_h^{mod+} scenario. Plots from Reference [33].

Chapter 3

APPARATUS

3.1 Overview

The Large Hadron Collider (LHC) is the world's most powerful proton-proton collider [34]. Located at the European Organization for Nuclear Research (CERN) in the outskirts of Geneva, Switzerland, the LHC tunnel is 27 km in circumference and 50 to 175 meters underground. Though the initial design intended for the collision of two 7 GeV proton beams, the current maximum beam energy achieved has been 6.5 GeV. The beams collide at 4 different points in the accelerator ring where the ATLAS, CMS, ALICE and LHCb experiments are housed. Additionally, the TOTEM, LHCf and MoEDAL experiments are also located along the LHC, being near the CMS, ATLAS and LHCb detectors, respectively.

3.2 The Accelerator Complex

The LHC beam injection chain is provided by Linac (abbreviation for linear accelerator), Proton Synchroton Booster (PSB), Proton Synchroton (PS) and Super Proton Synchroton (SPS). At each accelerator step the beam increases in energy: 50 MeV is achieved during the Linac stage, 1.4 GeV at PSB, 25 GeV at PS and finally 450 GeV in the SPS. A schematic overview of the CERN accelerator complex is shown in Figure 3.1.

3.3 LHC

The LHC is divided into 8 alternated straight and arched sectors, as shown in Figure 3.2. The ATLAS experiment is located in the straight section of sector 1, called Point 1, while the CMS experiment is diammetrically opposite in Point 5. Beam injection is done in Points 2 and 8, which also house the ALICE and LHCb experiments, respectively. Points 3 and 7 contain

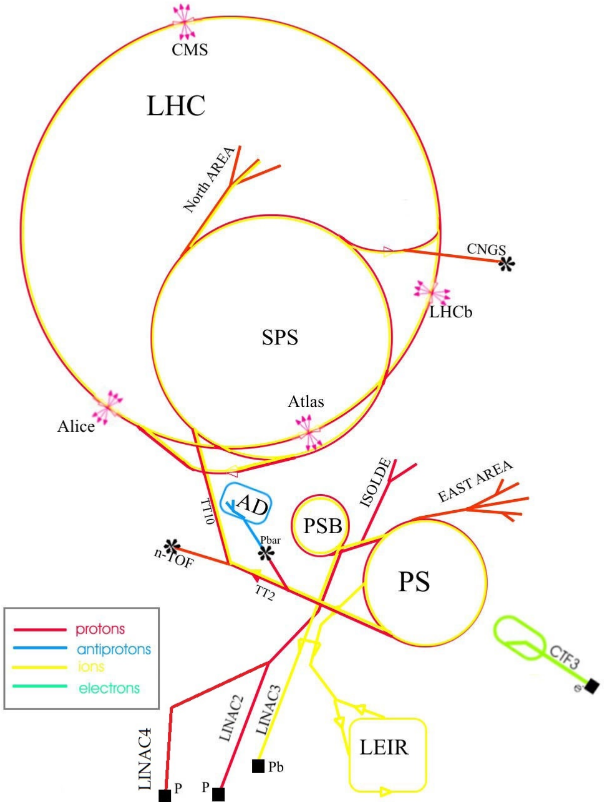

Figure 3.1: A schematic overview of the CERN accelerator complex.

beam collimators, while Point 4 holds two independent Radio Frequency (RF) systems that accelerate each beam. Finally, Point 6 holds the beam dump system, a collection of magnets used to deflect the beam horizontally and vertically out of the LHC ring.

The number of events per second dN/dt of a given process is given by

$$\frac{dN}{dt} = \mathcal{L}_{inst}\sigma, \tag{3.1}$$

where $\mathcal{L}_{inst}$ is the instantaneous luminosity and σ is the cross section of the physical process. The total number of events N is given by integrating the above expression in time. For stable colliding conditions, σ is time-independent such that N is directly proportional to the time-integrated luminosity L. Thus, we have that the number of events of a process $pp \to X$ is given by

$$N_X = L\sigma_{pp\to X}. \tag{3.2}$$

The cross section depends on the colliding and produced particles as well as the center-of-mass energy. The instantaneous luminosity depends only on the beam parameters and is given by

$$\mathcal{L}_{inst} = \frac{N_b^2 n_b f_{rev}\gamma_r}{4\pi\epsilon_n\beta_*}F, \tag{3.3}$$

where the terms in the equation above are:

- the number of bunches in a beam, n_b;
- the number of protons in a bunch, N_b;
- the beam revolution frequency, f_{rev};
- the relativistic factor, γ_r;
- the normalized beam emmitance (a measure of the beam loss in the transverse plane), ϵ_n;
- the beta function at the interaction point, β_*;

- the geometrical reduction factor F, due to the beams approaching each other at a slight angle.

As of August 2016, the peak luminosity achieved at the LHC is $11.6e^{33}\,\mathrm{cm}^{-2}\,\mathrm{s}^{-1}$, with as many as 2076 proton bunches.

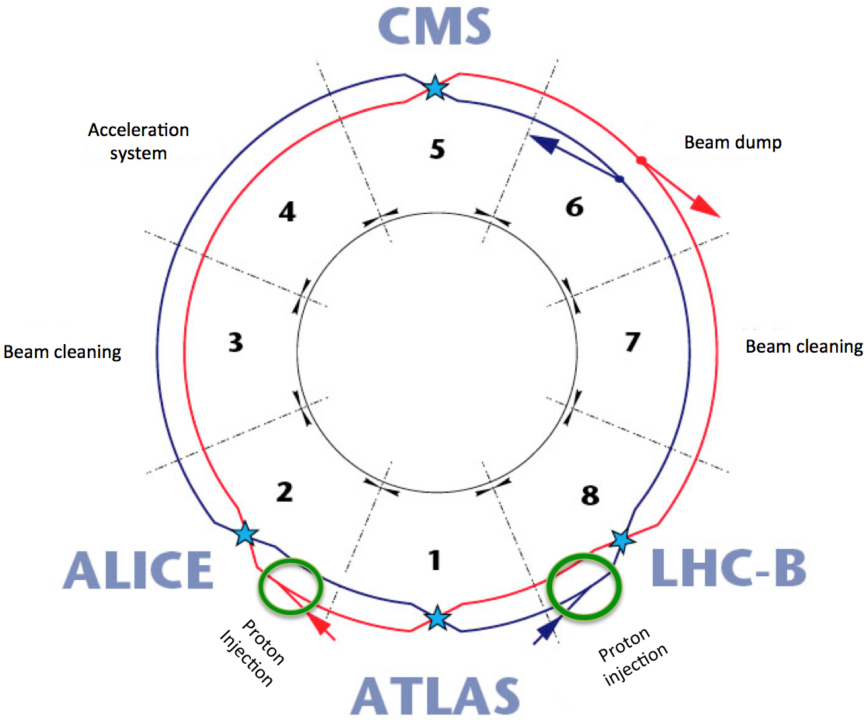

Figure 3.2: The eight sectors of LHC tunnel with the physics experiments depicted.

3.4 ATLAS

The ATLAS detector is a versatile particle detector whose layout is typically broken down into 3 subdetector systems: the Inner Detector, the calorimeter and the Muon Spectrometer [35]. An overview of the ATLAS detector, including its two magnets, is shown in Figure 3.3. To facilitate the detector description and the physical discussion involved, a coordinate system is defined with its origin at the center of the detector where collisions are expected. The z-axis is defined to be along the beam, while the xy plane is vertical with respect to the laboratory frame with the y-axis pointing towards the LHC curvature center. Directions in the xy plane are fully determined by the azimuthal angle ϕ, while the polar angle θ is the angle measured from the beam axis. The latter is often replaced by the pseudorapidity

$$\eta \equiv -\ln(\tan(\theta/2)), \tag{3.4}$$

which is an approximation of the rapidity that is well suited for the high particle energies present at the LHC. The angular distance between two particles is then

$$\Delta R = \sqrt{\Delta\eta^2 + \Delta\phi^2}. \tag{3.5}$$

The detector was designed with the aim of searching for the wide range of phenomena available at the TeV scale. These include not only the (now confirmed) production of the Standard Model Higgs boson, but also tests of QCD, electroweak, flavour physics and BSM processes. As such, several minimal benchmarks must be satisfied by ATLAS:

- fine granularity to discern between overlapping events;
- good track and charge reconstruction;
- good identification, energy and momentum measurements for electromagnetic objects and jets;
- sufficient vertex reconstruction and resolution to allow for proper identification of secondary decays, such as those found in b-jets and τ-leptons;

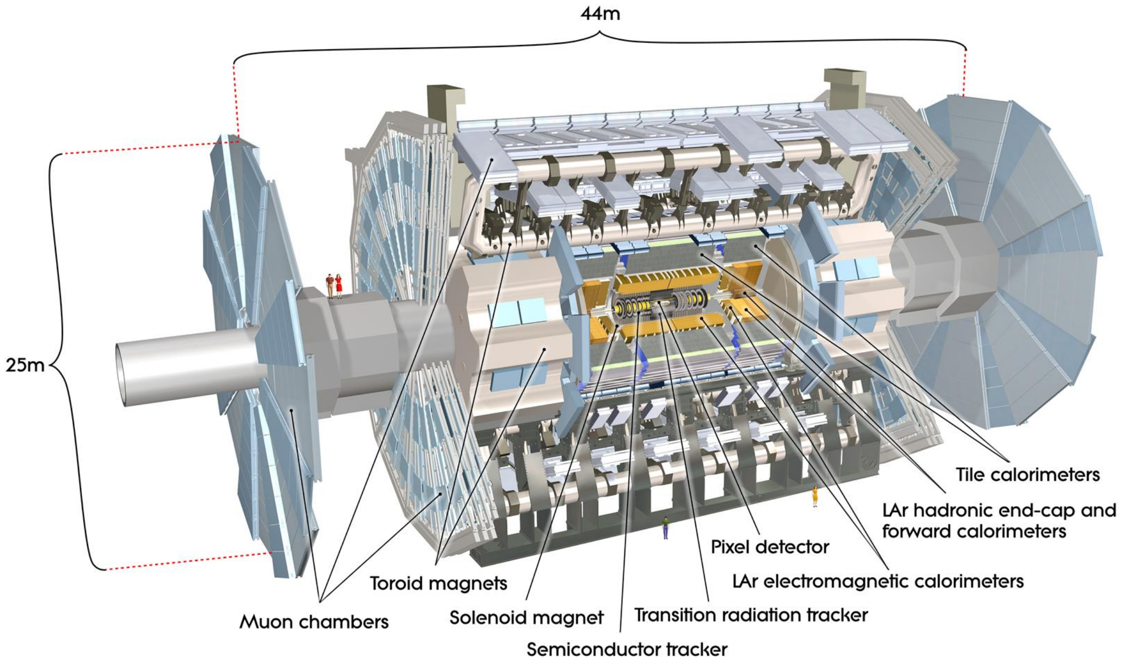

Figure 3.3: The ATLAS detector and its subsystems.

- good muon identification and momentum reconstruction;
- full azimuthal coverage for maximum efficiency, and highest possible pseudorapidity acceptance;
- fast and efficient triggering that can cope with high event rates while rejecting as much background as possible.

3.4.1 The Inner Detector

The Inner Detector (ID) is the innermost detector subsystem in ATLAS. It is 6.2 m in length and 2.1 m in diameter, immersed in a 2 T magnetic field from the surrounding central solenoid. The ID itself is composed of four subdetectors (from nearest to furthest from the beam pipe): the insertable B-layer (IBL), the Pixel detector, the silicon microstrip tracker (SCT) and the transition radiation tracker (TRT). A schematic overview of the ID is shown in Figure 3.4.

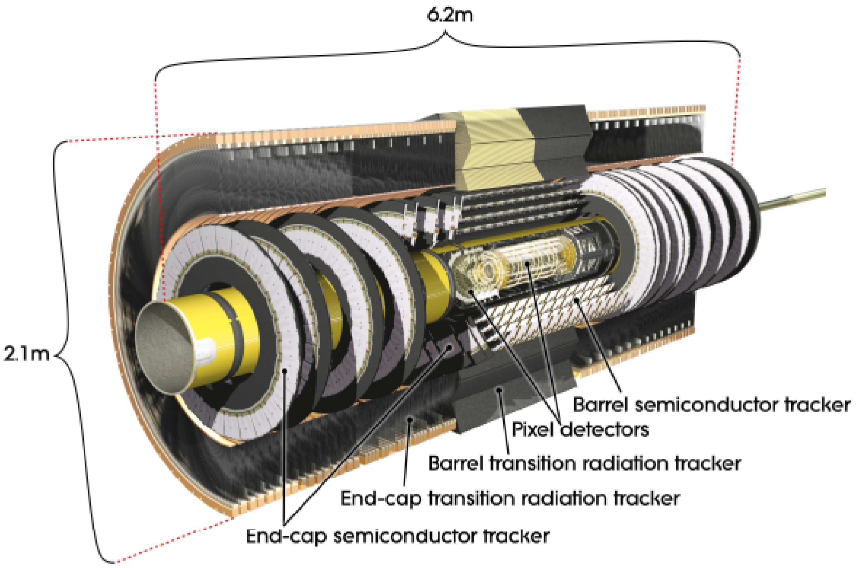

Figure 3.4: Overview of the ATLAS Inner Detector.

The IBL was installed during the planned Long Shutdown 1 (LS1) that occurred between Run-1 and Run-2, in 2013-14. This extra detector layer is necessary because the Pixel detector was originally designed for a peak luminosity of $\mathcal{L} = 1 \times 10^{34}\text{cm}^{-2}\text{s}^{-1}$, while the expected peak luminosity after Run-1 will be closer to $\mathcal{L} = 2 - 3 \times 10^{34}\text{cm}^{-2}\text{s}^{-1}$. Without the IBL, the inevitable degradation of the Pixel detector would cause ATLAS to no longer be able to meet the tracking and vertexing benchmarks needed for its physics program. The IBL consists of 14 staves arranged around the beam axis. The staves are flat and arranged at a 14° tilt with respect to the beam pipe circumference, as seen in Figure 3.5. Each stave consists of 20 sensor modules distributed over 64 cm of length and spanning an η range of 2.9. The pixel size in the IBL chipsets is $50 \times 250\ \mu\text{m}^2$.

Immediately after the IBL is the Pixel detector, which is composed of 3 concentric cyllindrical barrels with 3 disks at each end-cap. The number of layers and their arrangement predicts that each track should have 3 pixel hits. The Pixel has a resolution of 10 μm in $R - \phi$, 115 μm in z for the barrel region, and 115 μm in R for the end-caps.

Surrounding the Pixel is the SCT, composed of 4 coaxial cyllindrical layers in the barrel and 9 disks at each end-cap. Each cyllindrical layer has 2 strip layers, one parallel to the beam axis and another that is offset by 40 mrad. This geometrical arrangement allows for a 2-dimensional coordinate measurement at each cyllinder. A similar setup is found in the end-cap where one strip is radially aligned while the other is offset again by 40 mrad. The SCT is accurate to 17 μm in the xy plane, 580 μm along the z-axis and 580 μm in R at the end-caps.

The TRT is the outermost subdetector in the ID. Its 4 mm diameter straw tubes are 144 cm long and arranged parallel to the beam axis over 73 layers in the barrel, and 37 cm long over 160 straw planes in the end-caps. The TRT straws have an accuracy of 130 μm per straw, but can only make measurements in the xy plane. Though the resolution is lower than the SCT and Pixel, the TRT is able to make more measurements per track over a longer length which significantly improves the track momentum measurement.

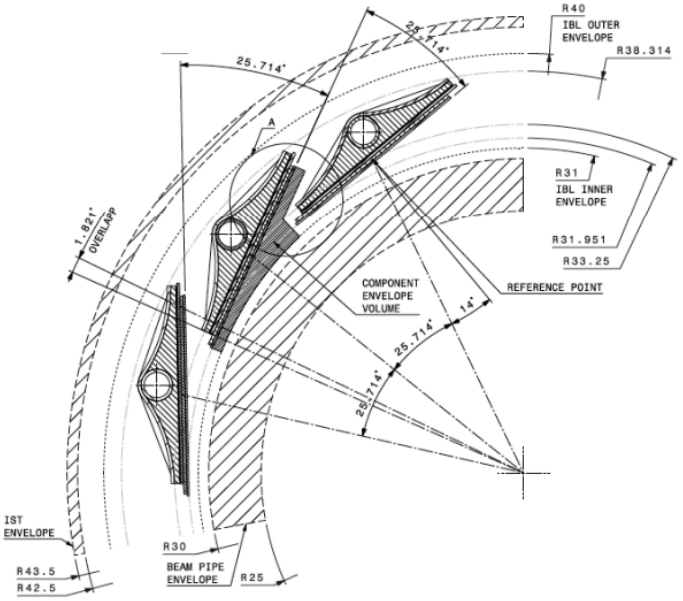

Figure 1. IBL structure in $r - \phi$ plane.

Figure 3.5: IBL structure in the xy plane.

3.4.2 The Calorimeter

The ATLAS calorimeter system covers the range $|\eta| < 4.9$, and consists of an electromagnetic calorimeter (EM) just outside the ID and a hadronic calorimeter (HCal) that envelops the EM calorimeter. The EM calorimeter has fine granularity and is particularly well suited for electron and photon reconstruction, while the hadronic calorimeter has coarser granularity that nevertheless is sufficient for reconstructing jet showers. The ATLAS calorimeter system has approximately 10 interaction lengths (λ), which provides excellent containment for both electromagnetic and hadronic showers. This will ensure a good missing energy measurement and reduce background in the muon spectrometer to negligible levels.

The EM calorimeter is a lead-liquid Argon detector with barrel ($|\eta| < 1.475$) and end-cap ($1.375 < |\eta| < 3.2$) components. It has an accordion shape in order to provide complete ϕ coverage without azimuthal discontinuities, and lead absorber plates that are 1.53 mm

(1.7-2.2 mm) thick in the barrel (end-cap). The calorimeter can have two or three layers depending on the η region, as well as a presampler layer for $|\eta| < 1.8$ (see Table 3.1). The presampler is a 1.1 cm thick active LAr layer used to recover the energy lost by electrons and photons prior to reaching the calorimeter (0.5 cm thick in the end-caps). The EM calorimeter has a total thickness of over 22 radiation lengths (X_0) in the barrel and at least 24 radiation lengths in the end-caps, with an energy resolution $\frac{\sigma_E}{E} = 10.1\%/\sqrt{E} \oplus 0.17\%$ (see Figure 3.6).

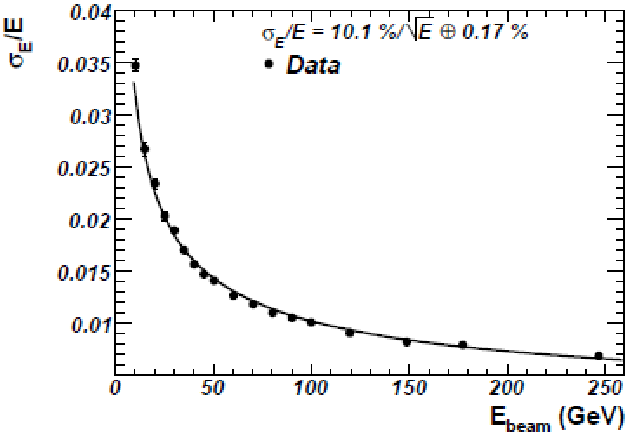

Figure 3.6: Fractional energy resolution of a barrel LAr calorimeter module as a function of the electron beam energy.

Similar to the other ATLAS subsystems, the HCal has separate structures for the barrel and end-caps. The barrel hadronic calorimeter is often called the Tile calorimeter, with a central barrel for the range $|\eta| < 1.0$ and two extended barrels in the region $0.8 < |\eta| < 1.7$. It uses scintillating plastic tiles for sampling material and steel as the absorber. Radially, the tile calorimeter goes from 2.28 m to 4.25 m, and is azimuthally divided in 64 modules. The barrel is segmented in three layers with interaction lengths of approximately 1.5, 4.1 and 1.8 for a total thickness of 9.7 λ at $\eta = 0$.

In the end-caps we have the Hadronic End-cap Calorimeter (HEC). Located directly behind the EM calorimeter, the HEC uses the same LAr cryostats as the EM calorimeter for the sampling medium. It consists of two independent coaxial wheels per end-cap, each one

Table 3.1: Parameters of the ATLAS calorimeter.

	Barrel		End-cap	
	Granularity versus $\lvert\eta\rvert$			
Presampler	0.025×0.1	$\lvert\eta\rvert < 1.52$	0.025×0.1	$1.5 < \lvert\eta\rvert < 1.8$
Calorimeter 1st layer	$0.025/8 \times 0.025$	$\lvert\eta\rvert < 1.4$	0.050×0.1	$1.375 < \lvert\eta\rvert < 1.425$
	0.025×0.025	$1.40 < \lvert\eta\rvert < 1.475$	0.025×0.1	$1.425 < \lvert\eta\rvert < 1.5$
			$0.025/8 \times 0.1$	$1.5 < \lvert\eta\rvert < 1.8$
			$0.025/6 \times 0.1$	$1.8 < \lvert\eta\rvert < 2.0$
			$0.025/4 \times 0.1$	$2.0 < \lvert\eta\rvert < 2.4$
			0.025×0.1	$2.4 < \lvert\eta\rvert < 2.5$
			0.1×0.1	$2.5 < \lvert\eta\rvert < 3.2$
Calorimeter 2nd layer	0.025×0.025	$\lvert\eta\rvert < 1.4$	0.050×0.025	$1.375 < \lvert\eta\rvert < 1.425$
	0.025×0.025	$1.40 < \lvert\eta\rvert < 1.475$	0.025×0.025	$1.425 < \lvert\eta\rvert < 2.5$
			0.1×0.1	$2.5 < \lvert\eta\rvert < 3.2$
Calorimeter 3rd layer	0.050×0.025	$\lvert\eta\rvert < 1.35$	0.050×0.025	$1.5 < \lvert\eta\rvert < 2.5$

built from 32 wedge-like copper plate modules, and spans the $1.5 < |\eta| < 3.2$ region. The average energy resolution of the HCal is $\frac{\sigma_E}{E} = 50\%/\sqrt{E}$. Finally, also in the end-cap region and convering the range $3.1 < |\eta| < 4.9$ we have the Forward Calorimeter (FCal), consisting of three modules and 10 interaction lengths of thickness. The first module has copper for the absorption material making it well suited for electromagnetic measurements, while the outer two modules are made of tungsten and serve the role of a hadronic calorimeter. The sensitive medium is again liquid Argon and the energy resolution is $\frac{\sigma_E}{E} = 100\%/\sqrt{E}$.

3.4.3 The Muon Detector

The general layout of the ATLAS Muon Spectrometer (MS) is shown in Figure 3.7. The MS relies on detecting muon tracks passing through its tracking chambers as they are deflected by a strong magnetic field. The field is generated by large air-core superconducting toroid magnets located in the barrel ($|\eta| < 1.4$) and end-caps ($1.6 < |\eta| < 2.7$). The barrel MS is distributed over three cyllindrical layers parallel to the beam axis, while the end-caps also have three disk-shaped layers parallel to the xy plane. The precision tracking in the MS is done by Monitored Drift Tubes (MDTs) in the barrel, and Cathode Strip Chambers (CSCs) in the end-caps. The MS also has its own triggering system covering the range $|\eta| < 2.4$, which is provided by Resistive Plate Chambers (RPCs) in the barrel and Thin Gap Chambers (TGCs) in the end-caps.

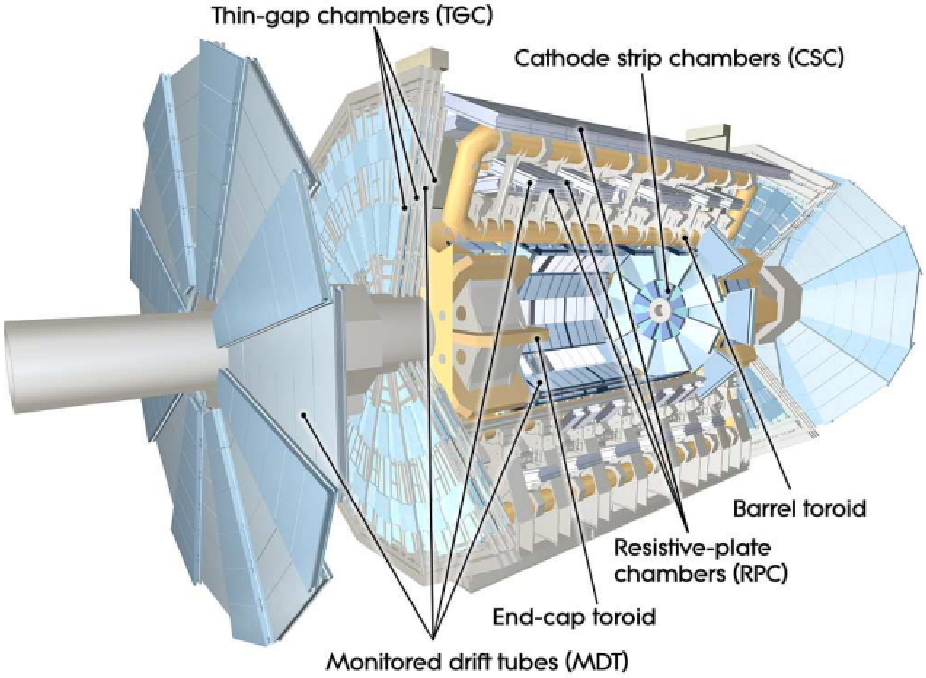

Figure 3.7: Structural layout of the ATLAS muon spectrometer.

The MDTs are 30 mm pressurized drift tubes filled with an Ar/CO_2 gas mixture at a 97/3 ratio and 3 bar. Electrons resulting from gas ionization due to passing muons are collected in a tungsten-rhenium wire at the center of the tube (Figure 3.8). The MDTs are assembled inside MDT chambers that are rectangular in the barrel and trapezoidal in the end-cap, each containing 6-8 tubes. The resolution of a single MDT is approximately 80 μm, while a complete MDT chamber has a resolution of 35 μm.

It is important to note that the MDT measures the particle's coordinate only in the bending plane. For a full track measurement in the barrel, the RPC's measurement in the non-bending plane must be added. The RPC consists of three cyllindrical layers, the two innermost chambers select low momentum tracks in the range 6-9 GeV, while the outermost layer above the MDT selects high momentum particles. Each layer contains two independent gaseous parallel electrode-plate detectors, thus giving 6 different measurements for a track that hits all three layers. A coincidence scheme is then used (3-of-4 hits for RPCs 1 and 2, and 1-of-2 for RPC3) that has high efficiency with strong rejection power of spurious track signals.

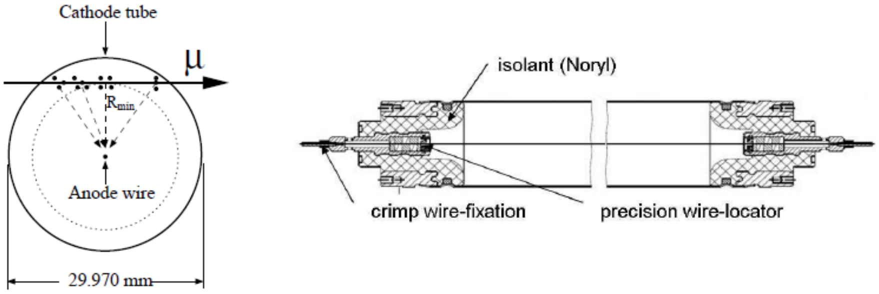

Figure 3.8: Cross-sectional and longitudinal view of a monitored drift tube.

The CSCs are multiwire proportional chambers with orthogonally aligned cathode segments. Each end-cap contains two CSC disk systems, each made of eight large and eight small CSC chambers. The CSC chambers have radially-oriented anode wires and cathode strips that can be either parallel or perpendicular to the wires (see Figure 3.9). This orthogonal orientation allows for both η and ϕ measurements at each of the four CSC planes in a chamber. The final CSC resolution is 40 μm in the bending plane and 5 mm in the transverse plane.

The TGCs provide muon trigger capability in the end-caps as well as a measurement of the ϕ coordinate to suplement the MDT radial measurement. There are seven TGC layers accompanying the middle end-cap MDT measurement, and two TGC layers accompanying the inner MDT layer measurement. The azimuthal coordinate of hits in the outer MDT layer are obtained through extrapolation from the middle TGC layer, made possible by the

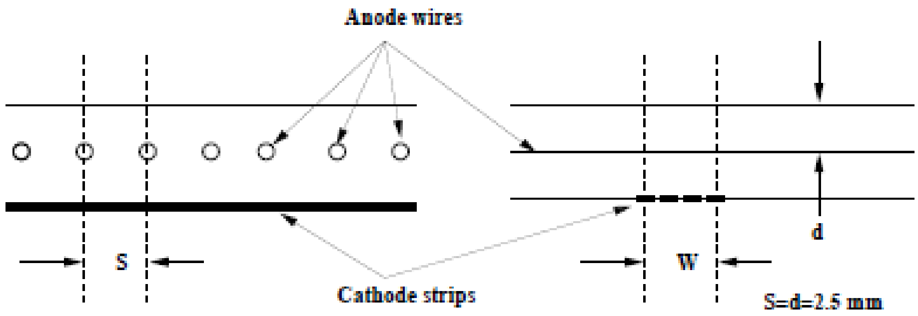

Figure 3.9: Cross-sectional view of a CSC cell.

lack of magnetic field between the two outer MDT planes. The TGC's principal of operation is through a multiwire proportional chamber with two cathode planes and an anode wire plane kept at 2900 V. The chamber resolution is 2-6 mm in R, 3-7mm in ϕ and 4 ns in time. A schematic overview of the TGC/MDT layout and the greater ATLAS MS system in the end-cap region is shown in Figure 3.10.

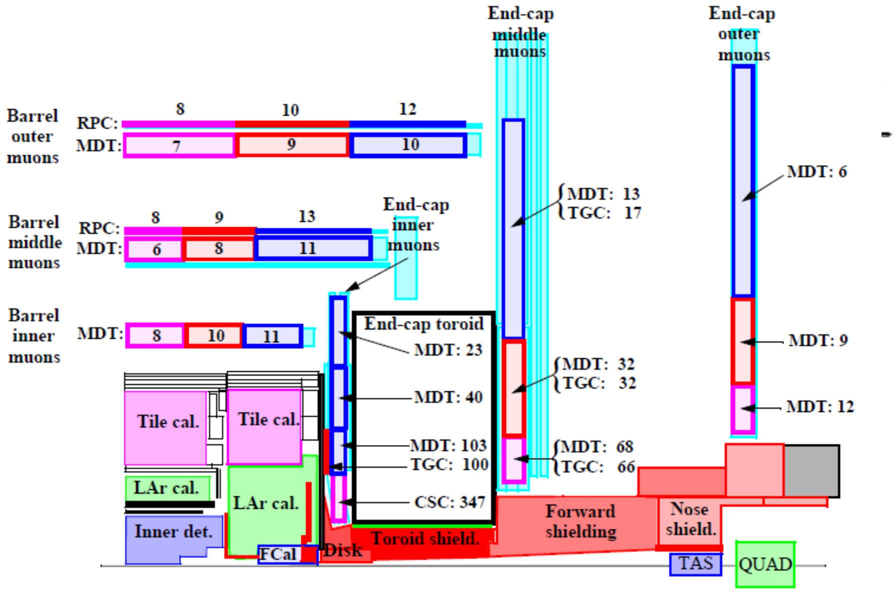

Figure 3.10: Cross-sectional view of the ATLAS muon spectrometer end-cap.

3.4.4 The ATLAS Trigger System

The LHC beam bunches contain upwards of 10^{11} protons colliding 40 million times per second. A typical ATLAS event occupies a few MB of disk space, so it is not feasible to store every event reconstructed by the ATLAS detector. In addition, many events correspond to well-known processes that are not of interest to the ATLAS physics program. In order to select only events that are potentially interesting and to cope with hardware memory limitations, ATLAS employs a multi-leveled trigger system.

In Run-1, the ATLAS trigger sequence was composed of the L1, L2 and Event Filter (EF) triggers. The L1 trigger is the first and lowest trigger level. It searches for events with muons, electrons, τ-leptons, photons and jets with high transverse momentum. Missing energy triggers are also employed. The L1 triggers function by defining Regions-of-Interest (RoIs) where signatures compatible with these objects have been detected, e.g. radial and $\eta - \phi$ coordinates of a high energy cluster in the EM calorimeter. After the event has been flagged as potentially interesting by at least one L1 trigger, the L2 triggers are called. Seeded by the L1 RoI, they use every possible online detector measurement near the RoI to further refine the event selection. The output rate of the L2 trigger is approximately 3.5 kHz, and it takes roughly 40 ms to give a binary decision on whether to keep the event. Finally, if the event passes both L1 and L2 triggers, it goes to the EF. This last step is done offline as it has a processing time on the order of 4 seconds, and brings the output rate down to 200 Hz.

For Run-2, the ATLAS trigger system has undergone several upgrades [36]. Hardware upgrades, new coincident schemes and improvements to the detector readout have allowed the L1 output rate to be raised from 70 kHz in Run-1 to 100 kHz in Run-2. Another significant change is that the L2 trigger layer is now merged with the EF into a unified higher-level trigger system (HLT). Trigger selections have been aligned with offline analysis requirements in order to reduce trigger inefficiency. The new HLT also allows some triggers to group multiple RoIs into one object ('super-RoI'), reducing the processing requirements for events where these objects are present. These improvements have allowed the average final output rate of the HLT system to be increased to 3 kHz.

Chapter 4

$A \to ZH \to \ell\ell\tau_{lep}\tau_{had}$

In this chapter we describe the ATLAS search for a heavy CP-odd Higgs boson, A, using Run-1 proton-proton collision data at a center-of-mass of 8 TeV and total integrated luminosity of 20.3 fb^{-1}. The search is done for the $A \to Zh$ decay mode and m_A range of $220 - 1000$ GeV. The final event signature being searched consists of a Z decaying to light leptons, and h decaying to $\tau\tau$, where one tau decays leptonically (τ_{lep}) and the other decays hadronically (τ_{had}). The $A \to Zh$ branching fraction is high for masses below the $t\bar{t}$ production threshold, so this search is particularly powerful in the $220 < m_A < 350$ GeV region (the lower bound corresponds to the mass threshold for on-shell decays).

4.1 Samples

4.1.1 Data Sample

This analysis uses proton-proton collision data recorded by the ATLAS detector during 2012 at a center-of-mass energy of 8 TeV. Only events collected with stable beams and all ATLAS sub-systems operational are recorded, resulting in 20.3 fb^{-1} with a 2.8% uncertainty in the luminosity measurement.

4.1.2 Monte Carlo Simulated Samples

In order to accurately predict the Standard Model background in our signal region, it is necessary to use simulated events for the various physics processes that can occur in the proton-proton collisions of the LHC. Monte Carlo (MC) simulated samples were generated for W+jets, Z+jets, $t\bar{t}$, single top, diboson and Z-associated SM Higgs production. The simulation is performed in two steps: the first is the Matrix Element that simulates the parton collision and production, and the second is the simulation of hadronic showering of the quarks and gluons that were produced.

Signal samples for the gluon-fusion production of an A boson decaying to a tau pair are produced for all three possible tau final states: $A \to Zh \to \ell\ell\tau_{lep}\tau_{lep}$, $\ell\ell\tau_{lep}\tau_{had}$, $\ell\ell\tau_{had}\tau_{had}$, where ℓ can be an electron, muon or tau. Several m_A hypotheses between 220 and 1000 GeV are considered. The event generation is done with MadGraph5 [37], and the subsequent parton hadronization is done with Pythia8 [38]. Theoretical cross sections and branching ratios for 2HDM type-I and II in the SM-like limit ($\sin(\beta - \alpha) \to 1$) are shown in Tables 4.1 and 4.2. This limit corresponds to the case where the lightest Higgs (h) couplings to fermions and vector bosons are similar to those for the SM Higgs boson. Signal cross sections are computed with `SusHi` [39], and branching ratios were obtained using `2HDMC` [40]. The $A \to Zh$ branching ratio drops sharply for $m_A > 350$ GeV due to the decay to $t\bar{t}$ becoming kinematically allowed and, therefore, dominant.

Table 4.1: Cross sections and branching ratios at different m_A hypotheses for type-I 2HDM.

m_A [GeV]	$\sin(\beta-\alpha)$	$\cos(\beta-\alpha)$	$\sigma(gg \to A)$[pb]	BR($A \to Zh$)	BR($h \to \tau\tau$)
			Type-I and $\tan(\beta) = 1$		
260	0.999	0.045	6.0135	0.11660	0.06079
340	0.999	0.045	4.4484	0.04540	0.06079
360	0.999	0.045	4.8650	0.00158	0.06079
500	0.999	0.045	1.7543	0.00260	0.06079
1000	0.999	0.045	0.0291	0.01235	0.06079
			Type-I and $\tan(\beta) = 10$		
260	0.999	0.045	3.0258	0.92957	0.05978
340	0.999	0.045	2.2424	0.82626	0.05978
360	0.999	0.045	2.4535	0.13629	0.05978
500	0.999	0.045	0.8855	0.20695	0.05978
1000	0.999	0.045	0.0147	0.55573	0.05978

Table 4.2: Cross sections and branching ratios at different m_A hypotheses for type-II 2HDM.

m_A [GeV]	$\sin(\beta-\alpha)$	$\cos(\beta-\alpha)$	$\sigma(gg \to A)$[pb]	BR($A \to Zh$)	BR($h \to \tau\tau$)
			Type-II and $\tan(\beta) = 1$		
260	0.999	0.045	6.0135	0.11915	0.05714
340	0.999	0.045	4.4484	0.04556	0.05713
360	0.999	0.045	4.8650	0.00158	0.05713
500	0.999	0.045	1.7543	0.00260	0.05713
1000	0.999	0.045	0.0291	0.01235	0.05713
			Type-II and $\tan(\beta) = 10$		
260	0.999	0.045	3.0258	0.00363	0.03358
340	0.999	0.045	2.2424	0.01728	0.03358
360	0.999	0.045	2.4535	0.01912	0.03358
500	0.999	0.045	0.8855	0.04951	0.03358
1000	0.999	0.045	0.0147	0.22088	0.03358

The event generation for Z+jets processes is done with SHERPA [41]. Top pair and single top production is simulated with POWHEG [42, 43] and AcerMC[44]. Diboson production (ZZ, WZ, WW) is simulated with POWHEG. Triboson (WWW, ZWW, ZZZ) and top-associated Z boson production is done with MadGraph5. We also consider the Z-associated SM Higgs boson production, which is simulated with Pythia8.

To simulate the detector response, the events pass through a full simulation of the ATLAS detector done with GEANT4 [45] before being reconstructed with the same ATLAS software used in data events. Due to the high number of bunches during stable beams at the LHC, multiple interactions within the same and nearby bunch crossings can occur. This effect is known as "pileup" and is taken into account by overlaying the simulated samples onto minimum-bias events, which are events obtained using a minimal trigger requirement that are a good representation of the background from soft QCD interactions. Finally, a reweighting of the MC samples according to the average number of interactions per bunch crossing is done to match the same distribution in data events.

4.2 Reconstruction

The signal events in this search have electrons, muons and taus in the final state, as well as missing transverse energy due to neutrinos from the tau decays. Reconstruction software translates these low-level detector signals, e.g. tracks and calorimeter deposits, into physical objects.

4.2.1 Electrons

The fundamental requirement for an electron candidate is to have energy deposits in the EM calorimeter with geometrically compatible charged-particle tracks in the Inner Detector [46, 47]. Sequential cuts are applied on variables derived from calorimeter clusters, tracking and combined cluster-tracking information in order to define three levels of electron identification. These identification levels are labeled "loose", "medium" and "tight", and have progressively higher background rejection power at a cost to identification efficiency. Only candidates in pseudorapidity range of $|\eta| < 2.47$ and outside the calorimeter crack region ($1.37 < |\eta| < 1.52$) are allowed, where the crack pseudorapidity region corresponds to the transition region between the barrel and end-cap calorimeters. All electrons are required to have transverse momentum greater than 7 GeV and pass the medium-level identification criteria. To reject electrons originating from hadronic decays, candidates must also be reconstructed with little activity in the surrounding calorimeter area, i.e. the candidate must be isolated. A lepton is considered isolated if the sum of calorimeter energy deposits in a cone around the candidate track (and not counting the energy measured from the track itself) is a small fraction of the lepton transverse momentum. The isolation criteria for electrons and muons used in this analysis are a combination of both track and calorimeter isolation, specifically given by:

- ptcone40$/p_T < 0.2$ and etcone20$/p_T < 0.2$ if there are no other leptons within a cone of $\Delta R = 0.4$;

- ptcone20/$p_T < 0.2$ and etcone20/$p_T < 0.2$ if there is at least one other lepton within a cone of $\Delta R = 0.4$.

The term ptcone20 (ptcone40) correspond to the sum of transverse momenta of all tracks measured in a cone of $\Delta R = 0.2$ (0.4) around the electron track. Analogously, etcone20 is the sum of the measured transverse energy in the calorimeter clusters located in the $\Delta R = 0.2$ cone surrounding the electron track. The smaller p_T cone used in the case of overlapping leptons is intended to avoid the neighboring lepton to cause a failure of the isolation requirement. This is important for higher m_A signal hypotheses where the Z boson is boosted, i.e. has high transverse momentum, causing the leptons from the $Z \to \ell\ell$ decay to become collimated.

4.2.2 Muons

Muon candidates are identified by the coincident detection of tracks in the Inner Detector and the Muon Spectrometer [48]. Muon candidates are considered for pseudorapidities as high as 2.7 by making use of the tracking provided by the forward muon spectrometer, and are required to have $p_T > 6$ GeV and pass the same isolation requirement as that for electrons.

4.2.3 Jets

The term jet refers to the group of collimated particles that are generated from the hadronization of energetic gluons and quarks. Jet reconstruction is done through the combination of calorimeter cell deposits in a process known as clustering. The ATLAS jet reconstruction is done by first identifying all calorimeter cells with energy deposits at least four times the background noise. After the initial jet seeds are identified, nearby calorimeter cells with energy deposits at least twice the noise level are added, along with any cells neighboring them that have a positive energy measurement. This combination leads to the formation of a 3-dimensional shower object spread over several calorimeter layers, and is called a topological cluster, or topo-cluster [49].

After the topo-clusters have been determined, the anti-kt algorithm is used to combine them into jets [50]. This is a sequential clustering algorithm that uses the distance d_{ti} between high-energy (hard) and low-energy (soft) clusters to decide how to do their combination. This distance is given by

$$d_{ti} = \min(1/k^2_{hard,i}, 1/k^2_{soft,j})\frac{\Delta^2_{ij}}{R^2}, \tag{4.1}$$

where k_{hard} (k_{soft}) is the transverse momentum of the hard (soft) cluster, Δ_{ij} is the angular distance between the clusters, and R is the cone size parameter used during clustering, in this case 0.4. This analysis has no explicit jet selection, but they have an indirect role in our selection by contributing to the missing transverse energy calculation. Taus can also decay hadronically with a similar, but narrower, shower cone. Unless explicitly stated otherwise, this text will use the term jet to refer only to the hadronization showers from quarks and gluons.

4.2.4 Taus

Hadronically decaying tau candidates are initially seeded from low-level jet objects. Only jets with $p_T > 10$ GeV are considered for hadronic tau reconstruction [51]. All τ_{had} candidates must have $p_T > 20$ GeV and $|\eta| < 2.47$ (2.5) for 1-track (3-track) τ_{had}. Jets from QCD processes are often misidentified as hadronic taus, so a multivariate classifier is used to reduce the jet$\rightarrow \tau_{had}$ fake rate. This algorithm is referred to as the τ_{had}-ID, or TauID, and plays a crucial role in the identification and use of hadronic taus in ATLAS. A detailed description of the TauID algorithm, as well as its three identification levels "loose", "medium" and "tight", can be found in Appendix A. A separate BDT-based algorithm is used to reject $e \rightarrow \tau_{had}$ fakes, called the eVeto. Because of the high efficiency of muon reconstruction, the fake rate of $\mu \rightarrow \tau_{had}$ can be brought to very small levels by applying a geometric overlap removal between taus and muons, as described below. However, occasionally muons may fail reconstruction rendering overlap removal impossible. This can happen, for example, if they are low energy and stop in the calorimeter before reaching the muon spectrometer. These events have different distributions for the energy deposited in the EM calorimeter and for the ratio of track momentum to measured calorimeter energy, and are rejected with a simple cut-based selection on these variables.

4.2.5 Missing Transverse Energy

Neutrinos are weakly interacting particles that propagate through the ATLAS detector without interacting with its components. Because the total momentum in the xy plane before the collision is zero, it is possible to calculate the amount and direction of the missing energy in the transverse plane through momentum conservation. This is called the Missing Transverse Energy, or E_T^{miss}. The longitudinal missing energy cannot be calculated because the momentum fraction of each colliding parton is unknown. The E_T^{miss} is defined as the opposite of the $\vec{p}_T$ sum of all reconstructed objects in an event [52], and therefore is often the last step in the event reconstruction. For the remainder of this thesis, the term "visible" and the superscript *vis* will denote quantities that are reconstructed without extrapolating the missing energy contribution due to neutrinos.

4.2.6 Object Overlap Removal

Often a particle will pass the reconstruction criteria of multiple object types, e.g. an object reconstructed as both e and τ. Thus, an "object overlap removal" procedure must be defined to unambiguously reconstruct an event. Object overlap is a geometric consideration based on whether the angular distance ΔR between the objects is smaller than a certain threshold. The following priority is used when removing objects:

- Jets within a $\Delta R = 0.2$ cone of any hadronic tau or light lepton are excluded;

- Hadronic taus within a $\Delta R = 0.2$ cone of electrons or muons are excluded, except when the τ is of at least "loose" identification quality and the overlapping lepton is not. For the latter case, the light lepton is removed;

- Electrons within a $\Delta R = 0.2$ cone of muons are excluded, except when the e is of at least "loose" quality and the μ is not. For the latter case, the μ is excluded.

4.2.7 Mass Reconstruction

The final discriminant used in this analysis is the reconstructed A boson mass m_A^{rec}. To obtain m_A^{rec}, one must first reconstruct the mass of the $\tau_{lep}\tau_{had}$ pair. This can be challenging because tau decays contain neutrinos and, therefore, large E_T^{miss}. To account for this, a dedicated mass reconstruction algorithm is used, called the Missing Mass Calculator (`MMC`) [53]. To reconstruct the ditau mass, the `MMC` must solve the following set of equations:

$$\begin{aligned}
E_{T,x}^{miss} &= p_1^{miss}\sin\theta_1^{miss}\cos\phi_1^{miss} + p_2^{miss}\sin\theta_2^{miss}\cos\phi_2^{miss},\\
E_{T,y}^{miss} &= p_1^{miss}\sin\theta_1^{miss}\sin\phi_1^{miss} + p_2^{miss}\sin\theta_2^{miss}\sin\phi_2^{miss},\\
M_{\tau_1}^2 &= (m_1^{miss})^2 + (m_1^{vis})^2 + 2\sqrt{(p_1^{vis})^2 + (m_1^{vis})^2}\sqrt{(p_1^{miss})^2 + (m_1^{miss})^2} - 2p_1^{vis}p_1^{miss}\cos\Delta\theta_{\nu m_1},\\
M_{\tau_2}^2 &= (m_2^{miss})^2 + (m_2^{vis})^2 + 2\sqrt{(p_2^{vis})^2 + (m_2^{vis})^2}\sqrt{(p_2^{miss})^2 + (m_2^{miss})^2} - 2p_2^{vis}p_2^{miss}\cos\Delta\theta_{\nu m_2},
\end{aligned} \tag{4.2}$$

where $E_{T,x}^{miss}$ and $E_{T,y}^{miss}$ are the components of E_T^{miss} in the transverse plane, and $p_{1,2}^{vis}$, $m_{1,2}^{vis}$, $\theta_{1,2}^{vis}$, $\phi_{1,2}^{vis}$ are the (unknown) momenta, invariant masses, polar and azimuthal angles of the visible tau decay products. Variables $p_{1,2}^{miss}$, $m_{1,2}^{miss}$, $\theta_{1,2}^{miss}$, $\phi_{1,2}^{miss}$ are the analogous terms for the invisible products. The tau lepton invariant mass is $M_{\tau_{1,2}} = 1.777$ GeV/c^2, and $\Delta\theta_{\nu m_{1,2}} = |\theta_{1,2}^{vis} - \theta_{1,2}^{miss}|$ corresponds to the azimuthal angle difference between the visible and invisible momentum vectors.

Since hadronic (leptonic) tau decays have one (two) neutrino(s), a $\tau_{lep}\tau_{had}$ decay has seven unknown variables (using the constraint that $m_{\tau_{had}}^{miss}$ is zero). Since there are only four equations in 4.2, the system is underconstrained. However, not all regions of the unconstrained parameter space are equally likely. This is clear if one looks at ΔR distributions between visible and invisible momenta in simulated hadronic and leptonic tau decays. As Figure 4.1 shows, depending on the tau decay type (1-track, 3-track or leptonic), certain decay topologies are favored and a probability density function can be constructed.

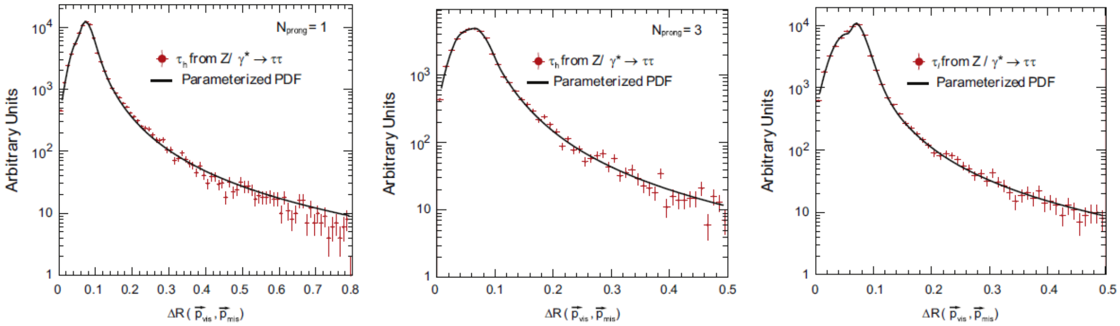

Figure 4.1: Example distributions of the angular distance between visible and invisible momenta of tau decay products for the cases of 1-track (left), 3-track (middle) and leptonic (right) tau decay types. Plots from Reference [53].

The `MMC` then solves Equations 4.2 by scanning through the kinematically allowed region of the system variables and weighs each solution by its corresponding global decay topology probability, given by:

$$\mathcal{P}_{\text{event}} = \mathcal{P}(\Delta R_1, p_{\tau 1}) \times \mathcal{P}(\Delta R_2, p_{\tau 2}), \tag{4.3}$$

where the probabilty functions $\mathcal{P}$ depend on the tau decay type and the initial momentum of the parent tau lepton. This scanning procedure will give a distribution of possible values for $m_{\tau\tau}$, and the returned value for the $m_{\tau\tau}^{MMC}$ estimate is the maximum of this probability-weighed distribution. For events with leptonic tau decays, the weighting procedure is adjusted by incorporating an additional probabilty, also obtained from simulation, for the invariant mass of the τ_{lep} neutrinos.

Because we know the dilepton and ditau pairs in the event must come from a Z and an h boson, respectively, we can achieve a better resolution by subtracting from the 4-object invariant mass the difference of the reconstructed $\ell\ell$ and $\tau\tau$ pair masses from their known parent particle values:

$$m_A^{rec} = m_{\ell\ell\tau\tau} - (m_{\ell\ell} - m_Z^0) - (m_{\tau\tau}^{MMC} - m_h^0). \tag{4.4}$$

The terms in Equation 4.4 are:

- m_Z^0 is the known mass of the Z boson, 91.2 GeV, and $m_H^0 = 125$ GeV is the mass of the assumed light Higgs;

- $m_{\tau\tau}^{MMC}$ is the mass of the tau pair as returned by the `MMC`;

- $m_{\ell\ell}$ is the invariant mass of the two light leptons that come from the Z decay;

- $m_{\ell\ell\tau\tau}$ is the invariant mass of the leptons from the Z and the two taus, where the latter is computed with the `MMC`.

4.3 Event Selection

Events in this search are initially selected by the firing of at least one of the following single-lepton triggers: `EF_e24vhi_medium1`, `EF_mu24i_tight` or `EF_mu36_tight`. In the case of the event being triggered only by the high p_T muon trigger, we require the offline transverse momentum of the highest p_T muon to be greater than 36 GeV. Dilepton triggers were not included because they did not increase the acceptance significantly.

All events must have exactly three light leptons and one hadronic tau. Additional requirements for these objects are:

- the hadronic tau must have $p_T > 20$ GeV and pass medium-level TauID;

- the leading (remaining) electron(s) must have $p_T > 26$ GeV (15 GeV) and pass medium-level identification criteria;

- the leading (remaining) muon(s) must have $p_T > 25 - 36$ GeV (10 GeV), depending on the trigger, and pass medium-level identification criteria.

Since this search has three light leptons in the final state, it is important to distinguish which come from the $Z \to \ell\ell$ decay and which is from the leptonic tau decay. If the light lepton belongs to a pair with opposite sign and same lepton flavor, it is classified as the former. If more than one such pair is possible, the pair with invariant mass closest to the Z

boson mass (91.2 GeV) is assumed to come from the Z decay. If the invariant mass $m_{\ell\ell}$ of this lepton pair is outside a Z-mass window of $80 - 100$ GeV, the event is discarded. The following cuts are then applied to complete the $A \to Zh \to \ell\ell\tau_{lep}\tau_{had}$ selection:

- electrons, muons and the hadronic tau must pass their respective medium-level identification criteria;
- the `MMC` algorithm must succeed in reconstructing the mass of the $\tau_{lep}\tau_{had}$ pair, which in turn must be in the range $75 < m_{\tau\tau} < 175$ GeV.

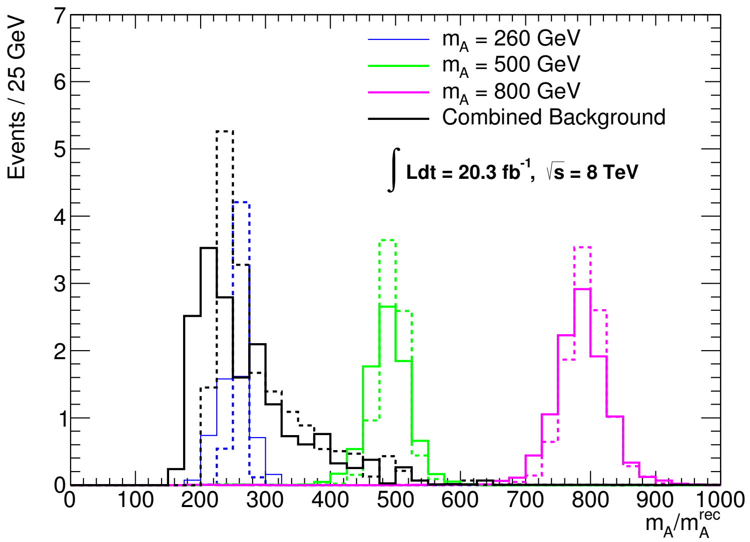

Figure 4.2: A comparison of $m_{\ell\ell\tau\tau}$ (solid) and m_A^{rec} (dashed) masses for $m_A = 260$ GeV, 500 GeV, 800 GeV, and the combined background. The background prediction shown here is exclusively from simulated events. The natural decay width of the A boson is typically small ($\Gamma_A/m_A \lesssim 1\%$), so that the width of the signal distributions is mostly due to the `MMC` reconstruction resolution.

Figure 4.2 shows distributions for several signal mass hyptheses of $m_{\ell\ell\tau\tau}$ and m_A^{rec}, where the latter can be seen to have significantly better resolution. Figure 4.3 shows the acceptance efficiency of the full selection on different signal mass hypotheses.

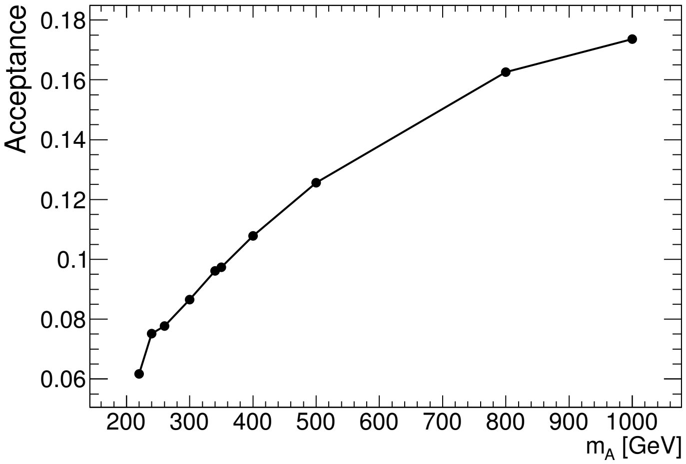

Figure 4.3: The signal acceptance efficiency for the full $\ell\ell\tau_{lep}\tau_{had}$ selection.

4.4 Background Estimation

The most important backgound processes that can pass our signal region selection are Z+jets, diboson and a smaller contribution from Z-associated SM Higgs production. In virtually all simulated events passing our selection, the light leptons are found to be matched to a true lepton. Background events can then be assigned to two different categories:

- events with correctly identified τ_{had}, or light leptons misidentifed as τ_{had};
- events with QCD jets misidentified as τ_{had}.

The background prediction of events in the first category is done entirely through simulated events, after confirming the reconstructed τ_{had} geometrically overlaps with a truth-level lepton, i.e. that the τ_{had} is truth-matched. However, because the jet $\rightarrow$ τ_{had} fake rate is not well modelled in simulation, events in the second category are predicted using a data-driven template method. To avoid bias, the selection and background estimation methods are developed while the analysis is blind, i.e. prior to looking at data events in our signal region.

The template method consists of obtaining the shape of the background distribution of the mass discriminant m_A^{rec}, i.e. the "background template", from a control region henceforth referred to as the template region. The template region has the same selection as the signal region, except that either the Higgs lepton and the τ_{had} have same-charge sign (SS), or the τ_{had} fails medium identifaction, or both. The normalization of the background template in the signal region is done using a scale factor measured in the Higgs mass sidebands (h-sidebands), where $m_{\tau\tau} < 75$ GeV or $m_{\tau\tau} > 175$ GeV. The scale factor is defined as the ratio of opposite-sign (OS) events passing medium TauID in the h-sideband region to the yield of template region events also in the h-sidebands. Since the objective is to estimate the fake-τ_{had} background, simulated events where the τ_{had} is truth-matched are subtracted from data at all levels in this procedure.

Effectively, the template region is defined by the separate or simultaneous failure to meet two selection criteria of the signal region: the τ_{had} medium identification, and the OS charge requirement of the $\tau_{lep}\tau_{had}$ system. Thus, the template region can be split into three regions (B, C and D) that have same selection as the signal region (A), except:

- region B has $\tau_{lep}\tau_{had}$ being same-sign charge;
- region C has the τ_{had} fail medium ID;
- region D has $\tau_{lep}\tau_{had}$ being same-sign charge and τ_{had} fails medium ID.

Table 4.3 shows event yields accross the 4 regions, while Table 4.4 shows the corresponding numbers in the h-mass sidebands.

4.4.1 Template Method Systematics

There are two potential sources of systematic error in the template method: if the background shape in the template region models poorly the corresponding shape in the signal region, and similarly if the normalization factor calculated in the h-sidebands is not an accurate measure of the same normalizing scale in the h-mass window. To investigate shape-related

Template control region event yields						
Sample	Region B		Region C		Region D	
	truth-matched $ll\tau\tau$	other	truth-matched $ll\tau\tau$	other	truth-matched $ll\tau\tau$	other
AZh (260 GeV)	0.0029 ± 0.0008	0.0030 ± 0.0008	0.1130 ± 0.0051	0.0265 ± 0.0023	0.0025 ± 0.0007	0.0247 ± 0.0021
AZh (400 GeV)	0.0038 ± 0.0009	0.0050 ± 0.0010	0.1344 ± 0.0057	0.0303 ± 0.0023	0.0042 ± 0.0010	0.0229 ± 0.0020
SM Higgs Zh	0.00 ± 0.00	0.01 ± 0.00	0.21 ± 0.01	0.02 ± 0.01	0.01 ± 0.00	0.02 ± 0.00
WW	0.00 ± 0.00	0.00 ± 0.00	0.00 ± 0.00	0.00 ± 0.00	0.00 ± 0.00	0.00 ± 0.00
WZ	0.00 ± 0.00	0.75 ± 0.19	0.00 ± 0.00	23.88 ± 1.07	0.00 ± 0.00	16.92 ± 0.89
ZZ	0.03 ± 0.01	0.23 ± 0.02	2.90 ± 0.11	3.09 ± 0.09	0.10 ± 0.02	2.97 ± 0.08
Triboson	0.00 ± 0.00	0.00 ± 0.00	0.01 ± 0.00	0.03 ± 0.01	0.00 ± 0.00	0.02 ± 0.00
Top	0.00 ± 0.00	0.42 ± 0.42	0.00 ± 0.00	0.81 ± 0.64	0.00 ± 0.00	0.88 ± 0.51
Top+Z	0.01 ± 0.01	0.03 ± 0.02	0.02 ± 0.01	0.48 ± 0.07	0.00 ± 0.00	0.27 ± 0.05
Z+Jets	0.00 ± 0.00	1.96 ± 1.21	0.00 ± 0.00	27.39 ± 5.55	0.00 ± 0.00	26.86 ± 5.35
Drell-Yan	0.00 ± 0.00	0.00 ± 0.00	0.00 ± 0.00	0.60 ± 0.30	0.00 ± 0.00	0.15 ± 0.14
Data	9		78		74	

Sample	Total		Signal Region	
	truth-matched $ll\tau\tau$	other	truth-matched $ll\tau\tau$	other
AZh (260 GeV)	0.118 ± 0.005	0.054 ± 0.003	0.478 ± 0.011	0.009 ± 0.001
AZh (400 GeV)	0.142 ± 0.006	0.058 ± 0.003	0.662 ± 0.012	0.015 ± 0.002
SM Higgs Zh	0.22 ± 0.01	0.05 ± 0.00	0.85 ± 0.02	0.02 ± 0.00
WW	0.00 ± 0.00	0.00 ± 0.00	0.00 ± 0.00	0.00 ± 0.00
WZ	0.00 ± 0.00	41.55 ± 1.40	0.00 ± 0.00	2.15 ± 0.32
ZZ	3.04 ± 0.11	6.29 ± 0.12	6.97 ± 0.17	0.30 ± 0.03
Triboson	0.01 ± 0.00	0.05 ± 0.01	0.08 ± 0.01	0.00 ± 0.00
Top	0.00 ± 0.00	2.11 ± 0.92	0.00 ± 0.00	0.00 ± 0.00
Top+Z	0.02 ± 0.01	0.78 ± 0.09	0.02 ± 0.01	0.07 ± 0.02
Z+Jets	0.00 ± 0.00	56.21 ± 7.80	0.00 ± 0.00	1.10 ± 0.66
Drell-Yan	0.00 ± 0.00	0.75 ± 0.33	0.00 ± 0.00	0.00 ± 0.00
Data	161		18	

Table 4.3: Number of events passing the $\tau_{lep}\tau_{had}$ channel selection in the template control region. For a better overview, the events are also split in regions B ($\tau_{lep}\tau_{had}$ is SS, τ_{had} passes TauID), C ($\tau_{lep}\tau_{had}$ is OS, τ_{had} fails TauID) and D ($\tau_{lep}\tau_{had}$ is SS, τ_{had} fails TauID). The signal region is also shown for comparison. Signal numbers assume $\sigma(gg \to A) \times BR(A \to Zh \to ll\tau\tau) = 1$ fb.

Higgs sidebands control region event yields						
Sample	Region B		Region C		Region D	
	truth-matched $ll\tau\tau$	other	truth-matched $ll\tau\tau$	other	truth-matched $ll\tau\tau$	other
AZh (260 GeV)	0.00027 ± 0.00027	0.0006 ± 0.0002	0.0092 ± 0.0015	0.0174 ± 0.0017	0.0000 ± 0.0000	0.0164 ± 0.0017
AZh (400 GeV)	0.00039 ± 0.00027	0.0012 ± 0.0005	0.0079 ± 0.0014	0.0225 ± 0.0021	0.0005 ± 0.0003	0.0239 ± 0.0021
SM Higgs Zh	0.00 ± 0.00	0.00 ± 0.00	0.01 ± 0.00	0.01 ± 0.00	0.00 ± 0.00	0.02 ± 0.00
WW	0.00 ± 0.00	0.00 ± 0.00	0.00 ± 0.00	0.00 ± 0.00	0.00 ± 0.00	0.00 ± 0.00
WZ	0.00 ± 0.00	0.70 ± 0.18	0.00 ± 0.00	18.36 ± 0.93	0.00 ± 0.00	14.28 ± 0.82
ZZ	0.10 ± 0.10	0.19 ± 0.02	0.64 ± 0.32	3.12 ± 0.09	0.00 ± 0.00	3.06 ± 0.08
Triboson	0.00 ± 0.00	0.00 ± 0.00	0.02 ± 0.00	0.02 ± 0.01	0.00 ± 0.00	0.02 ± 0.01
Top	0.00 ± 0.00	0.00 ± 0.00	0.00 ± 0.00	0.96 ± 0.73	0.00 ± 0.00	0.49 ± 0.35
Top+Z	0.00 ± 0.00	0.02 ± 0.02	0.00 ± 0.00	0.38 ± 0.06	0.00 ± 0.00	0.27 ± 0.05
Z+Jets	0.00 ± 0.00	2.86 ± 1.39	0.00 ± 0.00	50.39 ± 7.11	0.00 ± 0.00	58.28 ± 9.55
Drell-Yan	0.00 ± 0.00	0.00 ± 0.00	0.00 ± 0.00	0.47 ± 0.24	0.00 ± 0.00	0.68 ± 0.37
Data	7		102		85	

Sample	Total		Region A	
	truth-matched $ll\tau\tau$	other	truth-matched $ll\tau\tau$	other
AZh (260 GeV)	0.0095 ± 0.0015	0.0344 ± 0.0024	0.0387 ± 0.0029	0.0010 ± 0.0004
AZh (400 GeV)	0.0088 ± 0.0014	0.0476 ± 0.0030	0.0273 ± 0.0025	0.0025 ± 0.0007
SM Higgs Zh	0.01 ± 0.00	0.03 ± 0.00	0.06 ± 0.01	0.00 ± 0.00
WW	0.00 ± 0.00	0.00 ± 0.00	0.00 ± 0.00	0.00 ± 0.00
WZ	0.00 ± 0.00	33.34 ± 1.25	0.00 ± 0.00	1.88 ± 0.30
ZZ	0.99 ± 0.06	6.37 ± 0.12	2.22 ± 0.09	0.20 ± 0.02
Triboson	0.02 ± 0.00	0.04 ± 0.01	0.12 ± 0.01	0.01 ± 0.00
Top	0.00 ± 0.00	1.45 ± 0.81	0.00 ± 0.00	0.00 ± 0.00
Top+Z	0.00 ± 0.00	0.67 ± 0.08	0.05 ± 0.02	0.03 ± 0.01
Z+Jets	0.00 ± 0.00	111.53 ± 11.99	0.00 ± 0.00	1.02 ± 0.72
Drell-Yan	0.00 ± 0.00	1.15 ± 0.44	0.00 ± 0.00	0.00 ± 0.00
Data	194		14	

Table 4.4: Number of events passing the $\tau_{lep}\tau_{had}$ channel selection in the Higgs sidebands control region. For a better overview, the events are also split in regions B ($\tau_{lep}\tau_{had}$ is SS, τ_{had} passes TauID), C ($\tau_{lep}\tau_{had}$ is OS, τ_{had} fails TauID) and D ($\tau_{lep}\tau_{had}$ is SS, τ_{had} fails TauID). Region A is defined such that all the requirements of the signal region are satisfied apart from the Higgs mass window constrain. Signal numbers assume $\sigma(gg \to A) \times BR(A \to Zh \to ll\tau\tau) = 1$ fb.

.

systematics, the template control region is altered in various ways and the shape of the nominal template is compared to that from the alternately defined regions. The alternate regions used are:

- R1: only same-sign events are included;
- R2: only opposite-sign events are included;
- R3: The tau passes loose ID;
- R4: Light lepton from Higgs decay passes loose ID;
- R5: Both τ_{had} and Higgs lepton pass loose ID.

In addition, a Z-sidebands region is defined where the cut on the mass of the Z leptons is inverted ($m_{\ell\ell} < 80$ GeV or $m_{\ell\ell} > 100$ GeV). The main fake-τ_{had} background is from Z+jets processes so this control region is less motivated than the h-sidebands region. However, there are still some Z+jets events that fall outside the Z-mass window cut and therefore the Z-sidebands control region can be used as a secondary cross-check on both the shape and normalization factor used in the template method. As shown in Figure 4.4, no strong systematic difference is observed between the shapes of the m_A^{rec} distributions in region A and template, for methods using either the h-sidebands or Z-sidebands. Therefore, no shape systematics in the background template are used. As can be seen in Figure 4.5, the background template in the Z-sidebands has a different shape to that of the h-sidebands and nominal template regions. This, coupled to the lower event population in the Z-sidebands, are additional motivations for using the h-sidebands to compute the normalization factor.

Table 4.5 contains the normalization factors of each region and their corresponding predicted fake-τ_{had} event yields in the signal region. Regions R1-R5 are also used to estimate systematic uncertainties on the normalization factor. The uncertainty in the normalization factor is mainly due to the limited number of events in region A of the h-sidebands. This

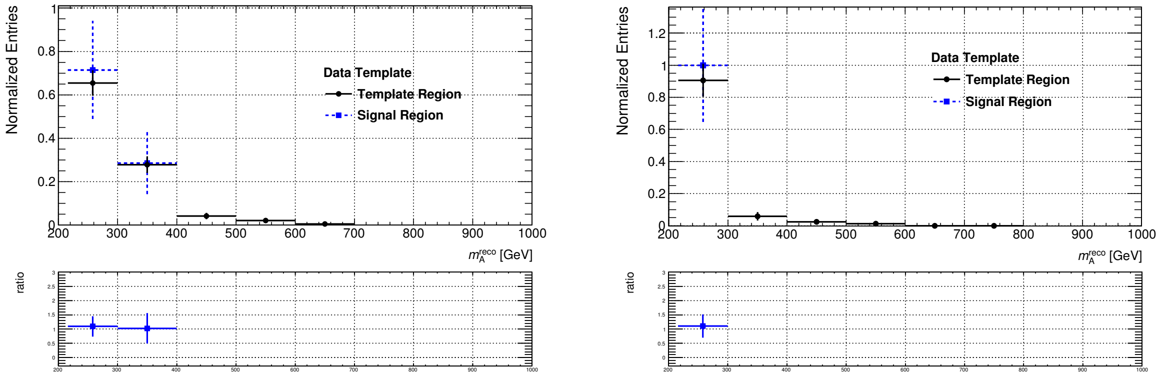

(a) Higgs sidebands

(b) Z sidebands

Figure 4.4: The shape of the reconstructed A boson mass, m_A^{rec}, for events passing in the h-sidebands region (a) and the Z-sidebands region (b) compared to Region A of Z-sidebands and h-sidebands, respectively. The truth-matched $ll\tau\tau$ events have been subtracted in both cases.

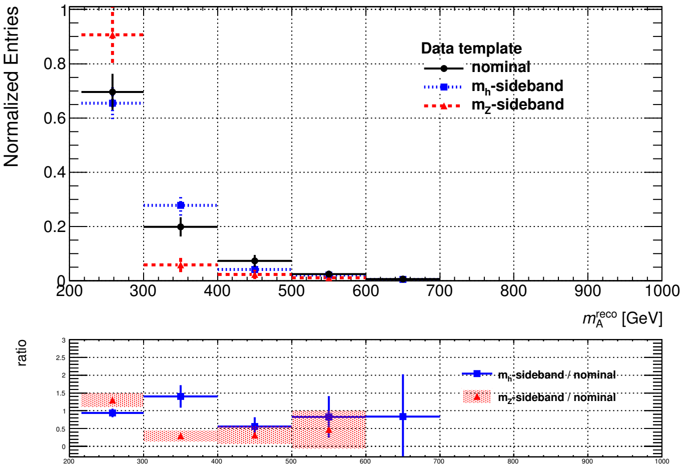

Figure 4.5: The shape of the reconstructed A boson mass, m_A^{rec}, for events passing in the Z-sidebands region, the h-sidebands region and the template region for the full selection. The truth-matched $ll\tau\tau$ events have been subtracted in both cases.

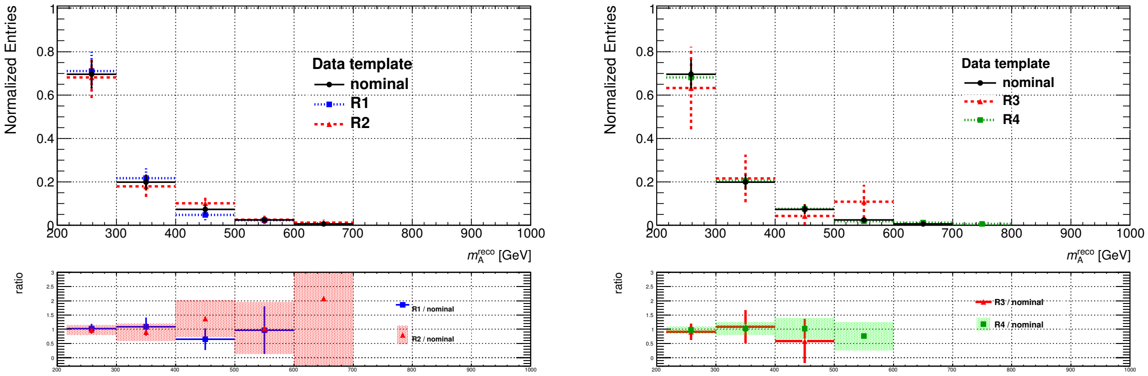

(a) R1 and R2

(b) R3 and R4

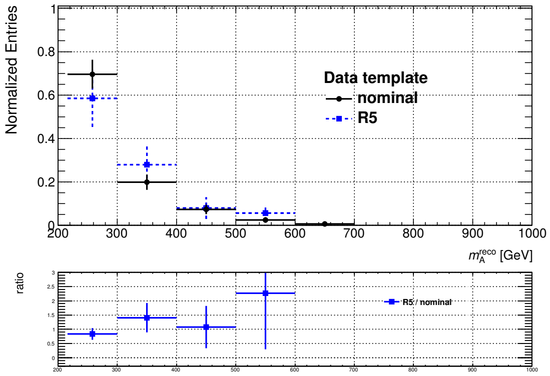

(c) R5

Figure 4.6: The default template shape compared to the shape that is obtained when using the R1 – R5 control regions. For more details see in the text.

Sample	Higgs sidebands		Z sidebands	
	Norm. factor	Predicted N_{fakes}	Norm. factor	Predicted N_{fakes}
Nominal	$5.73 \pm 2.01) \times 10^{-2}$	$9.15 \pm 0.73 \pm 3.2$	$(6.50 \pm 3.50) \times 10^{-2}$	$10.39 \pm 0.83 \pm 5.6$
R1	$(1.20 \pm 0.43) \times 10^{-1}$	$9.99 \pm 1.10 \pm 3.6$	$(1.04 \pm 0.57) \times 10^{-1}$	$8.65 \pm 0.95 \pm 4.7$
R2	$(1.09 \pm 0.39) \times 10^{-1}$	$8.38 \pm 0.97 \pm 3.0$	$(1.73 \pm 0.96) \times 10^{-1}$	$13.27 \pm 1.53 \pm 7.4$
R3	$(5.92 \pm 2.46) \times 10^{-1}$	$10.81 \pm 2.59 \pm 4.5$	1.39 ± 1.01	$25.37 \pm 6.07 \pm 18.5$
R4	$(3.39 \pm 1.12) \times 10^{-2}$	$10.68 \pm 0.60 \pm 3.5$	$(2.47 \pm 1.32) \times 10^{-2}$	$7.79 \pm 0.44 \pm 4.1$
R5	$(3.67 \pm 1.30) \times 10^{-1}$	$12.91 \pm 3.21 \pm 4.6$	$(4.74 \pm 2.19) \times 10^{-1}$	$16.64 \pm 2.85 \pm 7.7$

Table 4.5: Normalization factors and predicted event yields for the nominal and alternate definitions of the template region. Regions R4 and R5 have loose Higgs lepton in the control regions (but passing Medium ID in signal region). This study was conducted using a different generator for the diboson background, so there is a slight shift compared to quoted values in the text. The uncertainties quoted here are due to the data statistics and the finite number of generated MC. The uncertainty of the predicted yield that stems from the calculation of the normalization factor is shown second.

leads to a large uncertainty in the predicted yield, shown second in the quoted errors of Table 4.5. The first error quoted corresponds to the statistical variance expected for each predicted value and depends only on the number of events in the template region.

The variations in the normalization factor can be used to estimate a systematic uncertainty. Assuming a gaussian distribution around a central value, the normalization factor variance corresponds to approximately 1.5 events in the fake-τ_{had} events prediction. The final prediction of the nominal template method is then:

$$N_{fakes} = 9.44 \pm 0.76 \pm 3.13 \pm 1.5 = 9.4 \pm 3.5\,, \tag{4.5}$$

where the uncertainties are, in order of appearance, due to: the statistical uncertainty of the template, the limited number of events in the h-sidebands used to calculate the normalization factor, and the variance of the prediction. Thus, the final fake-τ_{had} background prediction has a 37% uncertainty which is, by a large margin, the largest systematic uncertainty of this analysis.

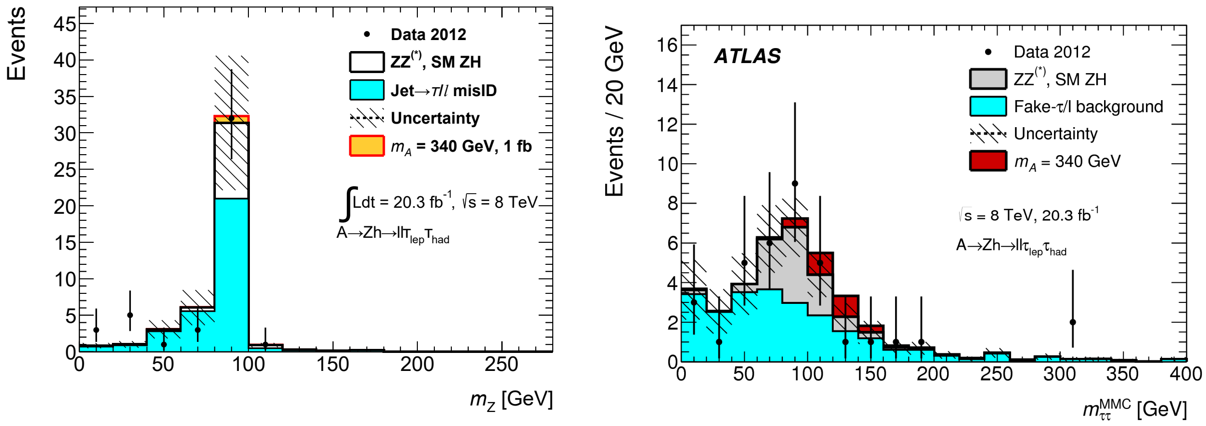

(a) m_Z

(b) m_h

Figure 4.7: The reconstructed Z (a) and h (b) boson masses. Both distributions are for the full signal region selection apart from the Z and h mass window requirements, respectively. Events with true τ_{had} are taken from simulation and events with jets misidentified as τ_{had} are estimated using the template method.

Higgs and Z mass distributions are shown in Figure 4.7, after the full selection but each without its respective mass window cut. Kinematic distributions for the optimized selection in the signal region can be found in Figure 4.8. The uncertainty error band includes both systematic and statistical uncertainties. The background prediction is in excellent agreement with observed data.

4.5 Systematic Uncertainties

This section describes only systematic uncertainties pertinent to the use of simulated samples, as those related to the data-driven background prediction of the template method are found in the previous section. Because the uncertainty in the template method is high (37%), the smaller uncertainties described here have a small impact on the final result. A summary of the final uncertainties on simulated background, simulated signal and fake-τ_{had} background is found in Table 4.13.

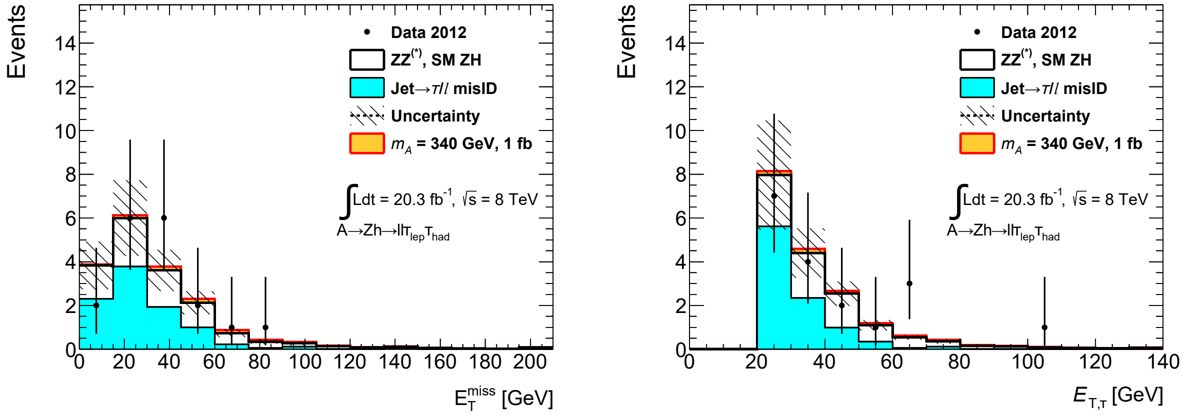

(a) E_T^{miss} (b) τ E_T

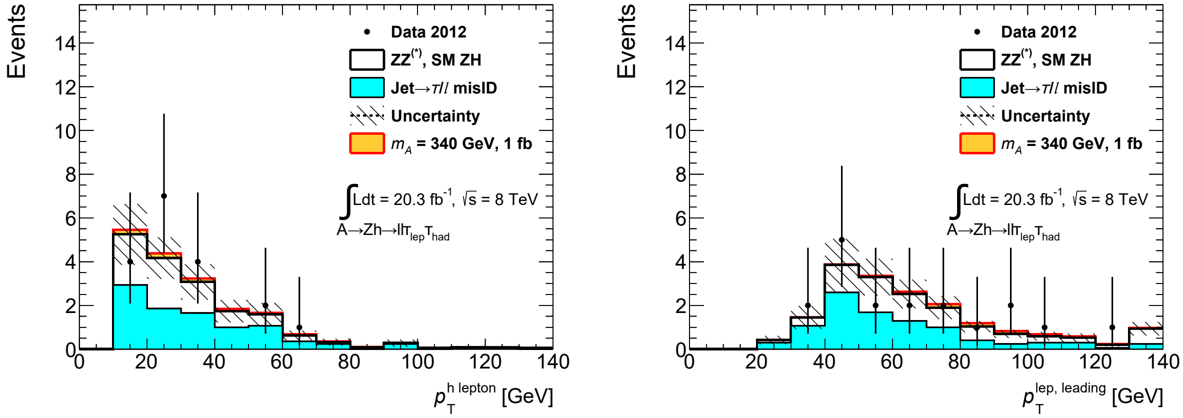

(c) h lepton p_T (d) leading Z lepton p_T

Figure 4.8: Comparisons of the distributions of kinematic variables for the full background prediction, observed data and a $m_A = 340$ GeV signal sample in the signal region.

4.5.1 Luminosity and theoretical uncertainties

There is a 2.8% uncertainty on the measured integrated luminosity of the data. This uncertainty is applied to all simulated samples as it translates to an uncertainty in the luminosity scaling that is applied to these samples.

The simulated samples also have theoretical uncertainties. They can be related to production cross sections, initial and final state radiation (ISR, FSR), the factorization and renormalization scheme used in hadronization processes, and the choice of parton distribution function (PDF) [54]. The uncertainties in the normalization and PDF have already been estimated in [55, 56], and for this analysis are found to have an effect of at most a few percent.

4.5.2 Detector-related uncertainties

The simulated detector response and software performance in Monte Carlo generated events has several systematic uncertainties. They can be related to:

- the reconstruction, identification and electron-veto efficiency of hadronic taus (τ_{had}-ID);
- the reconstruction of the energy of the τ_{had}, referred to as the τ_{had} energy scale (TES);
- the efficiencies of the lepton triggers used, as well as the subsequent reconstruction, isolation, identification and energy scale of simulated electrons and muons (Trig_Mu, Mu_EFF, Mu_ES, Trig_El, El_EFF, El_ES);
- the reconstruction of jet energies and resolution (JES, JER);
- pileup uncertainties due to the reweighting of MC samples to match the average interaction per bunch crossing ($\langle\mu\rangle$) profile of data events (PU);
- the E_T^{miss} calculation for simulated events (MET). Since the E_T^{miss} calculation is dependent on all other physical objects, their respective uncertainties all impact the E_T^{miss}

uncertainty.

The dominant detector-related uncertainties are related to the TES and TauID, being as high as 6%. Similar to all other uncertainties associated with simulated samples, they are dwarfed by the overall 37% uncertainty in the fake-τ_{had} data-driven background prediction.

Sample	LUMI		EL_EFF		EL_ES		JER		JES		MET		Mu_EFF	
	up %	dn %	up %	dn %	up %	dn %	up %	dn %	up %	dn %	up %	dn %	up %	dn %
220	2.8	-2.8	1.3	-1.3	-1.1	-1.2	0.4	0.4	0.5	-0.7	0.1	-0.1	1.1	-1.1
240	2.8	-2.8	1.3	-1.3	0.5	-0.5	-0.1	0.1	-0.4	-0.4	-0.2	-0.5	1.1	-1.1
260	2.8	-2.8	1.3	-1.3	0.5	0.6	-0.04	-0.04	-0.4	-0.5	-0.4	-0.3	1.1	-1.1
300	2.8	-2.8	1.4	-1.4	0.2	0.5	0.03	0.02	-0.2	-0.6	0.1	0.1	1.1	-1.1
340	2.8	-2.8	1.4	-1.3	0.7	0.4	-0.1	-0.1	0.2	0.3	0.1	0.1	1.1	-1.1
350	2.8	-2.8	1.4	-1.4	-0.1	-0.3	-0.2	-0.2	0.3	0.1	0.1	0.1	1.1	-1.1
400	2.8	-2.8	1.4	-1.4	0.3	0.2	-0.2	-0.2	-0.1	0.3	0.1	0.2	1.1	-1.1
500	2.8	-2.8	1.5	-1.5	0.1	0.1	-0.2	-0.2	-0.1	-0.1	0.1	0.1	1.1	-1.1
800	2.8	-2.8	1.5	-1.5	-0.2	0.3	-0.1	-0.1	0.3	0.4	-0.1	-0.1	1.1	-1.1
1000	2.8	-2.8	1.6	-1.6	0.2	0.2	-0.1	-0.1	0.7	0.7	0.1	0.4	1.2	-1.1
MC Background	2.8	-2.8	1.5	-1.5	4.8	8.9	-2.6	-2.6	-4.9	0.3	2.0	-0.4	1.1	-1.1

Sample	Mu_ES		PU		TES		TRIG_El		TRIG_Mu		τ_{had}-ID		
	up %	dn %	up %	dn %	up %	dn %	up %	dn %	up %	dn %	up %	dn %	
220	-0.4	0.1	3.9	-4.4	1.3	-1.0	0.1	-0.1	0.5	-0.5	3.3	-3.3	
240	0.2	0.1	3.7	-4.1	0.3	-0.7	0.1	-0.1	0.5	-0.5	3.3	-3.3	
260	-0.5	0.1	4.0	-4.5	0.8	-1.0	0.1	-0.1	0.5	-0.5	3.3	-3.3	
300	0.1	-0.2	3.8	-4.3	0.6	-0.8	0.1	-0.1	0.5	-0.5	3.3	-3.3	
340	-0.1	0.1	4.0	-4.5	0.9	-1.0	0.1	-0.1	0.5	-0.5	3.3	-3.3	
350	0.1	0.2	4.0	-4.5	0.6	-0.6	0.1	-0.1	0.5	-0.5	3.3	-3.3	
400	-0.1	0.1	4.0	-4.5	0.6	-0.5	0.1	-0.1	0.5	-0.5	3.3	-3.3	
500	0.1	0.1	4.1	-4.5	0.5	-0.7	0.1	-0.1	0.5	-0.5	3.3	-3.3	
800	0.1	0.1	3.8	-4.3	0.5	-0.2	0.1	-0.1	0.5	-0.5	3.3	-3.3	
1000	-0.3	-0.1	3.9	-4.4	0.2	-0.2	0.1	-0.1	0.5	-0.5	3.3	-3.3	
MC Background	1.5	-0.4	-1.0	1.0	6.0	-2.6	0.1	-0.1	0.5	-0.5	3.2	-3.2	

Table 4.6: Table showing the up and down detector systematic fluctuations of the $\tau_{lep}\tau_{had}$ MC signal and background samples after full selection, along with the corresponding statistical uncertainty

4.5.3 Signal modelling uncertainties

The kinematics of events generated with Monte Carlo do not match perfectly with those of events in data. This mismodelling in the simulation can lead to a different acceptance of our signal events, and is thus accounted for as an uncertainty on the normalization of our signal samples.

To gauge the impact of the ISR uncertainty, a variation of ±20% around the nominal value is assumed and its impact assessed. The effect of doubling and halving the factorization/renormalization factor is investigated using Madgraph5. The uncertainty on the nominal PDF is estimated by checking the effect of replacing it with two others: `MSTW2008lo68cl` [57] and `NNPDF21_lo_as_0119_100` [58]. The effect of using `MSTW2008lo68cl` as PDF is shown in Table 4.12, and similarly in Table 4.11 for `NNPDF21_lo_as_0119_100`. Tables 4.7 and 4.8 show the uncertainties due to changes in the factorization/renormalization scale. The second column is the nominal signal acceptance, while the third column is the acceptance after variation. The fourth column is the the ratio between the acceptance after variation and the nominal acceptance. The numbers in the last column are the difference between the nominal acceptance and acceptance after a $\pm 1\sigma$ variation of the combined statistical uncertainty of the two acceptances. Tables 4.9 and 4.10 show the uncertainty in the $\tau_{lep}\tau_{had}$ channel arising from variations of ISR. The final total uncertainty due to ISR, Fac./Renorm. and choice of PDFs is 2.4%.

sample name	nominal acceptance	fac/renorm up acceptance	ratio	# of sigma diff
220 GeV	0.26510	0.2631	0.9925	0.3706
260 GeV	0.32160	0.3196	0.9938	0.3500
340 GeV	0.34465	0.3500	1.0155	0.9169
500 GeV	0.40955	0.4053	0.9896	0.7064
1000 GeV	0.52285	0.5229	1.0001	0.0082

Table 4.7: Factorization/Renormalization shift up uncertainy on the signal acceptance.

4.6 Results

Table 4.14 shows the final event numbers after unblinding of the signal region. The final distribution of m_A^{rec} , after applying our complete background prediction methodology and

sample name	nominal acceptance	fac/renorm down acceptance	ratio	# of sigma diff
220 GeV	0.26510	0.2607	0.9834	0.8169
260 GeV	0.32160	0.3291	1.0233	1.3058
340 GeV	0.34465	0.3463	1.0048	0.2833
500 GeV	0.40955	0.3974	0.9703	2.0239
1000 GeV	0.52285	0.5291	1.0120	1.0221

Table 4.8: Factorization/Renormalization shift down uncertainy on the signal acceptance.

sample name	nominal acceptance	ISR up acceptance	ratio	# of sigma diff
220 GeV	0.26510	0.26185	0.98774	0.73777
260 GeV	0.32160	0.32050	0.99658	0.23561
340 GeV	0.34465	0.34890	1.01233	0.89297
500 GeV	0.40955	0.40075	0.97851	1.79262
1000 GeV	0.52285	0.51330	0.98173	1.91134

Table 4.9: Signal acceptance uncertainty due to upward shift of ISR.

sample name	nominal acceptance	ISR down acceptance	ratio	# of sigma diff
220 GeV	0.26510	0.2577	0.9721	1.6842
260 GeV	0.32160	0.3269	1.0163	1.1216
340 GeV	0.34465	0.3429	0.9948	0.3790
500 GeV	0.40955	0.4033	0.9846	1.2827
1000 GeV	0.52285	0.5158	0.9864	1.4211

Table 4.10: Signal acceptance uncertainty due to downward shift of ISR.

sample name	nominal acceptance	change PDF	ratio	# of sigma diff
220 GeV	0.26510	0.2607	0.9834	0.8169
260 GeV	0.32160	0.3095	0.9624	2.1297
340 GeV	0.34465	0.3407	0.9885	0.6799
500 GeV	0.40955	0.4026	0.9830	1.1561
1000 GeV	0.52285	0.5144	0.9838	1.3807

Table 4.11: Signal acceptance differences from using `NNPDF21_lo_as_0119_100`.

sample name	nominal acceptance	change PDF	ratio	# of sigma diff
220 GeV	0.26510	0.2670	1.0072	0.3509
260 GeV	0.32160	0.3177	0.9879	0.6832
340 GeV	0.34465	0.3400	0.9865	0.8006
500 GeV	0.40955	0.3988	0.9738	1.7900
1000 GeV	0.52285	0.5116	0.9785	1.8381

Table 4.12: Signal acceptance differences from using `MSTW2008lo68cl`.

$\tau_{lep}\tau_{had}$ channel systematics		
Sample	Systematic	Uncertainty (%)
MC background	SM h tautau BR	0.60
MC background	luminosity	2.80
MC background	tau ID	0.40
MC background	PDF gg	0.50
MC background	pdf Higgs qq	0.40
MC background	PDF qq	3.30
MC background	QCD scale gg	1.70
MC background	QCD scale qq	3.30
MC background	QCD scale Vh	0.30
Total (for Background)		5.79
Fake background	Data driven norm.	37.70
Signal	electron efficiency	1.40
Signal	electron energy scale	0.50
Signal	ATLAS ggAZh Acc ISR	0.50
Signal	ATLAS ggAZh Acc PDF	2.30
Signal	ATLAS ggAZh Acc Scale	0.20
Signal	JER	0.30
Signal	JES	0.60
Signal	luminosity	2.80
Signal	muon trigger	0.50
Signal	muon efficiency	1.10
Signal	muon scale	0.20
Signal	pileup	4.30
Signal	tau ID	3.30
Signal	tau energy scale	0.80
Total (for Signal)		6.90

Table 4.13: Overview of the $\tau_{lep}\tau_{had}$ channel systematic uncertainties as implemented in the fit model.

.

including all statistical and systematic uncertainties, is shown in Figure 4.9. The observed data is in good agreement with the predicted background and no statistically significant excess is observed. Thus, upper limits on the signal production cross section times branching ratio are derived at 95% confidence level (see Figure 4.10) using the modified frequentist approach ($\mathtt{CL}_S$), as decribed in Appendix B.

Regions of the parameter space that have signal predictions incompatible with these limits are shown in Figure 4.11 for both type-I and type-II 2HDM. The interpretation assumes the heavy Higgs masses are degenerate, and that the mixed mass term in the 2HDM lagrangian is given by $m_{12}^2 = m_A^2 \tan\beta/(1+\tan^2\beta)$ (see Equation 2.22).

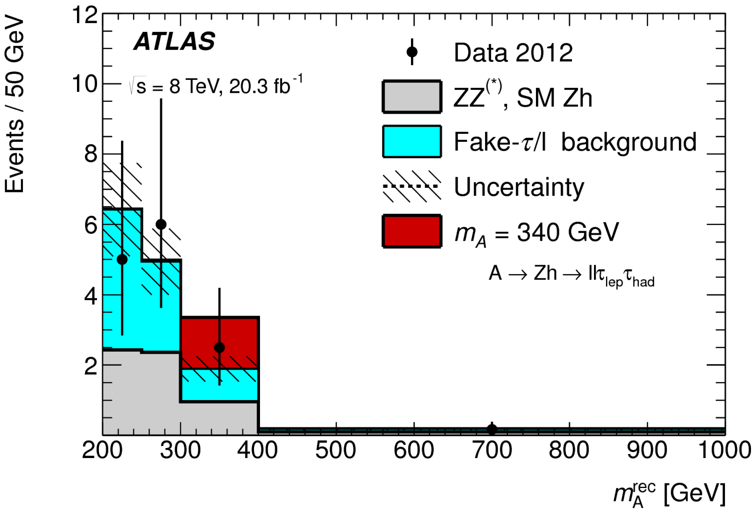

Figure 4.9: The reconstructed A boson mass, m_A^{rec}, for the full $\tau_{lep}\tau_{had}$ selection. The truth-matched background from simulation is shown stacked on the data-normalized template. The signal point shown here corresponds to $\sigma(gg \rightarrow A) \times BR(A \rightarrow Zh \rightarrow ll\tau\tau) = 1$ fb^{-1}.

Sample	$\ell\ell\tau_{lep}\tau_{had}$
ZZ	6.97 ± 0.17 ± 0.40
SM Zh	0.85 ± 0.02 ± 0.09
Others	0.10 ± 0.01 ± 0.01
Data-driven	9.44 ± 0.76 ± 3.54
Sum	17.4 ± 0.8 ± 3.6
Data	18
Signal	0.54 ± 0.04

Table 4.14: Final event yields of the $A \to Zh \to \ell\ell\tau_{lep}\tau_{had}$ search. The signal is given for a mass of 300 GeV, and assuming a cross section times branching ratio of 1 fb^{-1}.

.

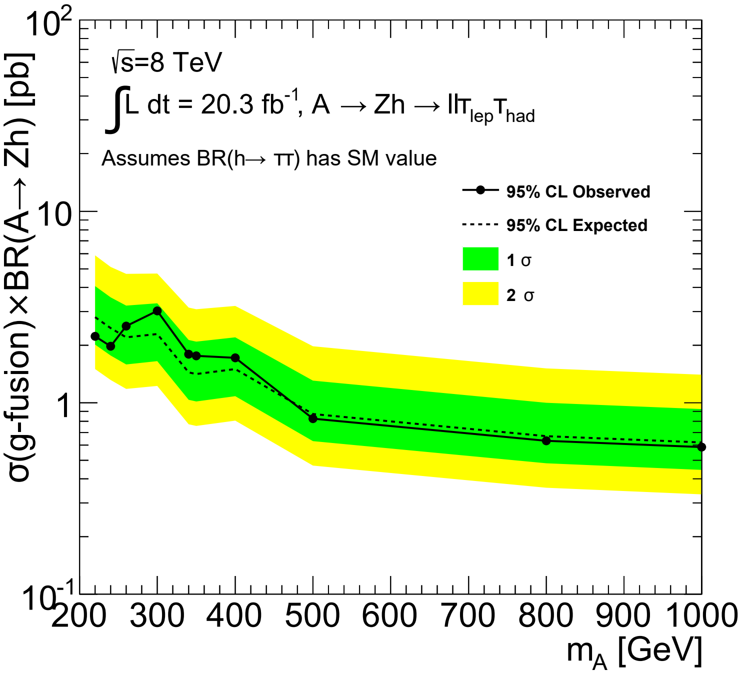

Figure 4.10: Expected and observed 95% CL upper limits of σ(gluon-fusion) × BR($A \to Zh \to ll\tau_{lep}\tau_{had}$) as a function of m_A.

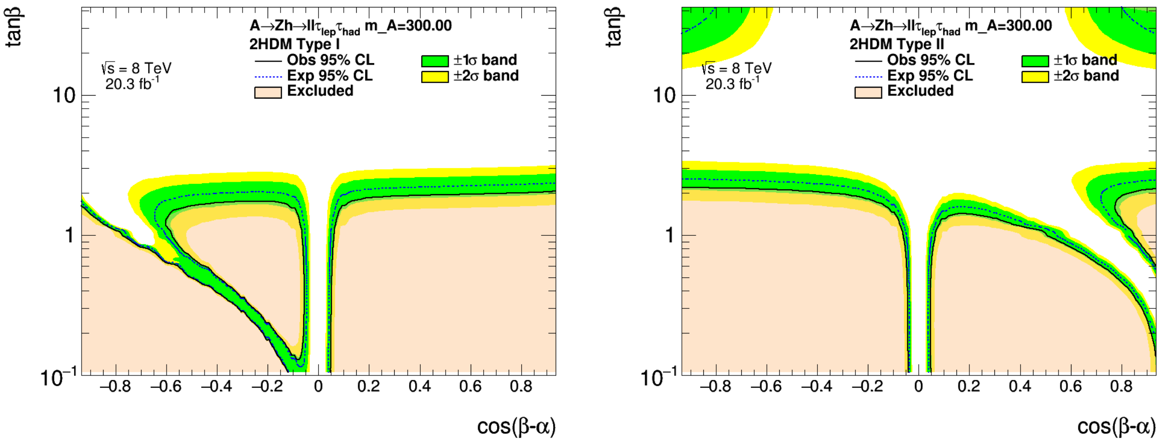

(a) (b)

Figure 4.11: Excluded parameter space of type-I (a) and type-II (b) 2HDM derived from $A \to Zh \to \tau_{lep}\tau_{had}$ search result.

This marks the first time the $A \rightarrow Zh \rightarrow \ell\ell\tau\tau$ search was done in ATLAS. The result was published combined with four other decay channels: $\ell\ell\tau_{lep}\tau_{lep}$, $\ell\ell\tau_{had}\tau_{had}$, $\nu\nu bb$ and $\ell\ell bb$ [59]. The combined analysis also did not find any significant deviations from the SM prediction. The combined results were interpreted for general types of 2HDM, leading to large exclusions of the allowed parameter space, as shown in Figure 4.12.

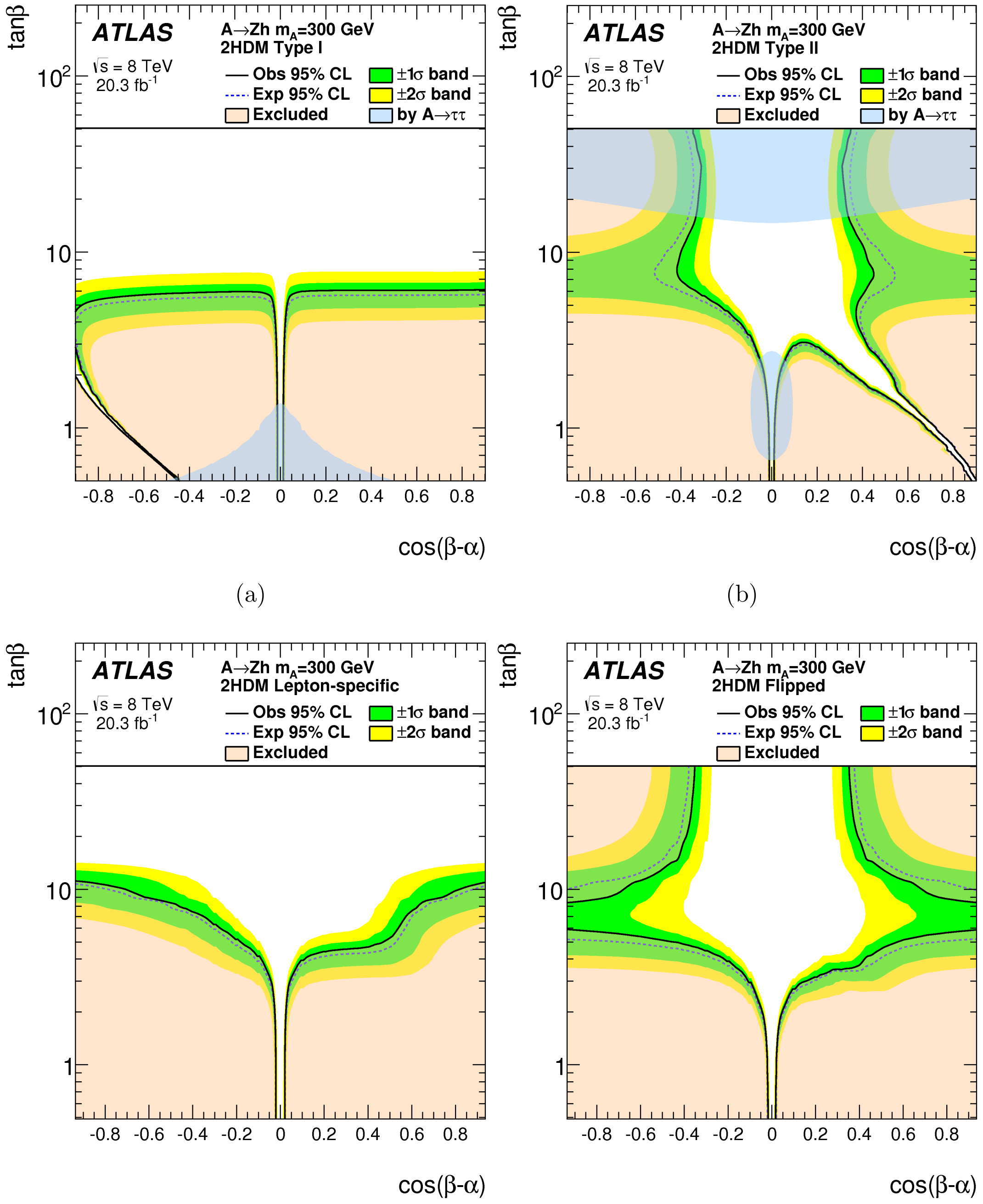

(a) (b)

(c) (d)

Figure 4.12: Exclusions in the $\cos(\beta - \alpha) - \tan\beta$ plane of the combined ($\ell\ell\tau\tau$, $\nu\nu bb$, $\ell\ell bb$) $A \to Zh$ search for Type-I (a), Type-II (b), Lepton-specific (c) and Flipped (d) 2HDM. The blue shaded area is the exclusion provided by the Run-1 $A \to \tau\tau$ search result. Plots from Reference [59].

Chapter 5

$A/H \rightarrow \tau_{lep}\tau_{had}$

In this chapter we describe the search for heavy MSSM-compatible A,H neutral Higgs bosons decaying to a tau pair using 3.2 fb^{-1} of LHC proton-proton collision data at a center-of-mass energy of 13 TeV collected with the ATLAS detector. The search is done in the $\tau_{lep}\tau_{had}$ final state, where one tau decays leptonically and the other hadronically. As discussed in Chapter 2, the MSSM Higgs couplings to down-type fermions are enhanced, especially for high values of $\tan\beta$. Thus, decays to $b\bar{b}$ and $\tau\tau$ dominate. However, the $b\bar{b}$ final state is disfavored by the large QCD background at the LHC. Another consequence is that the b-associated production mode is enhanced, so that a gain in sensitivity can be obtained by categorizing the signal region according to the presence or absence of b-tagged jets. Here we present the search for $A/H \rightarrow \tau\tau$ in the b-veto category of the $\tau_{lep}\tau_{had}$ final state.

5.1 Samples

5.1.1 Data Sample

This analysis uses proton-proton collision data recorded by the ATLAS detector during 2015 (Run-2) at a center-of-mass energy of 13 TeV. Since this channel relies on vetoing events with b-tagged jets, data where the IBL was turned off were not included. This leads to a total integrated luminosity of 3.2 fb^{-1}.

5.1.2 Monte Carlo Simulated Samples

Monte Carlo simulated samples were generated for W+jets, Z+jets, $t\bar{t}$, single top and diboson production. The W+jets and Z+jets events were generated using POWHEG [60] and showered with Pythia8 [61]. Separate high-mass vector-boson samples were generated

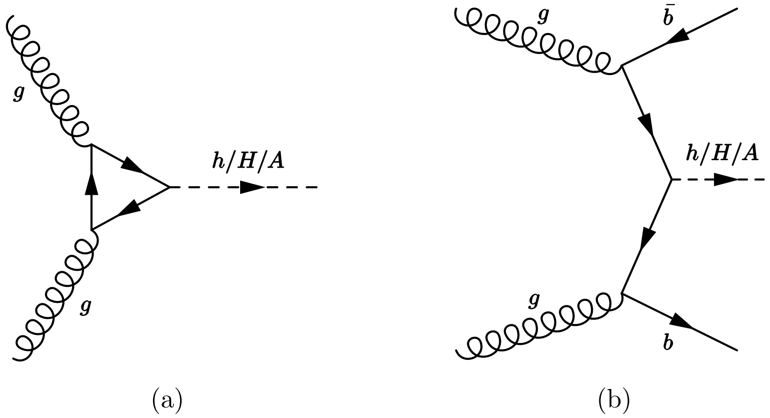

Figure 5.1: Lowest order Feynman diagrams for gluon fusion (a) and b-associated production (b) of a neutral MSSM Higgs boson.

for off-shell decays. POWHEG was also used for $t\bar{t}$ and single top samples, but with parton showering done with Pythia6 [62]. Diboson samples were both generated and showered using SHERPA [41].

As mentioned before, signal events can originate from two different processes: gluon-fusion and b-associated production (as shown in Figure 5.1). For b-associated production, the event generation was done with `MadGraph5_aMC@NLO 2.1.2` [63, 64] for Higgs masses ranging from 200 to 1200 GeV. Samples from gluon-fusion production were simulated using POWHEG. Both signal types had their parton showering and hadronisation simulated with Pythia 8.2 [61]. Due to particularities of how `MadGraph5_aMC@NLO 2.1.2` weighs its events, a large number of b-associated signal events are needed. To this end, the faster simulation framework ALTFAST-II was used [65]. The simulated detector response of all generated samples was done with GEANT4 [45], except for bbH signal samples since they use the faster simulation provided by ALTFAST-II.

5.2 Reconstruction

The signal events in this search have electrons, muons and taus in the final state. We also make use of b-tagging to veto events with b-tagged jets, and rely on missing transverse energy to refine our signal region selection and define control regions. Similarly to the $A \to Zh$ analysis, it is crucial to have well developed reconstruction software to identify low-level detector signals with physical particles.

5.2.1 Electrons

Electron candidates originate from energy deposits in the EM calorimeter that have charged-particle tracks in the Inner Detector compatible with them. A likelihood-based identification algorithm is used to reject misidentified jets or events from photon conversion [66]. Three quality levels are defined and candidates passing the "loose" criteria are considered for overlap removal. We also require the candidate to have $E_T > 30$ GeV (where $E_T \equiv E_{cluster}/\cosh(\eta_{track})$) and to be in the $|\eta| < 2.47$ region. A "gradient" isolation criteria is required where the surrounding cone (defined by $\Delta R < 0.2$) must have 1-10% of the electron energy. This threshold varies with electron transverse momentum, being 90% (99%) efficient at $p_T = 25$ (60) GeV.

5.2.2 Muons

Muon candidates are reconstructed from tracks in the muon spectrometer. All candidates must have $p_T > 30$ GeV and $|\eta| < 2.5$. Muons in ATLAS are reconstructed from several different algorithms [67]. Similarly to electrons, they are required to be isolated with a "gradient" criteria, with efficiency of 95 (99)% at $p_T = 25$ (60) GeV, and pass a "loose" quality requirement.

5.2.3 Jets

For Run-2, jets are again reconstructed using the anti-kt algorithm and cone size $R = 0.4$ [50]. For better pileup suppresion the Jet Vertex Tagger (JVT) algorithm is used [68]. The JVT is a multivariate classifier that uses jet energy, tracking and vertexing information of the reconstructed jet to assign a score that reflects the probabilty the object is not due to pileup. Specifically, we require a JVT score greater than 0.64 for jets with $p_T < 50$ GeV and $|\eta| < 2.4$.

5.2.4 b-tagging

Jets flagged as originating from b-hadrons are called b-tagged jets. We require them to pass all quality criteria that are applied to regular jets, and the MV2c20 algorithm is used for identifying b-tagged jets [69]. This algorithm is tuned to be 70% efficient in selecting b-originated jets from a $t\bar{t}$ sample, and has mis-identification rates of 10%, 4% and 0.2% when applied on c-jets, τ-jets and light-quark or gluon initiated jets, respectively.

5.2.5 Taus

Taus that decay hadronically are nearly always characterized by one or three tracks, corresponding to the number of charged pions in the hadronic decay. Tau decays also produce neutrinos and neutral pions, and are characterized by a small-angle shower in the calorimeter and few tracks. All jets with $p_T > 10$ GeV are initially considered to be τ_{had} candidates. The tau candidates must then have either have one or three tracks, have a visible transverse momentum greater than 20 GeV, pseudo-rapidity less than 2.5, and be outside the calorimeter transition region ($1.37 < |\eta| < 1.52$). Hadronic taus with one or three tracks are also called 1-prong or 3-prong taus, respectively. The TauID classifier used in Run-1 has been updated in Run-2 to cope with the different pileup profile, as well as improve rejection through the use of new kinematic variables. The specific updates to the Run-2 TauID algorithm can be found in Appendix A. Three quality criteria are defined for hadronic taus and the "medium" working point is chosen for the final analysis. However, for object overlap removal only the leading tau is used, regardless of TauID quality, as long as it has $p_T > 10$ GeV and $|\eta| < 2.5$. Electrons are also often mis-identified as hadronically decaying taus. To reduce the e-to-τ_{had} fake rate, taus that geometrically overlap with loosely identified electrons are discarded. The quality threshold on the electron candidates is such that a 95 % efficiency for reconstructing hadronic taus is obtained in a $Z \rightarrow \tau\tau$ sample.

5.2.6 Missing Transverse Energy

Similar to the $A \rightarrow Zh$ analysis, the E_T^{miss} is defined as the opposite of the $\vec{p}_T$ sum of all reconstructed objects in an event [70]. This analysis uses the Track-based Soft Term (TST) algorithm [71], which uses ID tracks from the primary vertex to create a "soft term" that improves the resolution and performance of the E_T^{miss} calculation over a wide range pileup of scenarios.

5.2.7 Object Overlap Removal

The following priority is used when removing multiple objects that overlap:

- jets within a $\Delta R = 0.2$ cone of the hadronically-decaying τ with highest transverse momentum are excluded;
- jets within a $\Delta R = 0.4$ cone of electrons or muons are excluded;
- hadronic taus within a $\Delta R = 0.2$ cone of electrons or muons are excluded;
- electrons within a $\Delta R = 0.2$ cone of muons are excluded.

For overlap removal purposes, a lower p_T requirement of 15 GeV for electrons and 7 GeV for muons is imposed.

5.3 *Event Selection*

This section contains a description of the selection criteria used in the $H/A \rightarrow \tau_{lep}\tau_{had}$ b-veto analysis. The $\tau_{lep}\tau_{had}$ b-veto channel must have one light lepton and one hadronic tau in the final state, both passing "medium" identification requirements, and no b-tagged jets. Due to their higher efficiencies and lower systematic errors, single electron or single muon triggers are used over hadronic tau triggers. The transverse momentum of the light lepton (tau) must be greater than 30 (25) GeV. Events are also required to have a vertex with at least four associated tracks. An $|\eta| < 2.3$ cut is applied to the τ_{had} for two reasons, the first being that the high η region has only a small fraction of signal events. The second reason is that there is a significant amount of misidentified $Z \rightarrow ee$ events that is hard to estimate due to the fact that the e-to-τ_{had} fake rate in this region is very poorly modeled in simulation. Finally, the electron and tau must have opposite-sign charges. Events where the τ_{lep} decays to an electron are said to belong to the electron channel ($e\tau_{had}$), and events where τ_{lep} decays to a muon make up the muon channel ($\mu\tau_{had}$). The discriminant variable used in this analysis is the total transverse mass, m_T^{tot}, for which a description can be found at the end of this section.

5.3.1 $e\tau_{had}$

For the $e\tau_{had}$ channel, the triggers `e24_lhmedium_L1EM20VH`, `e60_lhmedium` and `e120_lhloose` are used (in data, `e24_lhmedium_L1EM20VH` is replaced by `e24_lhmedium_L1EM18VH`). The electron must be trigger-matched, i.e. overlap with the object that triggered the event. All electrons must pass "medium" likelihood identification, and events with two or more "loose" electrons or muons are vetoed in order to reject $Z/\gamma^* \rightarrow \ell\ell$ production ("dilepton veto"). In spite of the selection cuts above, there is still a significant fraction of $Z \rightarrow ee$ events misidentified in our signal region, so a Z-mass veto is applied to the reconstructed visible mass of the $\tau_{lep}\tau_{had}$ system ($m_{\tau\tau}^{vis} < 80$ GeV or $m_{\tau\tau}^{vis} > 110$). A more detailed description of the treatment of $e \rightarrow \tau_{had}$ background events is found in Section 5.4.2.

5.3.2 $\mu\tau_{had}$

A $\mu\tau_{had}$ event must pass at least one of the `mu20_iloose_L1MU15` and `mu50` triggers. The same dilepton veto as in the $e\tau_{had}$ channel must be satisfied, and trigger-matching of the muon is again required. The muon must pass the "medium" quality identification requirement. Again, the muon and tau must have opposite-sign charges.

5.3.3 Selection Optimization

The cuts above are sufficient for selecting our signal events, but they do not yet take advantage of the kinematic differences between signal and background processes. The two cuts below significantly improve the sensitivity of this channel:

- $\Delta\phi(\tau,\ell) > 2.4$;
- $m_T(\ell, E_T^{miss}) < 40$ GeV, where $m_T(\ell, E_T^{miss}) \equiv \sqrt{2p_{T,\ell}E_T^{miss}(1-\cos\Delta\phi(\ell, E_T^{miss}))}$.

The $\Delta\phi(\tau,\ell) > 2.4$ cut is applied because the τ's from the Higgs boson decay in an approximately back-to-back topology. The second cut on the transverse mass exploits the fact that m_T peaks near the W boson mass (80 GeV) for W+jets background events. Signal events, however, have low transverse mass because $\cos\Delta\phi(\ell, E_T^{miss})$ tends to be low. This occurs because leptonically-decaying taus have two neutrinos and hadronically-decaying taus have one, causing the reconstructed E_T^{miss} to be approximately collinear to the light lepton. This behavior can be seen in Figure 5.2. Event yields at different stages of the selection cutflow can be found in Tables 5.1-5.4.

5.3.4 Total Transverse Mass

The reconstruction of the tau pair mass is essential to obtaining a good separation between signal and background events. However, because of the presence of neutrinos from the tau decays, mass reconstruction can be difficult. The final discriminant chosen is the total

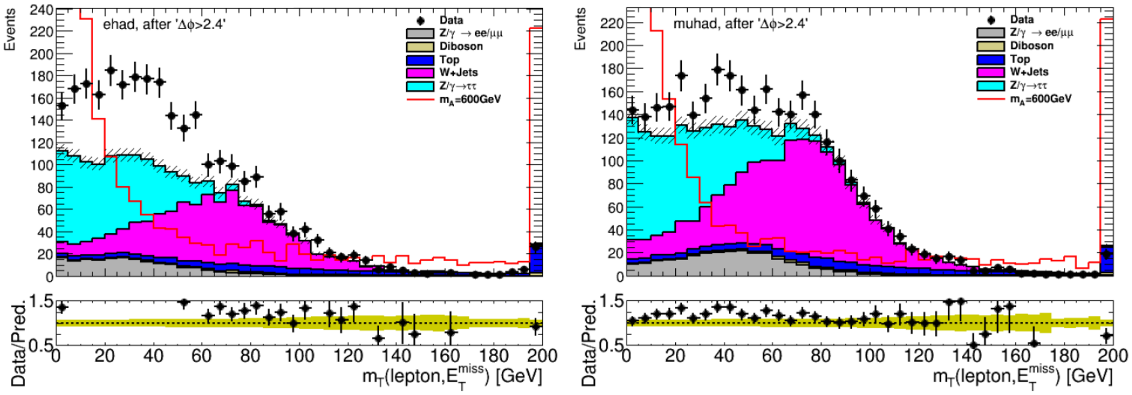

(a)

(b)

Figure 5.2: Distribution of the transverse mass $m_T(\ell, E_T^{miss})$ for the $e\tau_{had}$ (a) and $\mu\tau_{had}$ (b) channels. No estimate for the multi-jet background is shown at this stage, which is why the plotted background does not fully account for the observed data.

transverse mass m_T^{tot}, given by:

$$m_T^{tot} \equiv \sqrt{m_T^2(E_T^{miss}, \tau_1^{vis}) + m_T^2(E_T^{miss}, \tau_2^{vis}) + m_T^2(\tau_1^{vis}, \tau_2^{vis})}, \tag{5.1}$$

where $m_T(a, b)$ is defined as:

$$m_T(a, b) \equiv \sqrt{2p_T^{vis}(a)p_T^{vis}(b)(1 - \cos\Delta\phi(a, b))} \tag{5.2}$$

A few other mass reconstruction techniques were investigated, such as the MMC, but were found to have lower signal/background separation power. The total transverse mass has higher discriminating power because multi-jet background events (i.e. events from QCD processes) have low E_T^{miss} values and, therefore, low m_T^{tot}.

5.4 Background Estimation

Events from several background processes can pass our signal selection. Similarly to the $A \to Zh$ analysis of Chapter 4, it is useful to divide them into categories based on whether the lepton or τ_{had} have or have not been correctly identified ("true" or "fake"). The background categories, and the processes that populate them, are:

Table 5.1: Electron channel cutflow. The predictions correspond to a luminosity of 3.2 fb^{-1}. The errors are due solely to the finite number of simulated events.

Cut: Backgrounds		Top			$Z \to \tau\tau$+jets	
	Events	jet $\to \tau_{had}$ (%)	$e \to \tau_{had}$ (%)	Events	jet $\to \tau_{had}$ (%)	$e \to \tau_{had}$ (%)
pre-selection	3316.2 ± 11.2	27.7	2.8	7102.3 ± 54.5	0.9	0.0
$\Delta\phi(\tau, \ell) > 2.4$	1354.4 ± 7.1	22.0	2.6	5516.2 ± 47.8	0.7	0.0
$m_T(\ell, E_T^{miss})$	221.0 ± 2.9	33.4	3.2	4286.2 ± 42.2	0.7	0.0
b-veto	51.9 ± 1.4	36.1	2.0	4216.5 ± 41.7	0.7	0.0
Cut: Backgrounds		W+jets			Diboson	
	Events	jet $\to \tau_{had}$ (%)	$e \to \tau_{had}$ (%)	Events	jet $\to \tau_{had}$ (%)	$e \to \tau_{had}$ (%)
pre-selection	12258.0 ± 146.4	99.4	0.0	524.4 ± 5.6	22.0	3.6
$\Delta\phi(\tau, \ell) > 2.4$	6340.7 ± 105.5	99.3	0.0	261.1 ± 3.6	15.8	3.9
$m_T(\ell, E_T^{miss})$	1142.8 ± 44.8	99.5	0.0	53.3 ± 1.8	20.3	8.5
b-veto	1116.3 ± 44.0	100.0	0.0	51.2 ± 1.7	19.1	8.6
Cut: Backgrounds		$Z \to \ell\ell$+jets				
	Events	jet $\to \tau_{had}$ (%)	$e \to \tau_{had}$ (%)			
pre-selection	1796 ± 29	30.9	69.0			
$\Delta\phi(\tau, \ell) > 2.4$	1377 ± 26	21.2	78.7			
$m_T(\ell, E_T^{miss})$	920 ± 21	17.7	82.3			
b-veto	907 ± 21	17.6	82.4			

- backgrounds with true hadronic tau and true light lepton, composed of $Z \to \tau_{lep}\tau_{had}$ events and top events such as $t\bar{t} \to W^+W^-b\bar{b} \to \tau_{had}\ell\nu\bar{\nu}b\bar{b}$;

- backgrounds with true light lepton and a light lepton faking the τ_{had}, which consist mostly of $Z \to \ell\ell$ events;

- backgrounds with true light lepton and jet misidentified as a hadronic tau, composed mainly by W+jets events where the W decays leptonically, as well as a smaller contribution of Z/γ^*+jets events;

- backgrounds where both the light lepton and tau are misidentified, dominated by multi-jet processes.

Table 5.2: Electron channel cutflow for signal samples. The predictions correspond to a luminosity of 3.2 fb^{-1} and a cross section of 1 pb^{-1}. The errors are due solely to the finite number of simulated events.

Cut: Signal $e\tau_{had}$		ggH200	ggH300	ggH400	ggH500
pre-selection		52.8 ± 1.4	105.0 ± 2.0	144.5 ± 2.4	166.8 ± 2.6
$\Delta\phi(\tau, \ell) > 2.4$		45.4 ± 1.3	96.2 ± 1.9	137.7 ± 2.4	160.1 ± 2.5
$m_T(\ell, E_T^{miss})$		31.2 ± 1.1	60.5 ± 1.5	89.8 ± 1.9	103.2 ± 2.0
b-veto		30.7 ± 1.1	58.9 ± 1.5	87.0 ± 1.9	99.8 ± 2.0
Cut: Signal $e\tau_{had}$	ggH600	ggH700	ggH800	ggH1000	ggH1200
pre-selection	181.0 ± 3.0	182.5 ± 3.0	187.9 ± 3.0	177.5 ± 2.9	167.9 ± 2.8
$\Delta\phi(\tau, \ell) > 2.4$	173.8 ± 2.9	176.9 ± 2.9	182.3 ± 3.0	172.1 ± 2.9	163.7 ± 2.8
$m_T(\ell, E_T^{miss})$	108.8 ± 2.3	112.2 ± 2.3	113.9 ± 2.4	101.7 ± 2.2	95.3 ± 2.1
b-veto	105.2 ± 2.3	108.5 ± 2.3	109.0 ± 2.3	97.4 ± 2.1	90.7 ± 2.1
Cut: Signal $e\tau_{had}$		bbH200	bbH300	bbH400	bbH500
pre-selection		53.0 ± 1.6	106.0 ± 2.3	139.2 ± 2.3	157.3 ± 2.8
$\Delta\phi(\tau, \ell) > 2.4$		48.0 ± 1.5	99.2 ± 2.2	131.5 ± 2.2	149.4 ± 2.7
$m_T(\ell, E_T^{miss})$		33.1 ± 1.2	65.7 ± 1.8	81.9 ± 1.8	92.2 ± 2.1
b-veto		25.5 ± 1.1	46.0 ± 1.5	53.6 ± 1.4	61.4 ± 1.7
Cut: Signal $e\tau_{had}$	bbH600	bbH700	bbH800	bbH1000	bbH1200
pre-selection	169.6 ± 3.5	170.3 ± 3.3	168.8 ± 3.2	164.6 ± 2.8	151.7 ± 3.0
$\Delta\phi(\tau, \ell) > 2.4$	163.0 ± 3.4	164.1 ± 3.2	163.1 ± 3.2	159.4 ± 2.7	148.1 ± 3.0
$m_T(\ell, E_T^{miss})$	102.4 ± 2.7	100.2 ± 2.5	97.2 ± 2.4	89.6 ± 2.0	81.9 ± 2.2
b-veto	65.1 ± 2.1	59.9 ± 2.0	57.4 ± 1.9	53.5 ± 1.6	48.0 ± 1.7

This section will describe the background estimation in each of the categories above.

5.4.1 Background with true hadronic tau and true light lepton

Monte Carlo simulated events are used whenever the reconstructed lepton and hadronic tau are truth-matched to true-level leptons in the simulated event. As in the $A \rightarrow Zh$ search, this includes events with a reconstructed τ_{had} truth-matched to a light lepton. Data-driven calibration and scale factors are used to account for differences between simulated objects and those found in data. Examples of these are the Tau Energy Scale (TES), which brings the simulated reconstructed tau energy closer to the actual detector response for hadronic

Table 5.3: Muon channel cutflow. The predictions correspond to a luminosity of 3.2 fb^{-1}. The errors are due solely to the finite number of simulated events.

Cut: Backgrounds		Top			$Z \to \tau\tau$+jets	
	Events	jet $\to \tau_{had}$ (%)	$e \to \tau_{had}$ (%)	Events	jet $\to \tau_{had}$ (%)	$e \to \tau_{had}$ (%)
pre-selection	3914.7 ± 11.7	28.6	2.6	8599.8 ± 58.5	0.9	0.0
$\Delta\phi(\tau, \ell) > 2.4$	1559.5 ± 7.4	24.2	2.4	6859.5 ± 52.1	0.7	0.0
$m_T(\ell, E_T^{miss})$	258.9 ± 3.0	34.4	3.0	5145.7 ± 45.2	0.8	0.0
b-veto	61.3 ± 1.4	39.3	2.6	5072.5 ± 44.7	0.7	0.0

Cut: Backgrounds		W+jets			Diboson	
	Events	jet $\to \tau_{had}$ (%)	$e \to \tau_{had}$ (%)	Events	jet $\to \tau_{had}$ (%)	$e \to \tau_{had}$ (%)
pre-selection	17590 ± 190	99.6	0.0	615.9 ± 5.7	24.1	3.6
$\Delta\phi(\tau, \ell) > 2.4$	9937 ± 140	99.5	0.0	314.0 ± 3.9	19.7	3.8
$m_T(\ell, E_T^{miss})$	1538 ± 55	99.5	0.0	61.9 ± 1.8	18.0	7.0
b-veto	1504 ± 54	99.5	0.0	60.1 ± 1.8	17.5	7.0

Cut: Backgrounds		$Z \to \ell\ell$+jets	
	Events	jet $\to \tau_{had}$ (%)	$e \to \tau_{had}$ (%)
pre-selection	2465 ± 32	19.6	80.4
$\Delta\phi(\tau, \ell) > 2.4$	2050 ± 29	13.6	86.3
$m_T(\ell, E_T^{miss})$	931 ± 19	8.7	91.3
b-veto	920 ± 19	8.8	91.2

taus, and the TauID scale factor that corrects for efficiency differences of the TauID quality requirement when applied to MC and data.

5.4.2 *Background with true light lepton and light lepton faking hadronic tau*

Events with electrons being misidentified as taus come mostly from $Z/\gamma^* \to ee$ and are known to have their MC predicted yields different from what is observed in data. This is particularly the case for the forward region ($|\eta| > 2.3$), as can be seen in Figure 5.3(b). For these reasons we implement a Z-mass veto in the $e\tau_{had}$ channel and veto high-η taus ($|\eta| < 2.3$) in both channels. The vetoed region corresponds to $80 < m_{\ell,\tau}^{vis} < 110$ GeV, and we observe a 10-fold reduction in this background from this cut.

To correct for the mismodelling of the remaining background in this category, a scale

Table 5.4: Muon channel cutflow for signal samples. The predictions correspond to a luminosity of 3.2 fb^{-1} and a cross section of 1 pb^{-1}. The errors are due solely to the finite number of simulated events.

Cut: Signal $\mu\tau_{had}$		ggH200	ggH300	ggH400	ggH500
pre-selection		68.5 ± 1.6	112.3 ± 2.0	135.9 ± 2.2	158.7 ± 2.4
$\Delta\phi(\tau, \ell) > 2.4$		59.6 ± 1.5	102.4 ± 1.9	129.0 ± 2.2	152.0 ± 2.4
$m_T(\ell, E_T^{miss})$		39.9 ± 1.2	64.7 ± 1.5	83.0 ± 1.8	96.1 ± 1.9
b-veto		39.2 ± 1.2	62.9 ± 1.5	80.7 ± 1.7	93.0 ± 1.8
Cut: Signal $\mu\tau_{had}$)	ggH600	ggH700	ggH800	ggH1000	ggH1200
pre-selection	169.0 ± 2.8	178.3 ± 2.8	184.0 ± 2.9	179.2 ± 2.8	178.4 ± 2.8
$\Delta\phi(\tau, \ell) > 2.4$	163.0 ± 2.7	172.7 ± 2.8	178.5 ± 2.8	172.7 ± 2.8	173.4 ± 2.8
$m_T(\ell, E_T^{miss})$	101.9 ± 2.2	107.0 ± 2.2	110.5 ± 2.2	105.3 ± 2.2	101.0 ± 2.1
b-veto	98.3 ± 2.1	102.5 ± 2.1	105.9 ± 2.2	100.6 ± 2.1	96.0 ± 2.0
Cut: Signal $\mu\tau_{had}$		bbH200	bbH300	bbH400	bbH500
pre-selection		65.4 ± 1.7	109.7 ± 2.2	132.6 ± 2.1	146.0 ± 2.6
$\Delta\phi(\tau, \ell) > 2.4$		58.9 ± 1.6	101.2 ± 2.1	124.6 ± 2.1	137.7 ± 2.5
$m_T(\ell, E_T^{miss})$		39.1 ± 1.3	65.4 ± 1.7	79.0 ± 1.6	82.5 ± 2.0
b-veto		28.7 ± 1.1	45.6 ± 1.4	51.1 ± 1.3	53.0 ± 1.6
Cut: Signal $\mu\tau_{had}$	bbH600	bbH700	bbH800	bbH1000	bbH1200
pre-selection	159.9 ± 3.2	170.4 ± 3.0	172.9 ± 3.0	171.7 ± 2.6	166.6 ± 3.0
$\Delta\phi(\tau, \ell) > 2.4$	152.1 ± 3.1	163.5 ± 3.0	166.2 ± 3.0	166.0 ± 2.6	162.3 ± 2.9
$m_T(\ell, E_T^{miss})$	93.8 ± 2.4	99.6 ± 2.3	97.8 ± 2.3	96.3 ± 1.9	89.9 ± 2.1
b-veto	57.9 ± 1.9	62.2 ± 1.8	58.7 ± 1.8	57.4 ± 1.5	55.2 ± 1.6

factor from the Z-mass control region is derived as a function of the leading τ_{had} pseudorapidity. This control region is defined by inverting the Z-mass cut, with the remainder of the signal region selection kept the same. Events in this control region with misidentified leptons and/or taus are estimated using the "combined fake-factor method" that is described in Section 5.4.5, while backgrounds with true leptons and taus are taken from simulation with both statistical and systematic uncertainties taken into consideration. The final 1-prong and 3-prong scale factors are shown in Figure 5.4. For 1-prong events, a conservative 20% uncertainty is used that represents the fraction of subtracted simulated events in the Z-mass control region. For 3-prong, no evidence of η-dependence is observed so a universal

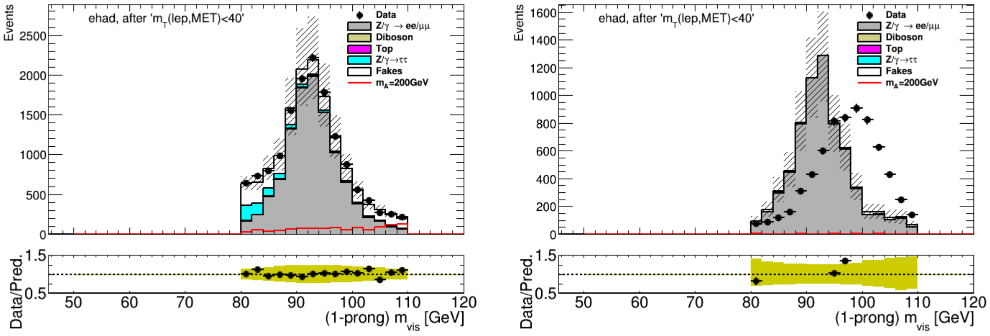

(a) (b)

Figure 5.3: Visible mass distributions in the $e\tau_{had}$ channel for events with $\eta < 2$ (a) and $|\eta| > 2.3$ (b), after applying the η_τ-dependent scale factor .

1.15 ± 0.50 scale factor is used.

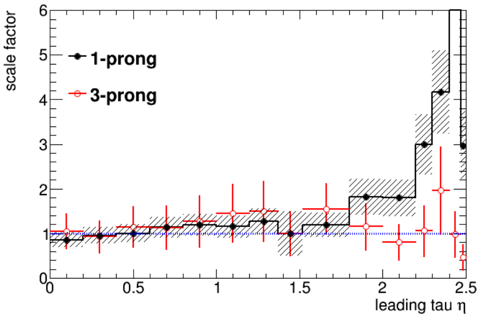

Figure 5.4: Scale factors for misidentified e-to-τ_{had} events.

We can test the scale factors above by comparing distributions for variables other than the tau pseudorapidity in the Z-mass control region, and confirming that the prediction matches the observed data. Distributions of $m_T(\ell, \tau_{had})$ and m_T^{tot} for 1-prong and 3-prong are shown in Figures 5.5 and 5.6, and indicate the scale factors are successful in correcting the $e \to \tau_{had}$ fake rate in MC events.

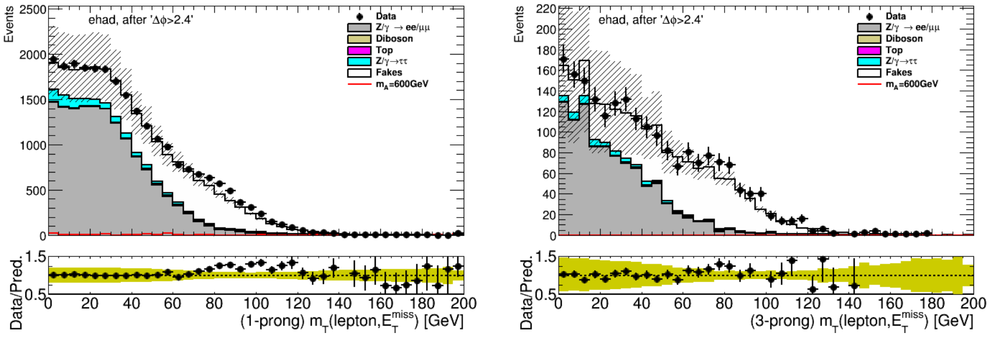

(a) (b)

Figure 5.5: Distributions of $m_T(\ell, \tau_{had})$ for events with one-prong (a) and three-prong (b) τ_{had} before the $m_T(\ell, E_T^{miss})$ cut requirement.

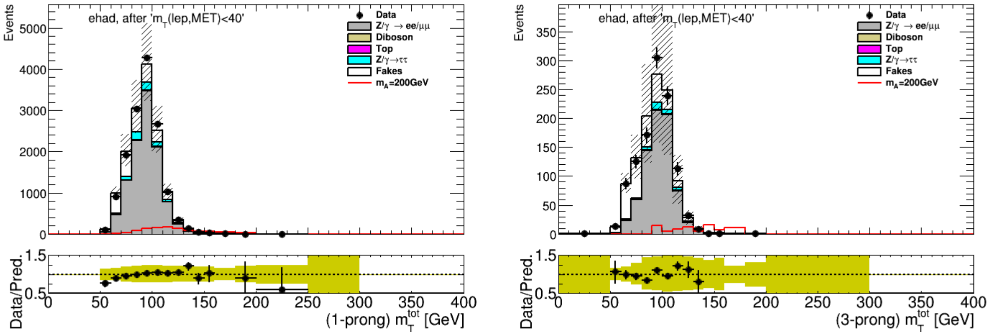

(a) (b)

Figure 5.6: Distributions of the total transverse mass for events with one-prong (a) and three-prong (b) τ_{had}.

5.4.3 Background with true light lepton and jet misidentified as tau

This background category is dominated by W+jets events where the W decays leptonically and the jet is misidentified as a τ_{had}. Because the jet-to-τ_{had} fake rate is not well simulated in MC, a data-driven fake factor method is used.

The fake factor method consists of predicting the number of events with misidentified objects passing our selection by applying multiplicative factors to events that were successfully rejected by the tau identification criterion but otherwise pass the full signal region selection. Fake factors are defined as the ratio of the number objects passing a given selection cut divided by the number failing the same cut in a control region that is almost exclusively populated by the objects whose misidentification rate we want to quantify. They are usually parameterized as a function of one or more kinematic variables that affect the efficiency of the selection cut used.

To compute W+jets fake factors, a W+jets control region is used where the $m_T(\ell, E_T^{miss}) <$ 40 GeV cut is replaced by a high $m_T(\ell, E_T^{miss})$ requirement. In this control region, fake factors are computed using the ratio of events passing medium TauID divided by events failing medium TauID. They are computed as a function of the hadronic tau transverse momentum and number of tracks:

$$FF(W + jets) = \frac{N(\text{pass medium tau ID})}{N(\text{fail medium TauID and BDT} > 0.35)} \tag{5.3}$$

The full selection used to define the W+jets control region is:

- exactly one light lepton passing the same identification criteria as the signal region;
- events must pass the same dilepton veto used in the signal region;
- at least one τ_{had} candidate. For events failing the τ_{had} identification requirement, a τ_{had}-ID BDT score greater than 0.35 on the τ_{had} ID is required;
- $\Delta\phi(\tau, \ell) > 2.4$;

- $m_T(\ell, E_T^{miss}) > 60$ GeV for the $\mu\tau_{had}$ channel;
- $m_T(\ell, E_T^{miss}) > 70$ GeV for the $e\tau_{had}$ channel;
- events with b-tagged jets are vetoed, as in the signal region.

The cut on the TauID BDT score causes the fractions of gluon-initiated and quark-initiated jets to match that in the signal region more closely. The cut on the transverse mass is tighter in the $e\tau_{had}$ channel to reject multi-jet background contamination and increase W+jets purity. Since the fake factors are to be used for backgrounds with jets faking τ_{had}, events with correctly identified τ_{had} or light leptons faking the τ_{had} are subtracted from the W+jets control region.

The distributions of several physically interesting variables is shown in Figures 5.7-5.10. The excess in data events observed at low $m_T(\ell, E_T^{miss})$ is mostly due to multi-jet contamination. The distributions show disagreements both in normalization and shape between data and simulation, which is why a data-driven fake factor method is necessary.

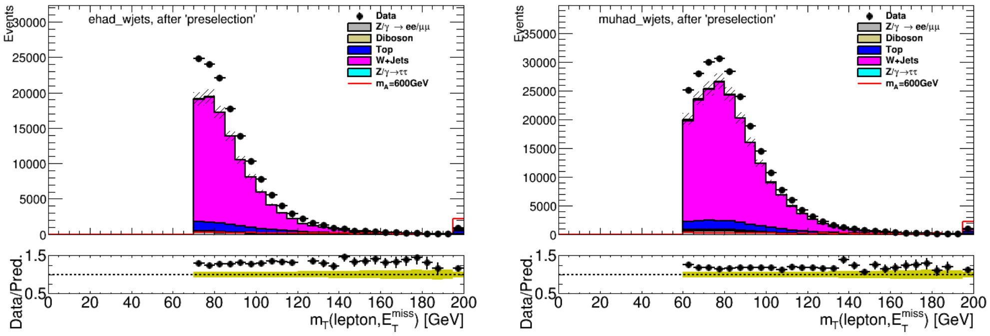

(a)

(b)

Figure 5.7: Distribution of $M_T(\ell, E_T^{miss})$ in the W+jets control region after preselection in the $e\tau_{had}$ (a) and $\mu\tau_{had}$ (b) channels. Only MC samples are shown for the prediction and no multi-jet estimation is included. The plotted signal is $m_\phi = 600$ GeV, where $\phi = H/A$, produced via gluon-fusion with a cross section times branching ratio of 100 pb (far beyond the excluded region of the MSSM, which is below 0.1 pb).

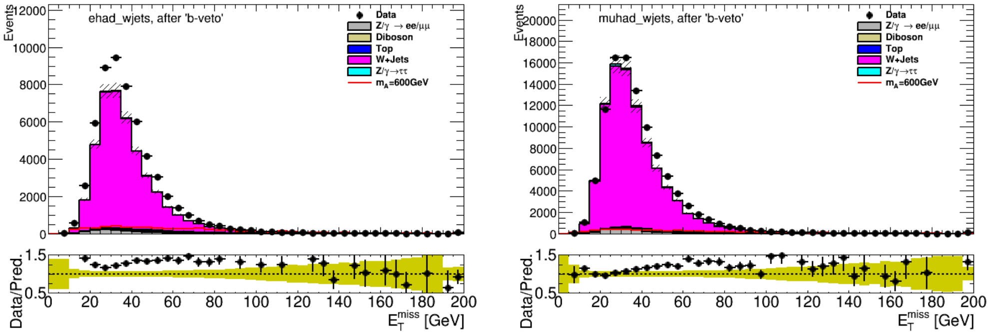

(a) (b)

Figure 5.8: Distribution of E_T^{miss} after the full W+jets control region selection in the $e\tau_{had}$ (a) and $\mu\tau_{had}$ (b) channels. Only MC samples are shown for the prediction and no multi-jet estimation is included. The plotted signal is described in Figure 5.7.

The final W+jets fake factors are shown in Figure 5.11, compared to "fake factors" computed in the low-m_T signal region. We do not expect very good agreement between the fake factors of the opposing $m_T(\ell, E_T^{miss})$ regions due to the higher fraction of multi-jet background at lower transverse mass. However, we see they are nevertheless in reasonable agreement given the high uncertainty in their calculation (described below). The fake factors used in the background prediction are the combined $e\tau_{had} + \mu\tau_{had}$ set, but calculated and applied separately for 1-track and 3-track hadronic taus.

The fake rate is also dependent on the E_T^{miss} distribution in the event such that there is a poor modelling of $\Delta\phi(\tau_{had}, E_T^{miss})$ and $\Delta\phi(\ell, E_T^{miss})$, as can be seen in Figure 5.12. Thus, an extra correction is derived using $\Delta\phi(\tau_{had}, E_T^{miss})$-dependent scale factors (shown in Figure 5.13). These are calculated and applied separately for the $e\tau_{had}$ and $\mu\tau_{had}$ channels. Because the 1-track and 3-track scale factors show some variation in the $e\tau_{had}$ channel, the correction in that channel uses separate 1-track and 3-track scale factors. An uncertainty of 10% is added to these scale factors due to the subtraction of MC events with true objects. Finally, Figure 5.14 shows that the corrected fake factors are performing well by confirming that the total transverse mass distribution observed in data agrees with that from the fake factor

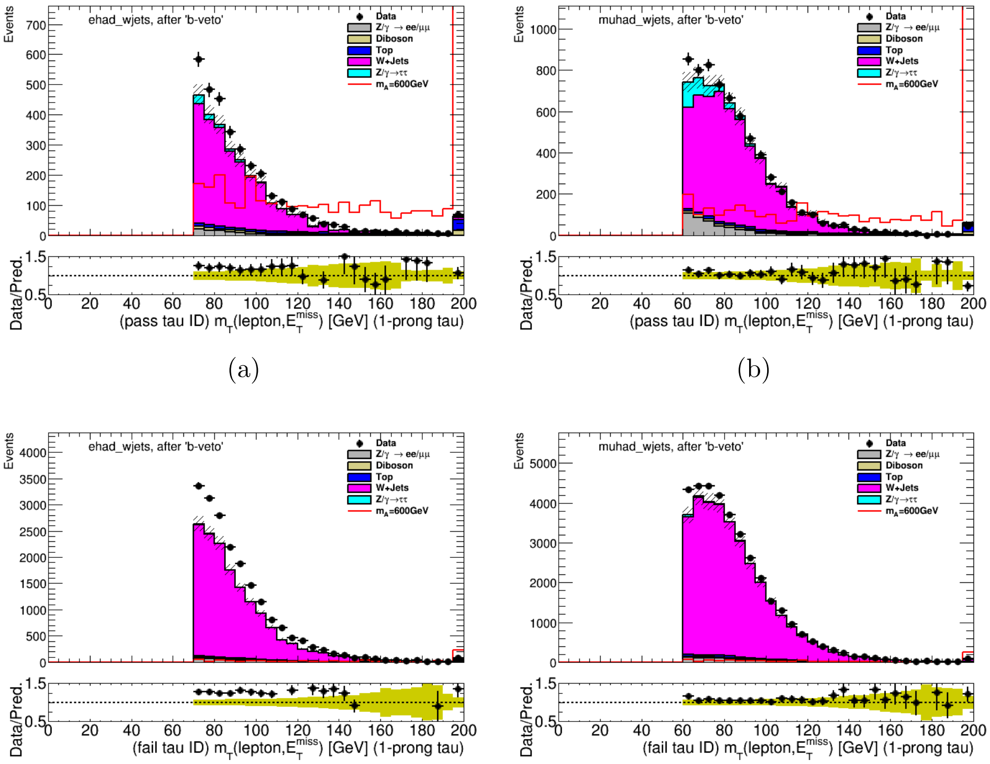

(a) (b)

(c) (d)

Figure 5.9: Distributions of $m_T(\ell, E_T^{miss})$ for events passing (a,b) and failing (c,d) the τ_{had} identification requirement in the W+jets control region and 1-prong τ_{had}. No multi-jet estimation is included. The plotted signal is described in Figure 5.7.

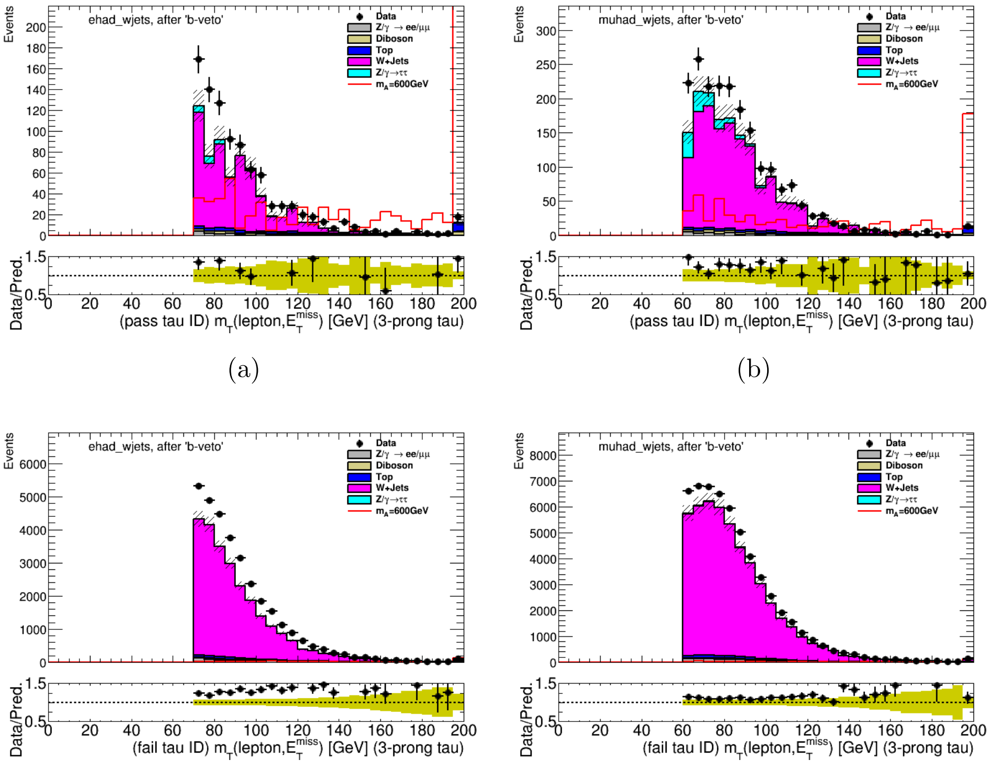

(a) (b)

(c) (d)

Figure 5.10: Distributions of $m_T(\ell, E_T^{miss})$ for events passing (a,b) and failing (c,d) the τ_{had} identification requirement in the W+jets control region and 3-prong τ_{had}. No multi-jet estimation is included. The plotted signal is described in Figure 5.7.

prediction in the W+jets control region.

Systematic uncertainties in the W+jets fake factors

The error bars shown in Figure 5.11 contain both systematic and statistical uncertainties. There are several sources of systematic errors in the W+jets background prediction:

- the kinematic differences between high transverse mass W+jets events ($m_T(\ell, E_T^{miss}) > 60$ GeV) and signal region events ($m_T(\ell, E_T^{miss}) < 40$ GeV) can lead to incorrect assumptions about the W+jets misidentification rates in signal region;

- contamination in the W+jets control region from other backgrounds with different τ_{had} identification efficiencies will impact the fake factor calculation;

- events failing τ_{had} identification have a different jet composition than events passing τ_{had} identification.

The impact of these potential sources of error have been investigated. The three error sources above can be correlated. For example, the $m_T(\ell, E_T^{miss})$ cut directly affects the amount of background contamination. Therefore, effects that are small or overshadowed by statistical uncertainties are not propagated to the final uncertainty. Regardless, the high-to-low $m_T(\ell, E_T^{miss})$ systematic uncertainty completely dominates the W+jets fake factor systematic uncertainty, so that the choice of which other errors to include has little impact on the final systematic.

The three sources of systematic uncertainty in the calculation of the W+jets fake factors are discussed in more detail in the following.

1. Fake rate differences between high and low m_T regions

To be able to distinguish this error source from others such as multi-jet contamination, this systematic is calculated using simulated W+jets MC events. Fake factors computed using Equation 5.3 in the W+jets control region are compared to those in the low-$m_T(\ell, E_T^{miss})$

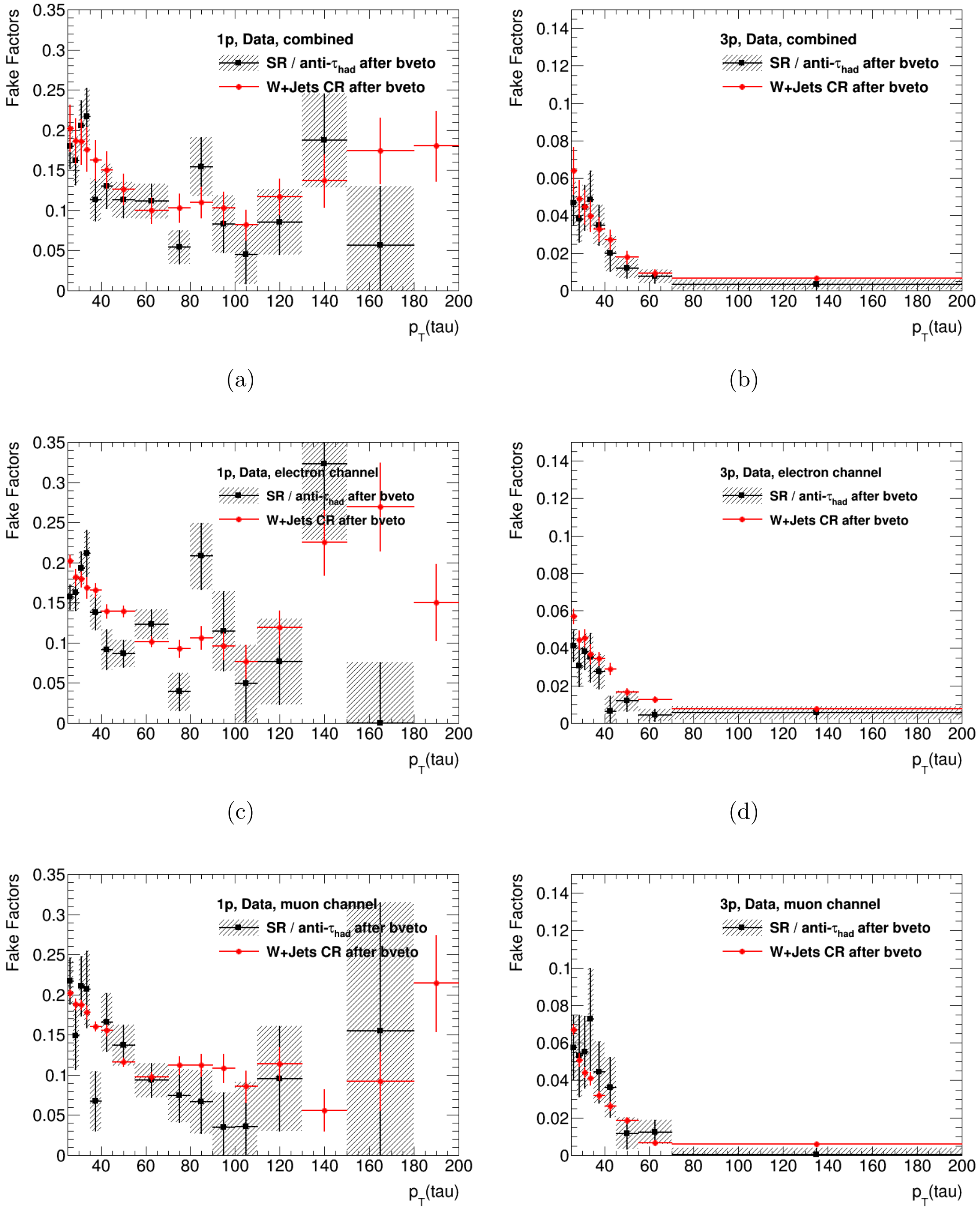

(a) (b)

(c) (d)

(e) (f)

Figure 5.11: Fake factors from the W+jets control region as a function of $p_T(\tau_{had})$ calculated in data for 1-prong (a) and 3-prong (b) τ_{had} candidates shown with red circular markers. The ratio of the signal region over the anti-τ_{had} region after subtracting the true backgrounds from simulations is shown for comparison with black markers. In (c,d) and (e,f), the fake factors are shown separately for the electron and the muon channel, respectively.

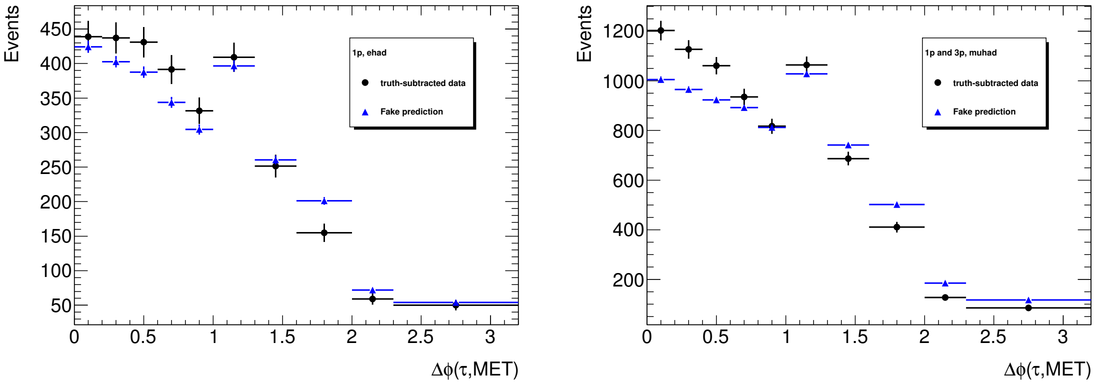

(a)

(b)

Figure 5.12: Distributions in the W+jets control region of $\Delta\phi(\tau, E_T^{miss})$ for truth-subtracted data passing τ identification and the prediction of τ fakes from the anti-τ region.

region. Because of the limited number of simulated W+jets events, the comparison can be done in only three p_T regions. The relative differences between the two sets of fake factors are shown in Table 5.5. For both prongs, a 20% systematic error is assigned from this effect which is the largest source of systematic error in the W+jets fake factor estimation.

Table 5.5: Relative difference betwee W+jets fake factors computed in the high and low $m_T(\ell, E_T^{miss})$ regions for 1-prong and 3-prong separately.

p_T bin [GeV]	1-prong	3-prong
$25 - 30$	$30\% \pm 5\%$	$15\% \pm 9\%$
$30 - 45$	$16\% \pm 5\%$	$30\% \pm 9\%$
$45 - 200$	$21\% \pm 5\%$	$23\% \pm 12\%$

2. Impurity of the W+jets control region

The W+jets control region has some contamination from processes with true leptons and hadronic taus, and from events with electrons faking the τ_{had}. These are subtracted from the W+jets control region according to their simulated predictions in that region. Thus,

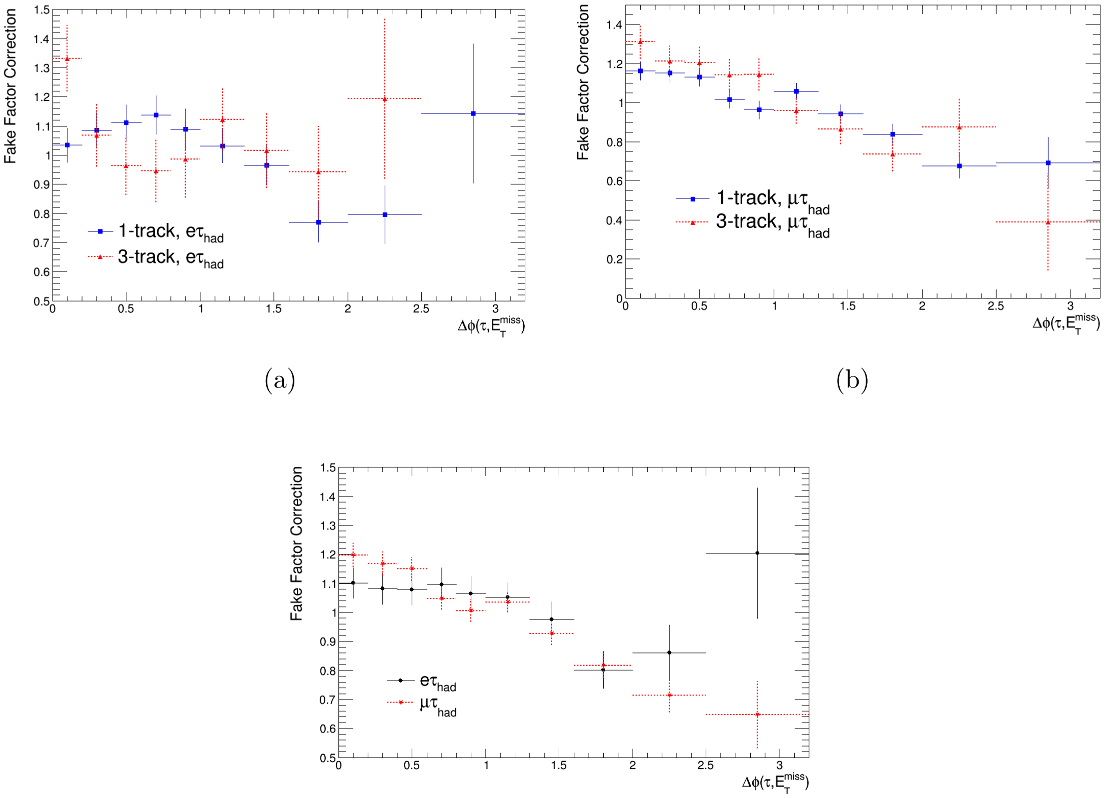

(a)

(b)

(c)

Figure 5.13: Correction scale factors to the W+jets fake factors as a function of $\Delta\phi(\tau, E_T^{miss})$. The scale factors are shown for the $e\tau_{had}$ (a), $\mu\tau_{had}$ (b) channels and combined (c) channels.
,

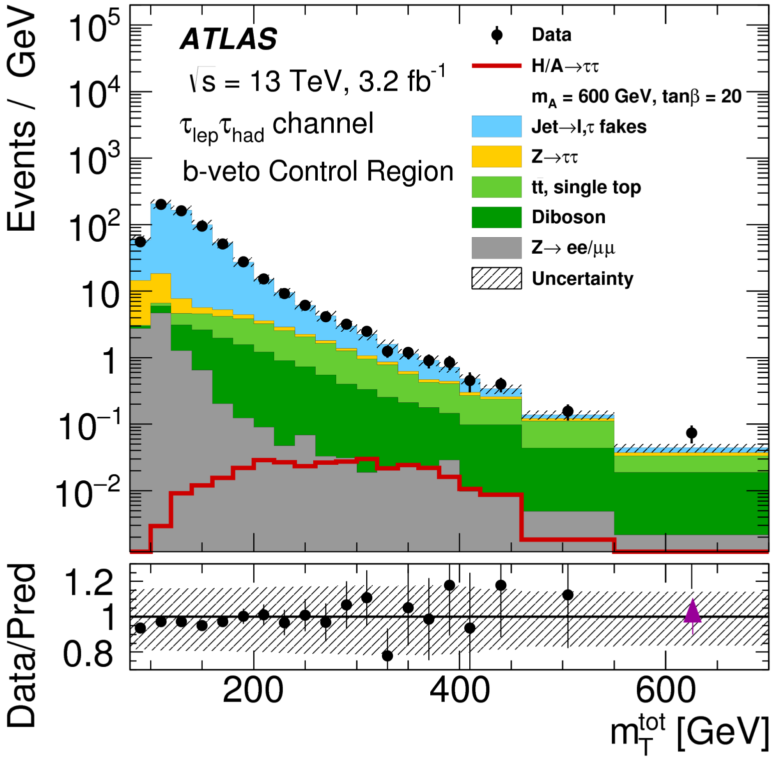

Figure 5.14: Distribution of the total transverse mass in the high $m_T(\ell, E_T^{miss})$ region for the combined $e\tau_{had} + \mu\tau_{had}$ channels.

a 10% uncertainty in the subtraction of simulated events compatible with the systematic uncertainty associated with using such simulated events (as shown in section 5.5) is added to the MC subtraction.

The effect of multi-jet contamination is more difficult to estimate. As will be explained in Section 5.4.4, we cannot use simulated events to model multi-jet processes. This contamination is then estimated from the excess of data compared to the combined MC prediction in the W+jets control region, found to be at most 10% for the fail-TauID region of the $e\tau_{had}$ channel. We then calculate what the impact on the fake factor would be if the entire W+jets control region had a 10% multi-jet contamination. By scaling the impact of the observed differences between the W+jets and multi-jet fake factors (shown below) with this impurity fraction, a systematic uncertainty of approximately 3% (1%) is found for 1-prong (3-prong) events.

Table 5.6: W+jets b-veto control region composition for 1-prong τ_{had}.

channel	$e\tau_{had}$				$\mu\tau_{had}$			
tau ID	pass		fail		pass		fail	
	inclusive	true τ_{had}	inclusive	true τ_{had}	inclusive	true τ_{had}	inclusive	true τ_{had}
$Z \to \tau\tau$	99 ± 5	94 ± 5	40 ± 3	31 ± 2	384 ± 15	379 ± 16	150 ± 7	121 ± 6
$Z \to \ell\ell$	90 ± 5	34 ± 3	416 ± 16	24 ± 2	449 ± 19	166 ± 8	868 ± 28	42 ± 3
Diboson	113 ± 4	97 ± 4	150 ± 5	28 ± 1	149 ± 5	120 ± 4	244 ± 8	34 ± 1
Top	166 ± 6	134 ± 5	40 ± 1	6 ± 0	210 ± 7	156 ± 5	67 ± 2	8 ± 0
W+jets	2262 ± 80	17 ± 3	14338 ± 436	7 ± 2	4979 ± 168	32 ± 5	31395 ± 941	27 ± 5
Data	3312		19579		6535		35741	

3. Anti-τ_{had} jet composition

Events passing the “medium” criteria of the TauID have a minimum BDT score that varies in τ_{had} p_T, and is on the order of 0.7 for 1-prong and 0.8 for 3-prong. Events failing τ_{had}-ID can have BDT scores as low as 0, and events with very low BDT score have a higher fraction of gluon-initiated jets faking the τ_{had}. Because gluon-initiated jets have a different fake rate compared to quark-initiated jets, a minimum BDT score of 0.35 is chosen so that the jet composition in the anti-τ_{had} region more closely resembles the one found in the signal region.

Table 5.7: W+jets b-veto control region composition for 3-prong τ_{had}.

channel	$e\tau_{had}$				$\mu\tau_{had}$			
tau ID	pass		fail		pass		fail	
	inclusive	true τ_{had}	inclusive	true τ_{had}	inclusive	true τ_{had}	inclusive	true τ_{had}
$Z \rightarrow \tau\tau$	27 ± 2	27 ± 2	27 ± 2	16 ± 1	122 ± 6	121 ± 6	123 ± 6	78 ± 4
$Z \rightarrow \ell\ell$	12 ± 2	2 ± 1	640 ± 24	21 ± 2	28 ± 2	1 ± 0	1066 ± 33	8 ± 1
Diboson	31 ± 1	26 ± 1	240 ± 10	19 ± 5	43 ± 2	33 ± 1	399 ± 13	32 ± 1
Top	45 ± 2	37 ± 2	12 ± 0	1 ± 0	58 ± 2	43 ± 2	23 ± 1	1 ± 0
W+jets	542 ± 26	3 ± 1	23501 ± 734	35 ± 5	1357 ± 57	8 ± 2	47336 ± 1368	56 ± 7
Data	937		32192		1997		55798	

An estimate of how much impact the jet composition can have in the W+jets fake factors is obtained by varying the lower BDT score cut. Changing the cut to 0.45 and recomputing the data-driven W+jets prediction indicates that this systematic error is approximately 5% for the $e\tau_{had}$ channel and 1% for the $\mu\tau_{had}$ channel.

5.4.4 Background with misidentified lepton and tau

The majority of events with misidentified lepton and tau are from multi-jet background. The good light lepton identification in ATLAS ensures a low jet-to-ℓ fake rate, causing the acceptance efficiency of multi-jet events in our signal region is very low. However, because the LHC is a proton-proton collider, the production rate of multi-jet events is extremely high, which causes multi-jet processes to still have an important contribution to the background in our signal region. It is not computationally feasible to generate enough MC events to reproduce these two opposing effects, so a data-driven estimation of multi-jet is required. Furthermore, the jet-to-τ_{had} fake rate and the shower properties of τ_{had} fakes are not always modelled well. For these reasons, a data-driven estimate of the multi-jet background is necessary.

The estimation method chosen for multi-jet background is similar to that for W+jets, using $p_T(\tau_{had})$ and prong-dependent fake factors calculated in a multi-jet control region using the TauID identification ratio (as shown in Equation 5.3). The multi-jet control region is obtained by inverting the isolation requirement of the light lepton, i.e. by defining an anti-isolated control region. The main sources of systematic uncertainties are:

- the uncertainties on the MC subtraction of events with true objects. This is conservatively estimated by varying the number of subtracted events by 50% and checking the impact on the fake factors. Due to the very low presence of events with true leptons in the anti-isolated control region, this systematic is negligible;

- biases in the τ_{had} ID efficiency from the anti-isolation requirement. This is estimated by comparing the fake factors in the multi-jet control region with those in the isolated region. To ensure orthogonality with the signal region, the lepton and τ_{had} are required to have same signed charge. The differences between the two sets of fake factors is used as a systematic uncertainty;

- unaccounted for dependence of the fake factors on E_T^{miss}. Similarly to the W+jets fake factors, a disagreement between predicted and observed events is observed for the $\Delta\phi(\ell, E_T^{miss})$ distribution, as can be seen in Figure 5.15. Thus, $\Delta\phi(\ell, E_T^{miss})$-dependent correction scale factors are used and a constant 10% uncertainty is applied to the multi-jet scale factors (again due to the subtraction of simulated events).

The final multi-jet fake factors are shown in Figure 5.16.

5.4.5 Combined Fake-Factor Method

The W+jets and multi-jet fake factors are defined as the pass/fail identification ratio of the medium TauID working point. Therefore, they must be multiplied with events that pass all selection requirements apart from the medium TauID cut. The category made up of such events will be referred to as the anti-τ_{had} region. Because the W+jets and QCD fake factors are to be applied to data events in the anti-τ_{had} region, for which truth-level information is obviously unavailable, an immediate concern is how to separate which events correspond to

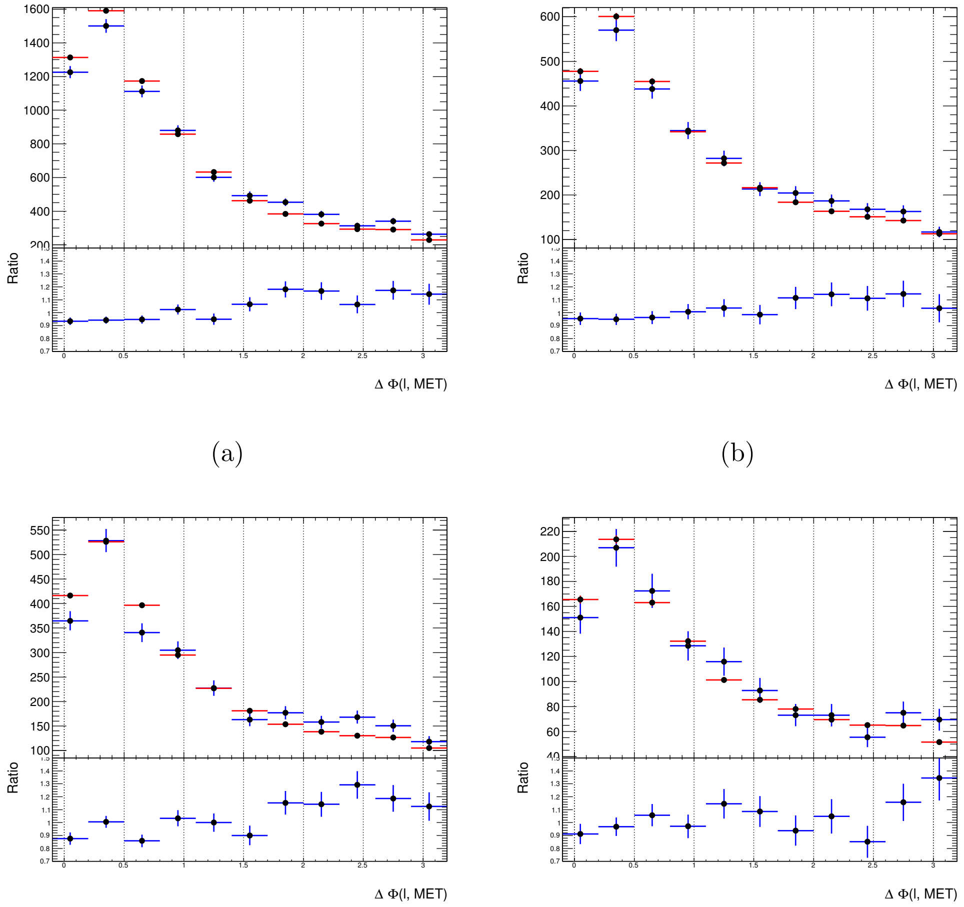

(a)

(b)

(c)

(d)

Figure 5.15: $\Delta\Phi(l, MET)$ distribution in $e\tau_{had}$ 1-prong (a), $\mu\tau_{had}$ 1-prong (b), $e\tau_{had}$ 3-prong (c) and $\mu\tau_{had}$ 3-prong (d). The blue points represent the events passing TauID selection in the anti-isolation region. The red points represent for events that failed TauID weighted with the lepton fake factors.

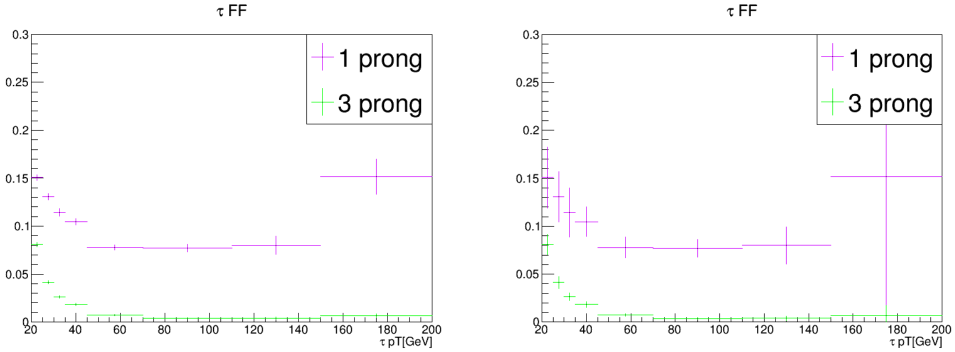

(a)

(b)

Figure 5.16: Fake factors for jets from multi-jet events misidentified as τ_{had}. Fake factors are shown as a function of p_T, for 1-prong and 3-prong τ, with (left) statistical uncertainty only and (right) all statistical and systematic uncertainties with the exception of the uncertainty on the anti-τ_{had} definition (evaluated by varying the jet BDT cut).

W+jets background and which correspond to multi-jet. Since the anti-τ_{had} region has a large number of events, a nearly perfect approximation is to combine the fake factors according to the relative fraction of each background into a "combined fake factor", instead of separating the to-be-weighed events by their processes. The new combined fake factor is defined below:

$$FF(\text{comb}) = FF(W+\text{jets}) \times (1 - r_{\text{QCD}}) + FF(\text{QCD}) \times r_{\text{QCD}}, \tag{5.4}$$

where r_{QCD} is the multi-jet fraction of data events in the anti-τ_{had} region after subtraction of events with true objects.

Predicting the multi-jet fraction

In terms of their object signatures, the main difference between multi-jet and W+jets is that in the former the light lepton is a misidentified jet whilst in the latter it is a true object from the W decay. To predict the jet-to-ℓ misidentification rate in the anti-τ_{had} region, a lepton fake factor method is defined using the lepton isolation efficiency, as shown below:

$$FF = \frac{N(\text{pass “gradient” lepton isolation})}{N(\text{fail “gradient” lepton isolation})} \tag{5.5}$$

These lepton fake factors are calculated in a “fake-lepton control region” defined with the following selection:

- same single lepton triggers as signal region;
- exactly one lepton. No isolation is required since this is the criteria to define the fake factors;
- at least one jet;
- no events with at least one τ_{had} passing “loose” identification;
- $M_T(\ell, E_T^{miss}) < 30$ GeV.

The event selection is designed to minimize the contamination of true leptons without dramatically reducing the number of multi-jet events. The cuts on the transverse mass and number of jets are efficient both in rejecting W+jets events and bringing the selection closer to the signal region selection. The number of jets per event and distributions of the transverse mass can be found in Figures 5.17-5.18. The sample composition of the lepton fake factor control region is shown in Table 5.8.

The lepton fake factors are parameterized as a function of lepton η, shown in Figure 5.19. For the $\mu\tau_{had}$ channel, there are two sets of fake factors used for events with lepton transverse momentum above or below 55 GeV. The multi-jet fraction in the anti-τ_{had} region is obtained by applying these fake factors to data events in the anti-isolated anti-τ_{had} region. The multi-jet fraction of the anti-τ_{had} region (r_{QCD} term of Equation 5.4) is then given by:

$$r_{\text{QCD}} = \frac{N_{\text{QCD}}}{N_{\text{data}} - N_{\text{true MC}}} \tag{5.6}$$

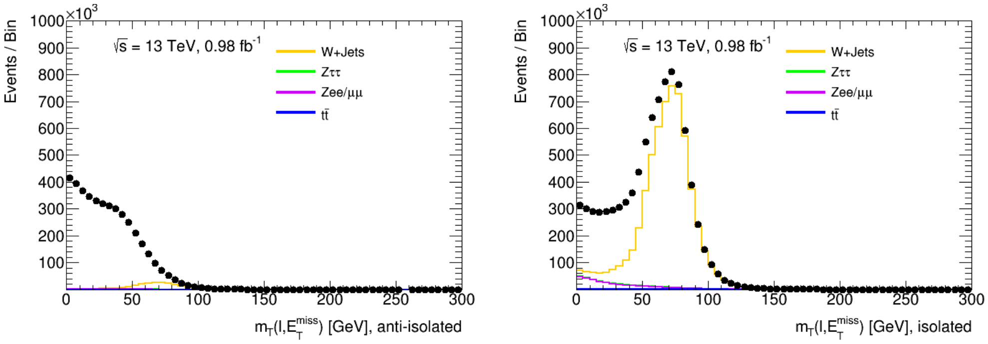

(a) (b)

Figure 5.17: The transverse mass of the lepton and missing transverse momentum in the fake lepton region for e and μ channels combined, (a) with the anti-isolation applied and (b) with the isolation requirement applied, but without the cuts on jet multiplicity and transverse mass applied.

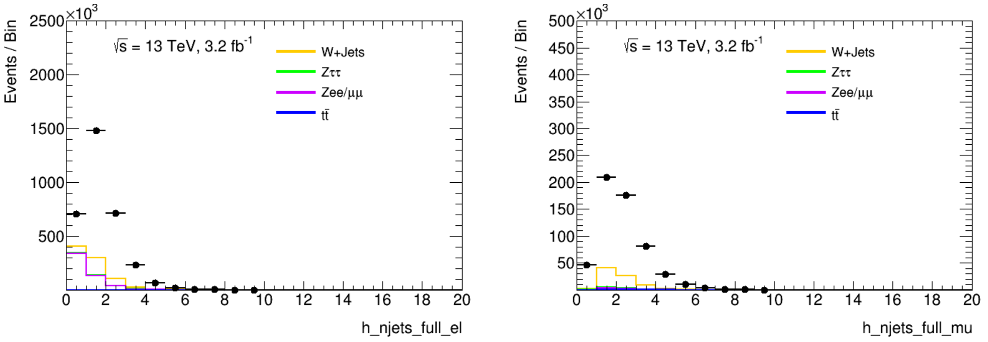

(a) (b)

Figure 5.18: The number of jets in the fake lepton region for the $e\tau_{had}$ (a) and $\mu\tau_{had}$ (b) channels with no requirement on the lepton isolation.

Table 5.8: Events in the fake lepton region. The numbers correspond to an integrated luminosity of 3.2 fb^{-1}. The quoted uncertainties are due to the finite number of generated events in the simulated samples.

Backgrounds	μ-channel b-veto	e-channel b-veto
W+jets	67700 ± 900	244500 ± 1700
$Z \to \tau\tau$+jets	4340 ± 110	10700 ± 180
Top	1366 ± 27	3020 ± 40
$Z \to \ell\ell$+jets	5130 ± 120	174700 ± 700
Total non-multi-jet background	78500 ± 900	433000 ± 1900
Data	507760	2511210
ggH, m_A = 350 GeV, 1pb	8.3 ± 0.6	15.9 ± 0.8
ggH, m_A = 1500 GeV, 1pb	5.9 ± 0.5	8.4 ± 0.6

where N_{QCD} is the number of multi-jet events estimated with the lepton fake factors, N_{data} the number of events observed in data, and $N_{\text{true MC}}$ the number of simulated events with truth-matched leptons and taus.

The r_{QCD} fraction is parameterized as a function of τ_{had} p_T, as shown in Figure 5.20. The uncertainties considered in the r_{QCD} parameterization include:

- statistical uncertainty on the lepton fake factor, corresponding to less than 1%;
- systematic uncertainty from true lepton contamination of the lepton fake factor control region, corresponding to approximately 9% and 12% in the $e\tau_{had}$ and $\mu\tau_{had}$ channels, respectively;
- statistical uncertainty in the anti-τ_{had} region, roughly 1%;
- systematic uncertainty from varying the transverse mass cut in the lepton fake factor control region definition, approximately 4% in the electron channel but only 0.7% in the muon channel.

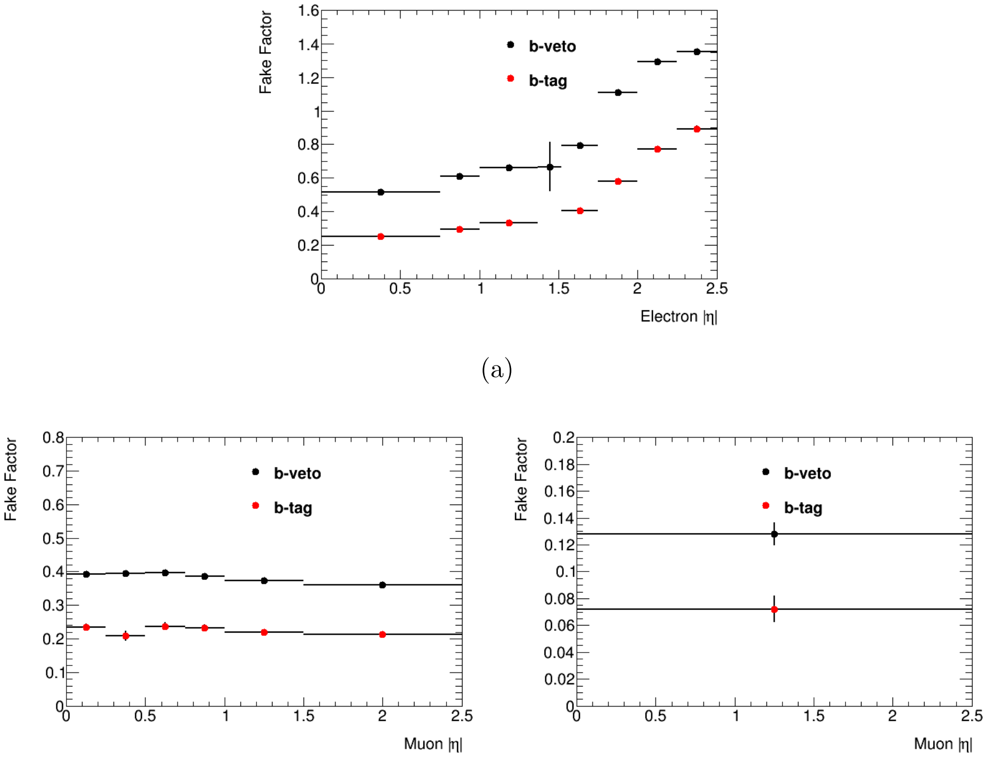

(a)

(b) (c)

Figure 5.19: Fake factors from the fake lepton control region as a function of lepton η for electrons (a), muons with $p_T < 55$ GeV (b) and muons with $p_T > 55$ GeV (c).

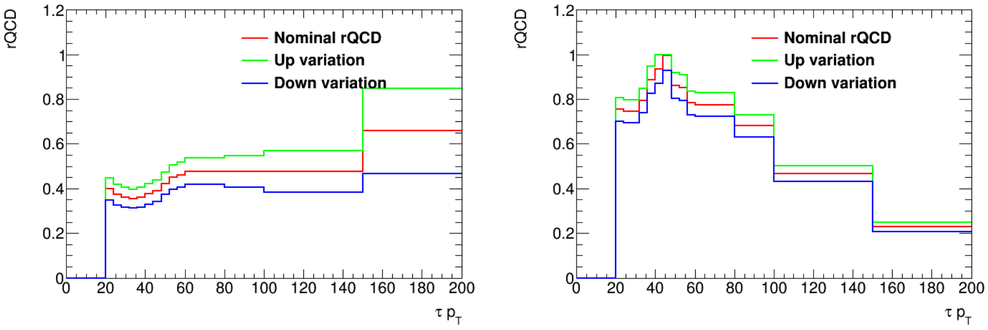

(a) (b)

Figure 5.20: The trend of r_{QCD} as a function of τp_T at the end of the event selection, along with the total up and down shifts for the uncertainties, shown separately for the muon (left) and electron (right) channels.

Using the multi-jet estimate (r_{QCD}) from the lepton fake factor method and the W+jets and multi-jet fake factors, the combined fake factor of Equation 5.4 can be calculated. The final prediction of the background with misidentified leptons and/or hadronic taus for several kinematic variables is shown in Figures 5.21-5.22. A last set of shape systematics is considered for the final misidentified background prediction where the W+jets fake factors, multi-jet fake factors and r_{QCD} are separately varied by one standard deviation of their respective uncertainties. Since the W+jets and multi-jet are not different between the $e\tau_{had}$ and $\mu\tau_{had}$ channels, they are treated as correlated between the channels. The r_{QCD} fraction, however, is treated as uncorrelated since it is separately derived for each lepton channel.

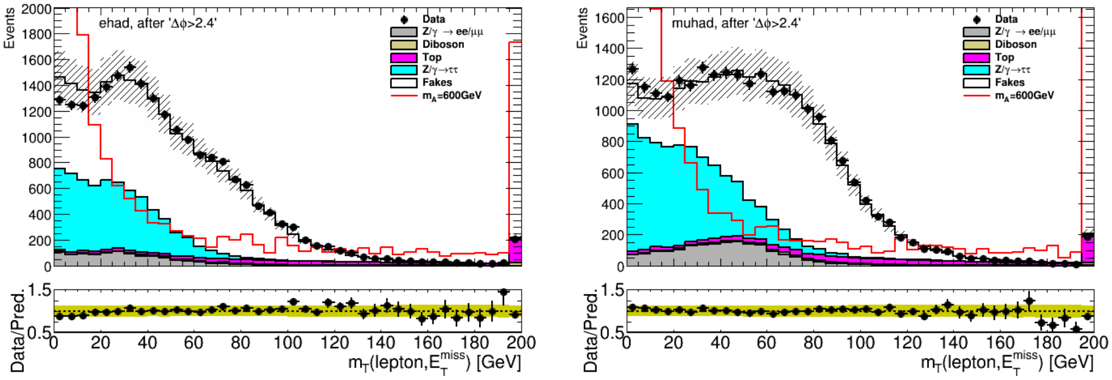

(a) (b)

Figure 5.21: The transverse mass between the lepton and the E_T^{miss} before the $m_T(\ell, E_T^{miss})$ requirement for the $e\tau_{had}$ (a) and $\mu\tau_{had}$ (b) channels.

5.5 *Systematic Uncertainties*

This section describes the systematic uncertainties pertinent to the use of simulated samples. A description of systematic uncertainties for data-driven background predictions can be found in the previous section.

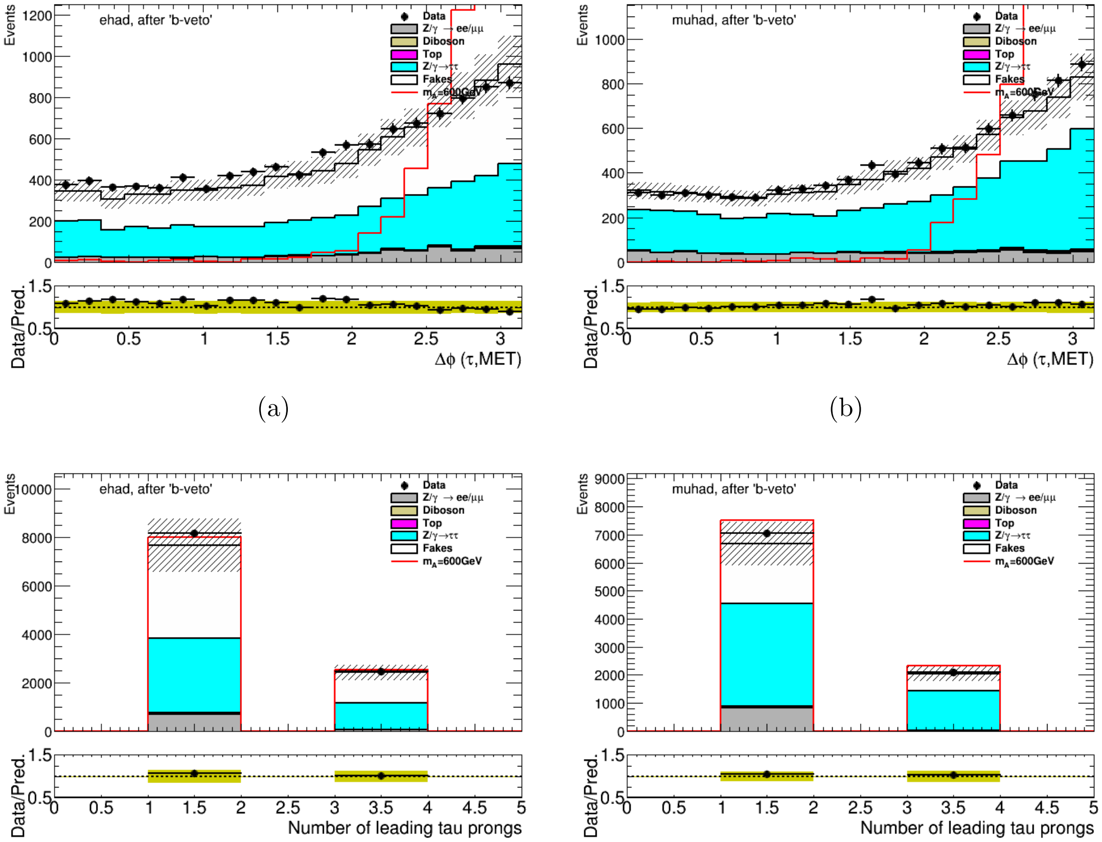

(a) (b)

(c) (d)

Figure 5.22: The distributions of $\Delta\phi(\tau_{had}, E_T^{miss})$ (a,b) and number of tau tracks (c,d) for the full selection in the $e\tau_{had}$ (left) and $\mu\tau_{had}$ (right) channels.

5.5.1 Luminosity and cross section uncertainties

There is a 5% uncertainty on the integrated luminosity measurement which should be applied to any event taken from simulation. In the case of this analysis, these correspond to events with truth-matched lepton and hadronic tau. The main backgrounds affected by this uncertainty are $Z \to \tau\tau$ and $t\bar{t}$. The production cross-sections used to scale the simulated events also have theoretical uncertainties. The most important simulated background samples used in this analysis are $Z \to \tau\tau$ and diboson, which carry uncertainties of 5% and 6%, respectively.

5.5.2 Detector-related uncertainties

The simulated detector response and software performance in Monte Carlo generated events has several systematic uncertainties. They can be due to:

- the reconstruction and identification of τ_{had} (Tau reco/ID);
- the reconstruction of the energy of the τ_{had}, also referred to as the τ_{had} energy scale (Tau e-scale);
- the efficiencies of muon triggers, as well as the subsequent reconstruction, isolation, identification and energy scale of simulated muons ("Muon");
- the efficiencies of electron triggers, as well as the subsequent reconstruction, isolation, identification and energy scale of simulated electrons ("Electron");
- uncertainties in the E_T^{miss} calculation for simulated events ("MET");
- jet energy scale and resolution ("Jet");
- the flavor-tagging algorithm efficiency ("*b*-tagging");

Table 5.9: The effect of the systematic uncertainties in the MC samples used for the background estimation for the $e\tau_{had}$, b-veto category. The effect on the normalization in % is shown per sample.

Electron channel, backgrounds, b-veto				
Systematic	$Z \to \ell\ell$	Top	$Z \to \tau\tau$	Diboson
Muon	0.00	0.11	0.00	0.06
Electron	1.99	1.48	1.27	1.43
Tau reco/ID	0.03	10.43	10.81	10.09
Tau e-scale	0.00	5.75	2.22	5.21
Jet	2.58	5.23	2.51	1.79
MET	1.35	1.13	0.67	0.89
b-tagging	0.02	6.53	0.03	0.01
Pile-up	1.91	3.13	3.30	2.88

- the simplified simulation used for b-associated production signal samples, which use ALTFAST II ("AF2");

- pileup uncertainties due to the reweighting of MC samples to match the average interaction per bunch crossing ($\langle\mu\rangle$) profile of data events ("Pile-up").

The uncertainties are computed separately for the $e\tau_{had}$ and $\mu\tau_{had}$ channels, and a summary can be found in Tables 5.9-5.12.

5.5.3 Signal modelling uncertainties

Similarly to the $A \to Zh \to \ell\ell\tau\tau$ search, mismodelling in the simulated acceptance of our signal events is accounted for as an uncertainty on the normalization of our signal samples. The different MC tunings used to gauge the effect of incorrect event generation are described in Ref. [72] and [73] for gluon fusion and b-associated production, respectively. The final uncertainties differ for each signal mass hypothesis and are symmetrized according to their highest values. The implementation of the uncertainties is done as a linear m_A-dependent function:

Table 5.10: The effect of the systematic uncertainties in the MC samples used for the background estimation for the $\mu\tau_{had}$, b-veto category. The effect on the normalization in % is shown per sample.

Muon channel, backgrounds, b-veto				
Systematic	$Z \to \ell\ell$	Top	$Z \to \tau\tau$	Diboson
Muon	0.96	2.42	1.25	1.83
Electron	0.00	0.00	0.01	0.11
Tau reco/ID	0.00	10.84	11.06	10.71
Tau e-scale	0.00	5.53	4.51	5.88
Jet	3.17	5.00	2.97	3.76
MET	3.23	0.57	0.86	1.20
b-tagging	0.07	6.26	0.03	0.01
Pile-up	0.96	2.98	2.43	2.24

Table 5.11: The effect of the systematic uncertainties in the MC samples used signal events in the $e\tau_{had}$, b-veto category. The effect on the normalization in % is shown per sample.

Electron channel, signal, gluon fusion, b-veto category						
Systematic	ggH200	ggH300	ggH400	ggH500	ggH800	ggH1000
Electron	0.94	1.22	0.99	1.14	1.51	1.74
Tau reco/ID	11.32	9.05	7.84	7.43	7.99	8.66
Tau e-scale	8.55	5.43	5.07	4.27	4.27	3.27
Jet	2.75	3.21	1.87	2.07	1.95	2.07
MET	1.22	1.23	0.51	0.61	0.51	1.09
b-tagging	0.02	0.05	0.03	0.03	0.04	0.04
Pile-up	2.17	5.61	1.42	3.71	0.78	5.10
Electron channel, signal, b-associated production, b-veto category						
Systematic	bbH200	bbH300	bbH400	bbH500	bbH800	bbH1000
Muon	0.04	0.04	0.04	0.06	0.04	0.03
Electron	1.37	1.13	1.30	1.47	1.85	2.01
Tau reco/ID	11.39	8.90	8.10	7.36	7.96	8.60
Tau e-scale	5.62	5.17	4.42	3.70	4.04	0.93
Jet	3.13	2.15	2.06	2.28	1.86	2.26
MET	1.90	0.50	0.40	0.57	0.60	0.48
AF2	3.69	2.48	2.35	2.22	2.19	2.17
b-tagging	1.64	1.83	1.81	1.79	1.82	1.73
Pile-up	1.22	3.31	1.99	0.66	1.86	0.90

Table 5.12: The effect of the systematic uncertainties in the MC samples used for signal events in the $\mu\tau_{had}$, b-veto category. The effect on the normalization in % is shown per sample.

Muon channel, signal, gluon fusion, b-veto category						
Systematic	ggH200	ggH300	ggH400	ggH500	ggH800	ggH1000
Muon	1.84	2.31	2.70	2.83	3.13	3.32
Electron	0.00	0.00	0.00	0.00	0.00	0.00
Tau reco/ID	12.00	9.38	8.12	7.58	7.96	8.67
Tau e-scale	2.73	3.58	4.25	4.11	4.15	3.55
Jet	2.22	2.71	2.43	2.13	2.59	2.31
MET	0.56	0.60	1.06	0.55	0.57	0.58
b-tagging	0.03	0.05	0.04	0.04	0.06	0.05
Pile-up	0.88	1.69	0.63	1.33	3.40	3.96
Muon channel, signal, b-associated production, b-veto category						
Systematic	bbH200	bbH300	bbH400	bbH500	bbH800	bbH1000
Muon	1.79	2.46	2.71	2.99	3.23	3.38
Electron	0.06	0.09	0.05	0.02	0.04	0.03
Tau reco/ID	11.85	9.20	8.28	7.43	7.86	8.49
Tau e-scale	3.22	4.07	4.22	4.40	5.01	2.71
Jet	4.06	2.41	2.59	3.37	2.29	2.93
MET	0.78	1.12	0.56	0.46	0.65	0.57
AF2	2.91	2.57	2.49	2.43	2.22	2.20
b-tagging	1.50	1.73	1.76	1.81	1.96	1.84
Pile-up	0.81	2.25	0.26	2.62	4.16	2.52

- $10.367 \times 10^{-5} m_A + 0.18065$ for b-associated production,
- $-2.908 \times 10^{-5} m_A + 0.1845$ for gluon fusion production,

where the mass of the Higgs boson, m_A, is given in units of GeV. Tables 5.13-5.14 show the final signal modelling uncertainties.

Table 5.13: Summary of uncertainties of $gg \to H/A$ signal samples in b-veto category.

Mass	1-	1+	2-	2+	renormMultFac do	renormMultFac up	pT0Ref do	pT0Ref up	scale	PDF	Total
$200 GeV$	2.4%	0.8%	0.3%	0.5%	2.5%	1.8%	1.7%	2.5%	17.4%	4.1%	18.3%
$500 GeV$	0.3%	2.2%	0.4%	0.1%	1.6%	0.9%	0.5%	0.5%	15.5%	4.8%	16.3%
$1000 GeV$	1.1%	0.9%	1.1%	0.5%	1.6%	0.3%	1.1%	1.0%	15.1%	4.3%	15.8 %

Table 5.14: Summary of uncertainties of $gg \to bb(H/A)$ signal samples in b-veto category.

Mass	1	2	3	combine tune variation	scale	PDF	Total
200 GeV	4.429%	3.698%	0.950%	5.848%	19.088%	5.756%	20.777%
500 GeV	5.888%	0.760%	3.055%	6.677%	20.182%	6.494%	22.228%
1000 GeV	1.069%	0.591%	0.666%	1.391%	25.719%	12.922%	28.816%

5.6 Results

The final distribution of the m_T^{tot} discriminant for the observed data is in good agreement with the predicted background, as can be seen in Figure 5.23. Additional kinematic distributions for the $e\tau_{had}$ and $\mu\tau_{had}$ channels are shown in Figures 5.24 and 5.25. The uncertainty band includes both statistical and systematic uncertainties, with their likelihood-fit values, as described in Appendix B.

The results from the $e\tau_{had}$ and $\mu\tau_{had}$ b-veto categories are combined to improve the sensitivity. As in the $A \to Zh$ analysis, the parameter of interest in the search is the signal strength μ given by the ratio of the fitted signal production cross section to its counterpart value predicted by the MSSM signal assumption. Upper limits on the cross section times branching ratio of general heavy neutral Higgs bosons are set for both gluon fusion and b-associated production at 95% confidence-level. Figure 5.26 shows $\sigma \times$ BR limits for the combined $e\tau_{had}$+$\mu\tau_{had}$ search. Separate limits for each $\tau_{lep}\tau_{had}$ channel can be found in Figure 5.27. The results are interpreted in the m_h^{mod+} scenario, and points in the $m_A - \tan\beta$ plane with signal hypotheses incompatible with the previously calculated production upper limits are excluded.

A search for neutral MSSM Higgs bosons decaying to tau pairs has already been conducted in ATLAS using 8 TeV Run-1 data [74]. The search of $H/A \to \tau_{lep}\tau_{had}$ search presented here aims for a public result that includes the $\tau_{had}\tau_{had}$ decay channel, and events with and without b-tagged jets. The results are interpreted in a variety of benchmark scenarios of the MSSM (for a detailed description, see Ref. [31]). The combined Run-2 analysis is more sensitive than the Run-1 analysis in the entire mass range being considered, as can be seen in Figure 5.29(d). An early Run-2 result without b-tagging has already been made public [75].

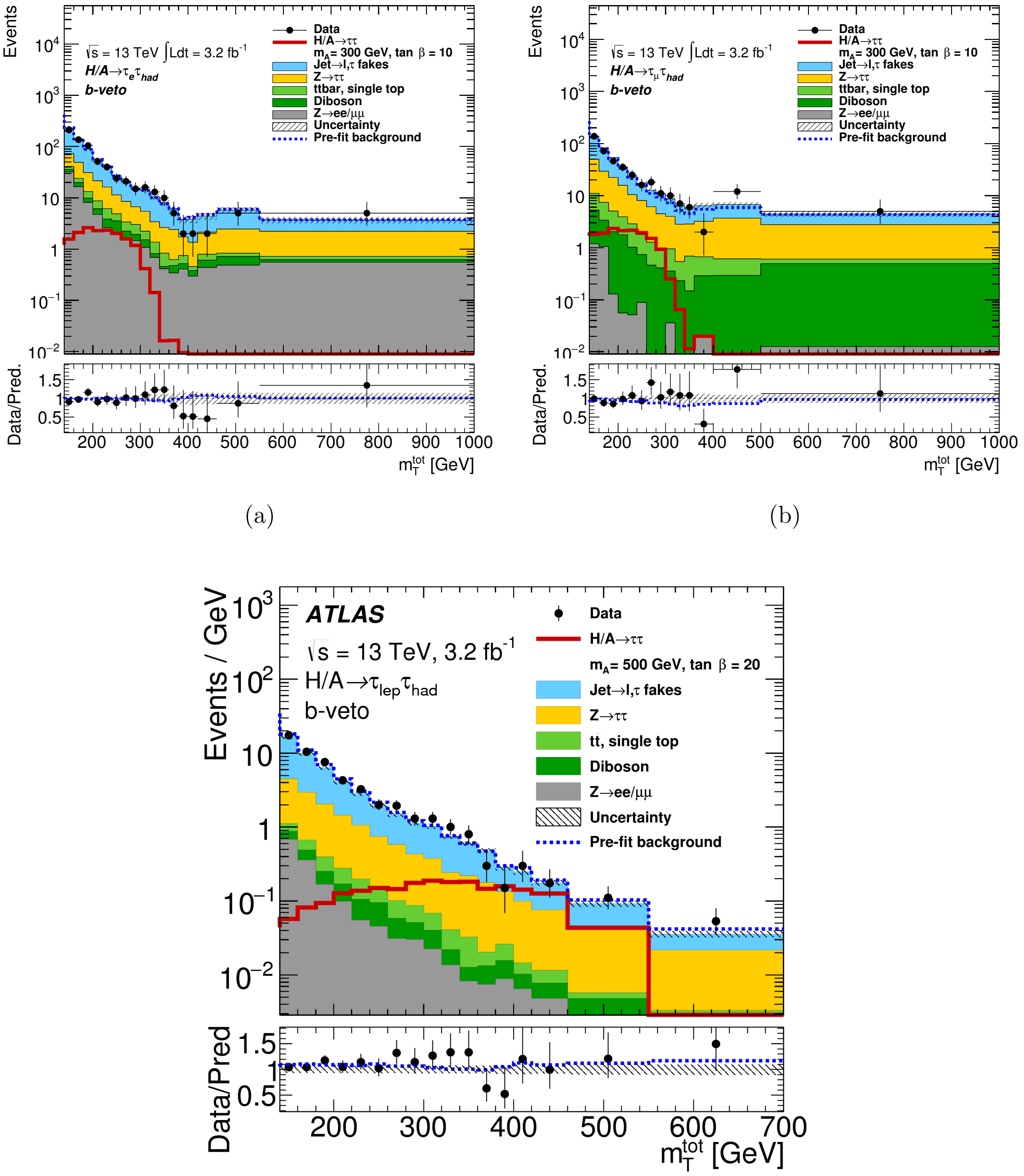

(a)

(b)

(c)

Figure 5.23: Final distributions of the total transverse mass for $e\tau_{had}$ (a), $\mu\tau_{had}$ (b) and combined (c) categories.

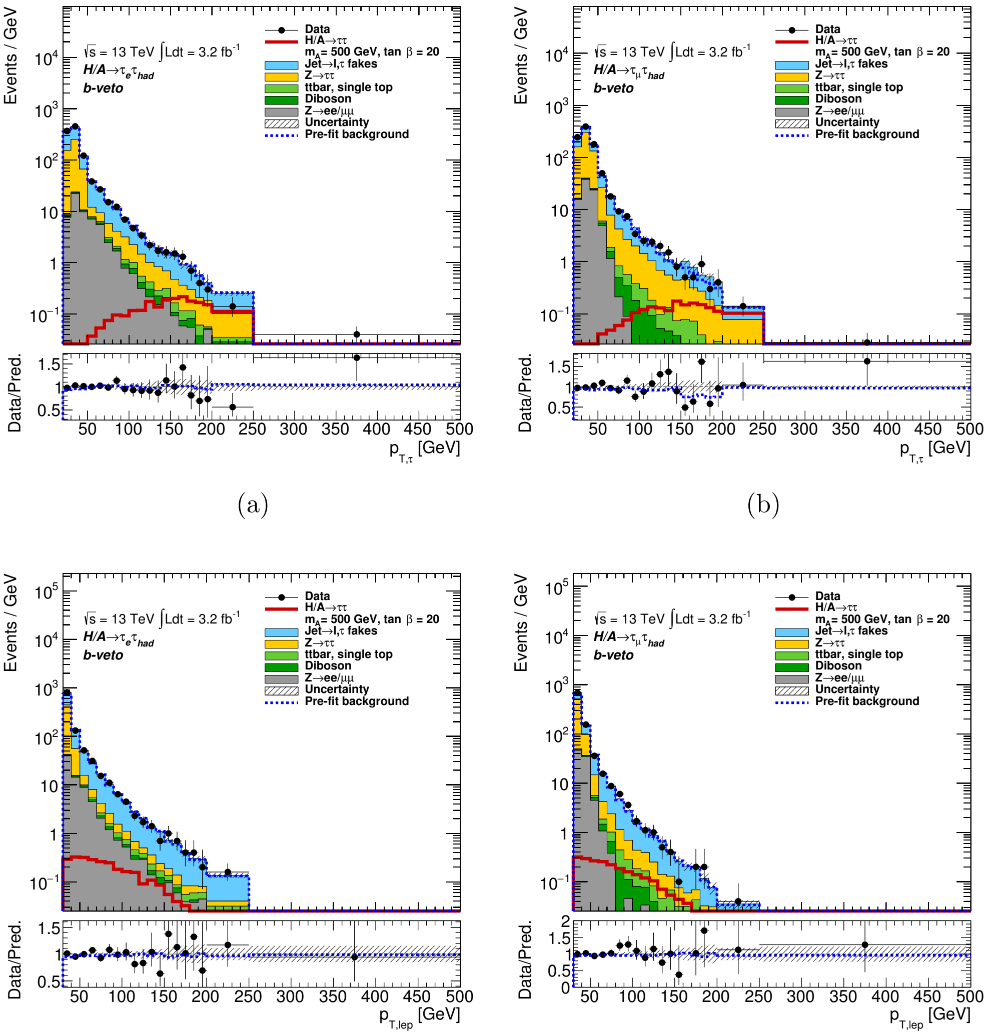

(a) (b) (c) (d)

Figure 5.24: Distributions in the electron (left) and muon (right) channels of the $\tau_{had} p_T$ (top) and lepton p_T (bottom). The background predictions and uncertainties used are from the likelihood fit result (see Appendix B).

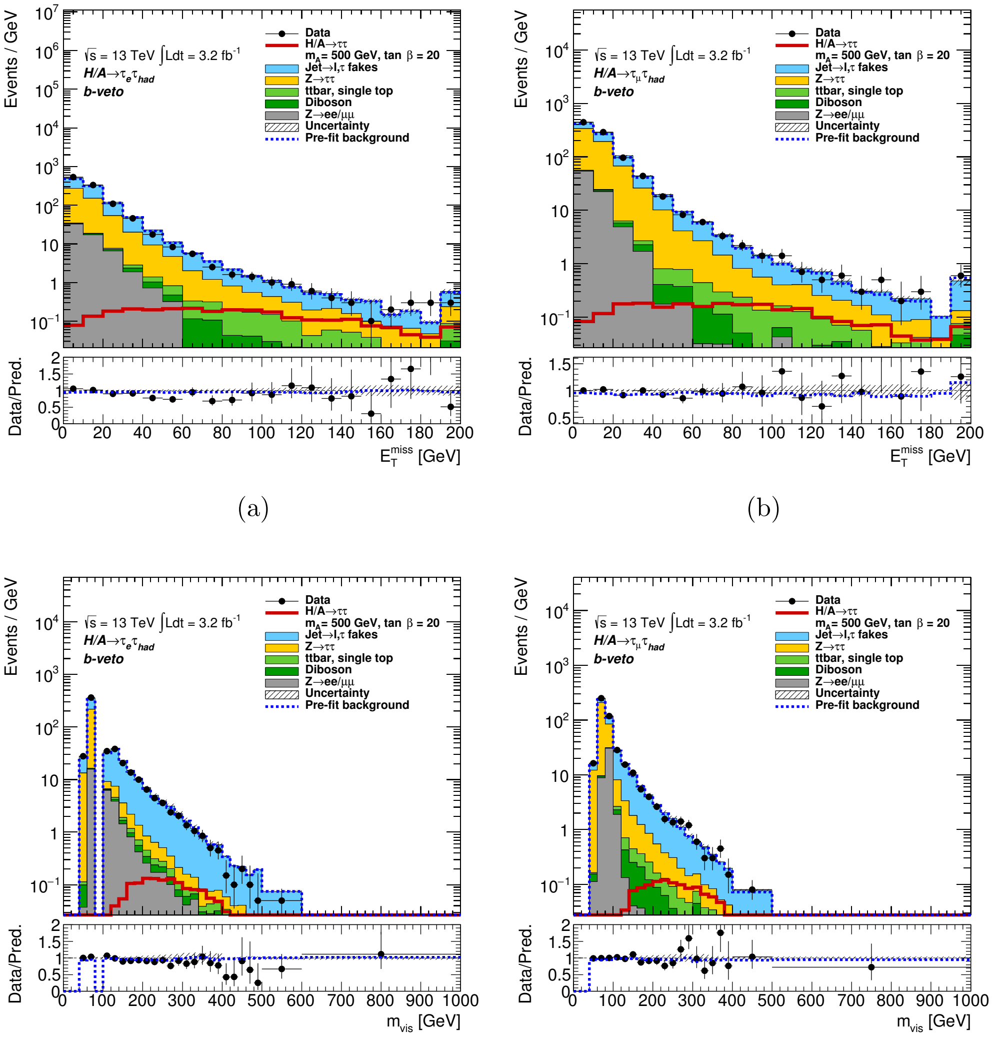

(a) (b)

(c) (d)

Figure 5.25: Distributions in the electron (left) and muon (right) channels of the E_T^{miss} (top) and visible mass (bottom). The background predictions and uncertainties used are from the likelihood fit result (see Appendix B).

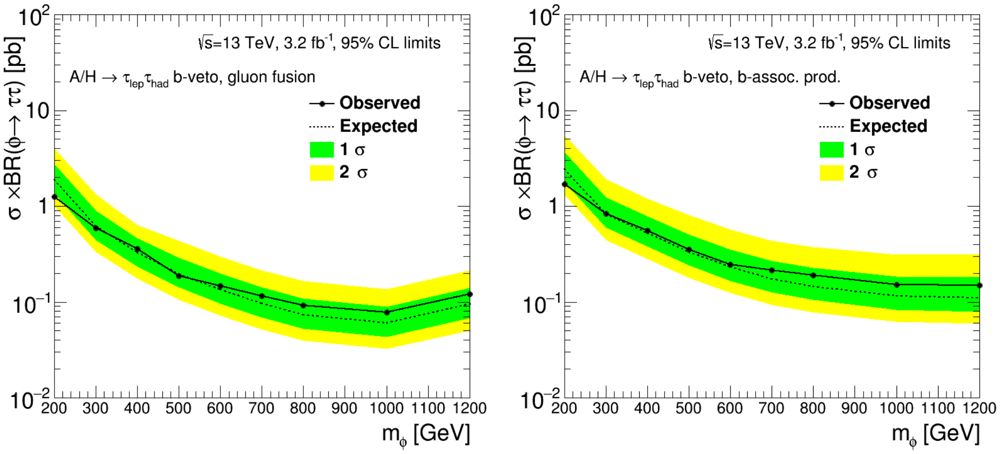

(a)

(b)

Figure 5.26: The 95% CL upper limit on the production cross section times branching ratio to $\tau_{lep}\tau_{had}$ of a single scalar boson produced via gluon fusion (a) or b-associated production (b) in the b-veto category for 3210 pb^{-1} of integrated luminosity at 13 TeV.

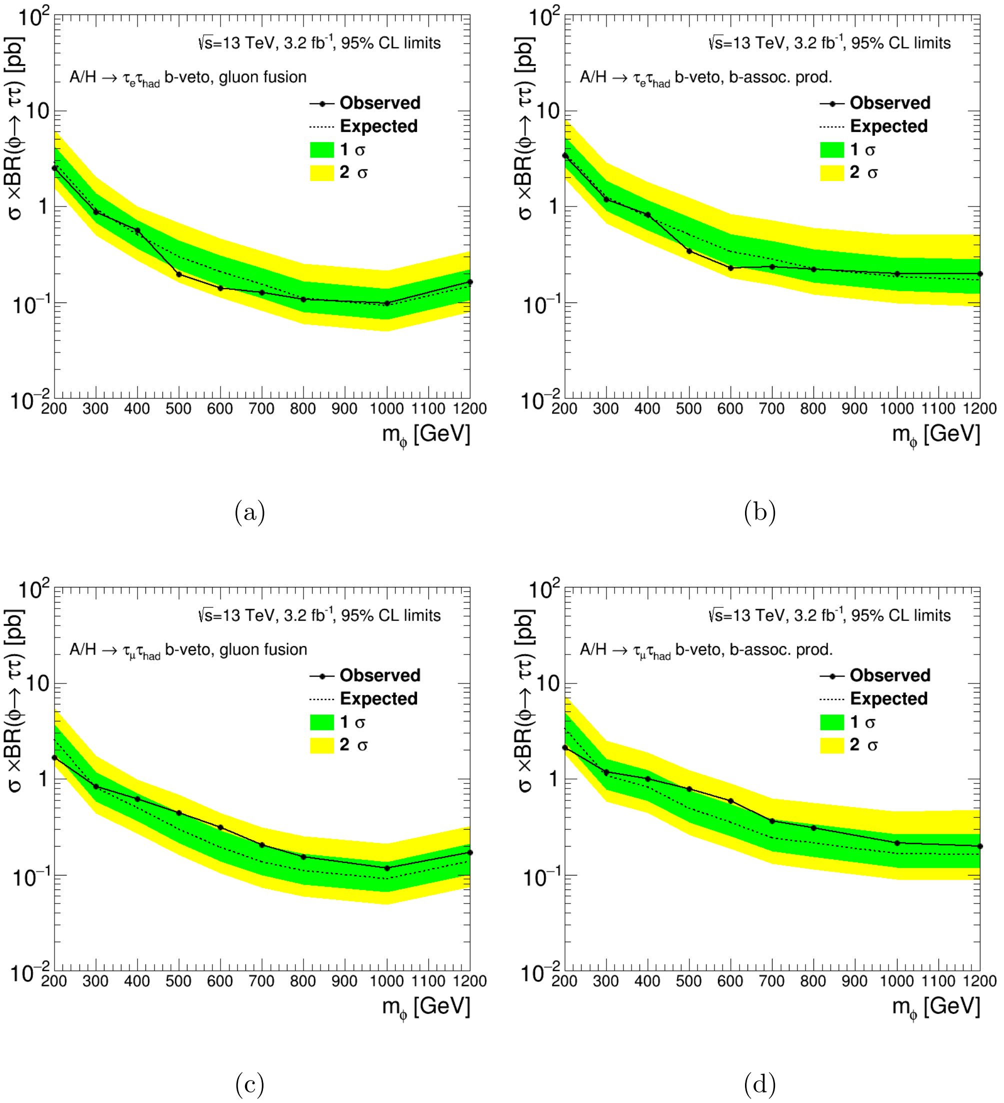

(a)

(b)

(c)

(d)

Figure 5.27: The 95% CL upper limit on the production cross section times branching ratio to $\tau_{lep}\tau_{had}$ of a single scalar boson produced via gluon fusion (left) or b-associated production (right) for the $e\tau_{had}$ (top) and $\mu\tau_{had}$ (bottom) channels in the b-veto category.

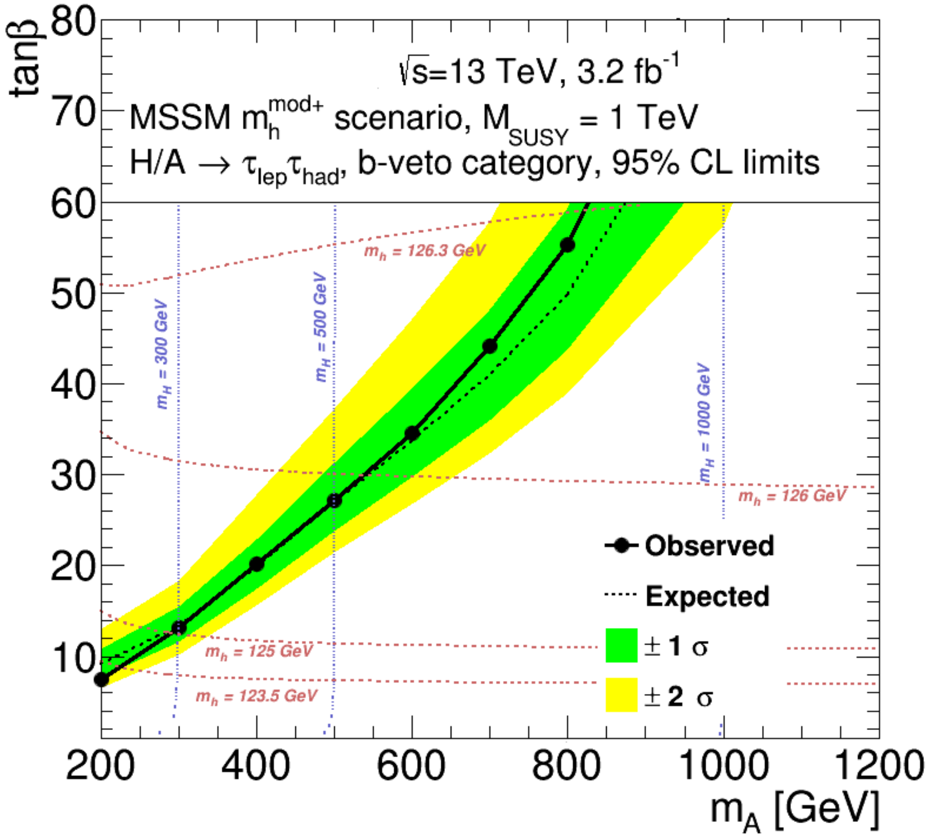

Figure 5.28: Interpretation of the results from the $\tau_{lep}\tau_{had}$ channal in the m_h^{mod+} scenario of the MSSM. Dashed lines of constant m_h and m_H are shown in red and blue, respectively.

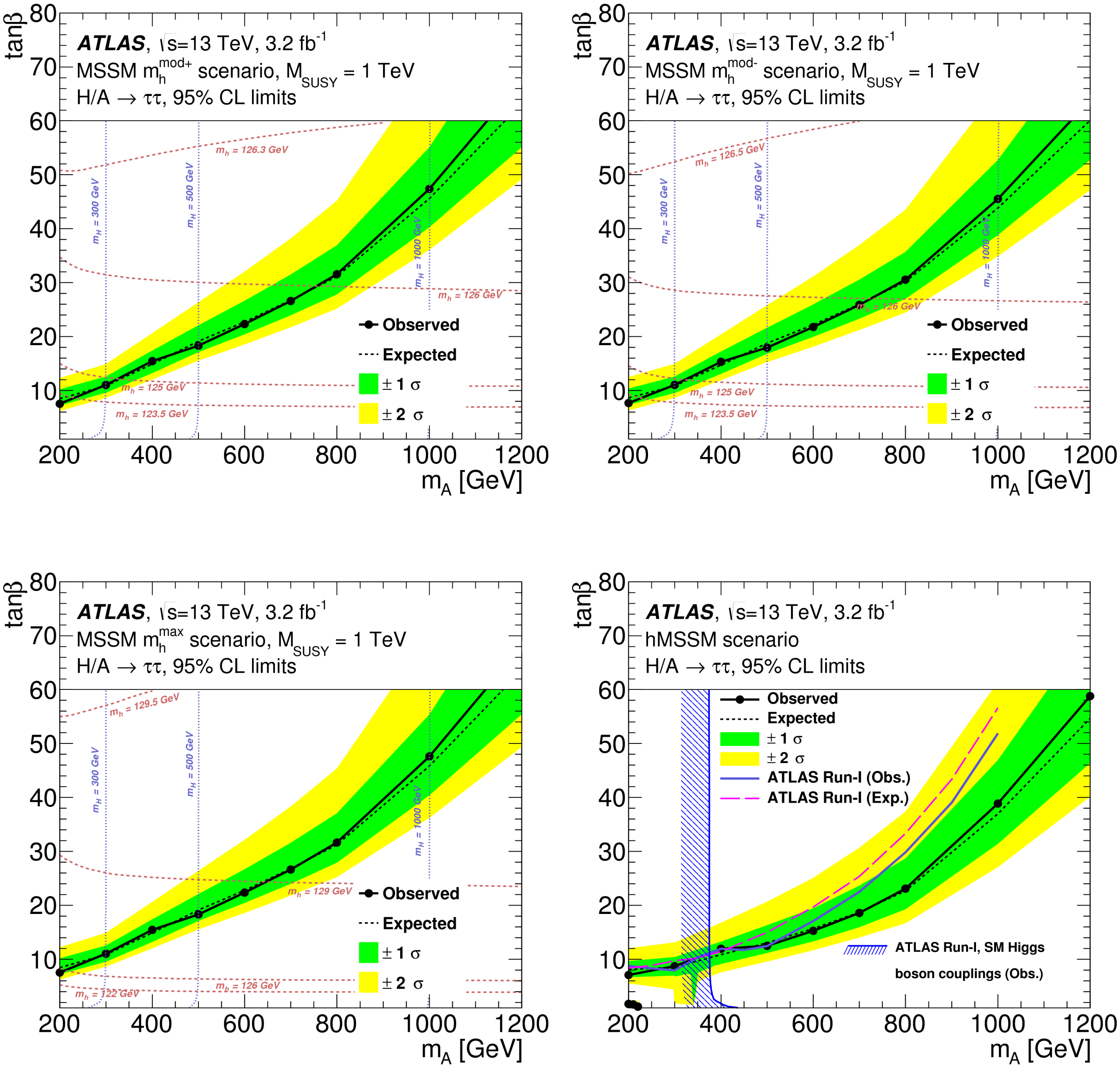

Figure 5.29: Comparison of the exclusion in the $m_A - \tan\beta$ plane of the m_h^{mod+} (a), m_h^{mod-} (b), m_h^{max} (c) and hMSSM (d) scenarios for the combined $(\tau_{lep}\tau_{had} + \tau_{had}\tau_{had})$ Run-2 $H/A \to \tau\tau$ search. Dashed lines of constant m_h and m_H are shown in red and blue, respectively.

Chapter 6

SUMMARY AND CONCLUSION

The searches for a heavy CP-odd 2HDM Higgs boson A decaying to Zh in the $\ell\ell\tau_{lep}\tau_{had}$ final state and for heavy neutral MSSM H/A Higgs bosons decaying to $\tau_{lep}\tau_{had}$ in events without b-tagged jets are presented. The former considers the gluon fusion production mechanism, while the latter considers both gluon fusion and b-associated production modes. The Standard Model background is estimated using both simulated events and data-driven predictions.

Neither search shows statistically significant excesses compared to the SM prediction. Upper limits on cross section times branching ratio for a general 2HDM CP-odd A and neutral MSSM H/A are set. Results are also interpreted within different 2HDM and MSSM scenarios, with significant regions of the relevant parameter space being excluded.

Though significant progress in probing the BSM Higgs sector has been made, large regions of the 2HDM and MSSM parameter space remain unexplored. The motivation for 2HDMs and/or Supersymmetry is still powerful. As the LHC collects more data and improved versions of the present analyses are being developed, new physics may be just around the corner.

BIBLIOGRAPHY

[1] G. Bertone, D. Hooper and J. Silk, "Particle dark matter: Evidence, candidates and constraints", *Phys. Rept.*, vol. 405, pp. 279–390, 2005.

[2] C. Rovelli, *Quantum Gravity* (Cambridge University Press2004). ISBN 978-0-511-75580-4.

[3] M. Dine and A. Kusenko, "The Origin of the matter - antimatter asymmetry", *Rev. Mod. Phys.*, vol. 76, p. 1, 2003.

[4] G. 't Hooft, "Naturalness, chiral symmetry, and spontaneous chiral symmetry breaking", *NATO Sci. Ser. B*, vol. 59, p. 135, 1980.

[5] The ATLAS Collaboration, "Observation of a new particle in the search for the Standard Model Higgs boson with the ATLAS detector at the LHC", *Phys. Lett.*, vol. B716, pp. 1–29, 2012.

[6] The CMS Collaboration, "Observation of a new boson at a mass of 125 GeV with the CMS experiment at the LHC", *Phys. Lett.*, vol. B716, pp. 30–61, 2012.

[7] The ATLAS Collaboration, "Study of the spin and parity of the Higgs boson in diboson decays with the ATLAS detector", *Eur. Phys. J.*, vol. C75(10), p. 476, 2015. [Erratum: Eur. Phys. J.C76,no.3,152(2016)].

[8] The ATLAS Collaboration, "Measurements of the Higgs boson production and decay rates and coupling strengths using pp collision data at $\sqrt{s} = 7$ and 8 TeV in the ATLAS experiment", *Eur. Phys. J.*, vol. C76(1), p. 6, 2016.

[9] The CMS Collaboration, "Precise determination of the mass of the Higgs boson and tests of compatibility of its couplings with the Standard Model predictions using proton collisions at 7 and 8 TeV", *Eur. Phys. J.*, vol. C75(5), p. 212, 2015.

[10] The CMS Collaboration, "Constraints on the spin-parity and anomalous HVV couplings of the Higgs boson in proton collisions at 7 and 8 TeV", *Phys. Rev.*, vol. D92(1), p. 012004, 2015.

[11] The ATLAS Collaboration, “Evidence for the Higgs-boson Yukawa coupling to tau leptons with the ATLAS detector”, *JHEP*, vol. 04, p. 117, 2015.

[12] The ATLAS Collaboration, “Search for the $b\bar{b}$ decay of the Standard Model Higgs boson in associated $(W/Z)H$ production with the ATLAS detector”, *JHEP*, vol. 01, p. 069, 2015.

[13] The CMS Collaboration, “Search for the Standard Model Higgs boson produced in association with a W or a Z boson and decaying to bottom quarks”, *Phys. Rev.*, vol. D89(1), p. 012003, 2014.

[14] P. W. Higgs, “Broken symmetries, massless particles and gauge fields”, *Phys. Lett.*, vol. 12, pp. 132–133, 1964.

[15] P. W. Higgs, “Broken Symmetries and the Masses of Gauge Bosons”, *Phys. Rev. Lett.*, vol. 13, pp. 508–509, 1964.

[16] P. W. Higgs, “Spontaneous Symmetry Breakdown without Massless Bosons”, *Phys. Rev.*, vol. 145, pp. 1156–1163, 1966.

[17] F. Englert and R. Brout, “Broken Symmetry and the Mass of Gauge Vector Mesons”, *Phys. Rev. Lett.*, vol. 13, pp. 321–323, 1964.

[18] G. S. Guralnik, C. R. Hagen and T. W. B. Kibble, “Global Conservation Laws and Massless Particles”, *Phys. Rev. Lett.*, vol. 13, pp. 585–587, 1964.

[19] S. P. Martin, “A Supersymmetry primer”, [Adv. Ser. Direct. High Energy Phys.18,1(1998)].

[20] P. Fayet, “Spontaneously broken supersymmetric theories of weak, electromagnetic and strong interactions”, *Physics Letters B*, vol. 69(4), pp. 489 – 494, 1977.

[21] J. Wess and B. Zumino, “Supergauge Transformations in Four-Dimensions”, *Nucl. Phys.*, vol. B70, pp. 39–50, 1974.

[22] S. Dimopoulos and H. Georgi, “Softly broken supersymmetry and SU(5)”, *Nuclear Physics B*, vol. 193(1), pp. 150 – 162, 1981.

[23] G. C. Branco *et al.*, “Theory and phenomenology of two-Higgs-doublet models”, *Phys. Rept.*, vol. 516, pp. 1–102, 2012.

[24] W. Greiner, S. Schramm and E. Stein, *Quantum Chromodynamics* (Springer2007). ISBN 978-3-540-48535-3.

[25] W. Greiner and B. Muller, *Gauge theory of weak interactions* (Springer1993). ISBN 978-3-540-87842-1.

[26] J. F. Gunion and H. E. Haber, "Conditions for CP-violation in the general two-Higgs-doublet model", *Phys. Rev.*, vol. D72, p. 095002, 2005.

[27] R. D. Peccei, "The Strong CP problem and axions", *Lect. Notes Phys.*, vol. 741, pp. 3–17, 2008.

[28] A. Djouadi, "The Anatomy of electro-weak symmetry breaking. II. The Higgs bosons in the minimal supersymmetric model", *Phys. Rept.*, vol. 459, pp. 1–241, 2008.

[29] A. Arbey *et al.*, "Implications of a 125 GeV Higgs for supersymmetric models", *Phys. Lett.*, vol. B708, pp. 162–169, 2012.

[30] A. Djouadi *et al.*, "The Minimal supersymmetric Standard Model: Group summary report", in "GDR (Groupement De Recherche) - Supersymetrie Montpellier, France, April 15-17, 1998", (1998).

[31] M. Carena *et al.*, "MSSM Higgs Boson Searches at the LHC: Benchmark Scenarios after the Discovery of a Higgs-like Particle", *Eur. Phys. J.*, vol. C73(9), p. 2552, 2013.

[32] LHC Higgs Cross Section Working Group, "BSM Higgs production cross sections at $\sqrt{s} = 13$ TeV (update in CERN Report 4 2016)", URL `https://twiki.cern.ch/twiki/bin/view/LHCPhysics/CERNYellowReportPageBSMAt13TeV`.

[33] LHC Higgs Cross Section Working Group, "LHC Higgs Cross Section WG Picture Gallery", URL `https://twiki.cern.ch/twiki/bin/view/LHCPhysics/LHCHXSWGCrossSectionsFigures`.

[34] L. Evans and P. Bryant, "LHC Machine", *JINST*, vol. 3(08), p. S08001, 2008.

[35] The ATLAS Collaboration, "The ATLAS Experiment at the CERN Large Hadron Collider", *JINST*, vol. 3, p. S08003, 2008.

[36] The ATLAS Collaboration, "2015 start-up trigger menu and initial performance assessment of the ATLAS trigger using Run-2 data", ATL-DAQ-PUB-2016-001, CERN, Geneva, 2016.

[37] J. Alwall *et al.*, “MadGraph 5: going beyond”, *JHEP*, vol. 2011(6), pp. 1–40, 2011.

[38] T. Sjöstrand, S. Mrenna and P. Skands, “A brief introduction to PYTHIA 8.1”, *Comput. Phys. Commun.*, vol. 178(11), pp. 852 – 867, 2008.

[39] R. V. Harlander, S. Liebler and H. Mantler, “SusHi: A program for the calculation of Higgs production in gluon fusion and bottom-quark annihilation in the Standard Model and the MSSM”, *Comput. Phys. Commun.*, vol. 184, pp. 1605–1617, 2013.

[40] D. Eriksson, J. Rathsman and O. Stal, “2HDMC: Two-Higgs-Doublet Model Calculator Physics and Manual”, *Comput. Phys. Commun.*, vol. 181, pp. 189–205, 2010.

[41] T. Gleisberg *et al.*, “Event generation with SHERPA 1.1”, *JHEP*, vol. 2009(02), p. 007, 2009.

[42] S. Frixione, P. Nason and C. Oleari, “Matching NLO QCD computations with parton shower simulations: the POWHEG method”, *JHEP*, vol. 2007(11), p. 070, 2007.

[43] E. Re, “Single-top production with the POWHEG method”, *PoS*, vol. DIS2010, p. 172, 2010.

[44] B. P. Kersevan and E. Richter-Was, “The Monte Carlo event generator AcerMC versions 2.0 to 3.8 with interfaces to PYTHIA 6.4, HERWIG 6.5 and ARIADNE 4.1”, *Comput. Phys. Commun.*, vol. 184, pp. 919–985, 2013.

[45] The ATLAS Collaboration, “The ATLAS Simulation Infrastructure”, *Eur. Phys. J.*, vol. C70, pp. 823–874, 2010.

[46] The ATLAS Collaboration, “Electron reconstruction and identification efficiency measurements with the ATLAS detector using the 2011 LHC proton-proton collision data”, *Eur. Phys. J.*, vol. C74(7), p. 2941, 2014.

[47] The ATLAS Collaboration, “Electron and photon energy calibration with the ATLAS detector using LHC Run 1 data”, *Eur. Phys. J.*, vol. C74(10), p. 3071, 2014.

[48] The ATLAS Collaboration, “Measurement of the muon reconstruction performance of the ATLAS detector using 2011 and 2012 LHC proton–proton collision data”, *Eur. Phys. J.*, vol. C74(11), p. 3130, 2014.

[49] The ATLAS Collaboration, “Topological cell clustering in the ATLAS calorimeters and its performance in LHC Run 1”, CERN-PH-EP-2015-304, 2016.

[50] M. Cacciari, G. P. Salam and G. Soyez, "The Anti-k(t) jet clustering algorithm", *JHEP*, vol. 04, p. 063, 2008.

[51] The ATLAS Collaboration, "Identification and energy calibration of hadronically decaying tau leptons with the ATLAS experiment in *pp* collisions at $\sqrt{s}$=8 TeV", *Eur. Phys. J.*, vol. C75(7), p. 303, 2015.

[52] The ATLAS Collaboration, "Performance of Missing Transverse Momentum Reconstruction in ATLAS studied in Proton-Proton Collisions recorded in 2012 at 8 TeV", ATLAS-CONF-2013-082, CERN, Geneva, 2013.

[53] A. Elagin, P. Murat, A. Pranko and A. Safonov, "A New Mass Reconstruction Technique for Resonances Decaying to di-tau", *Nucl. Instrum. Meth.*, vol. A654, pp. 481–489, 2011.

[54] P. Skands, "Introduction to QCD", in "Proceedings, Theoretical Advanced Study Institute in Elementary Particle Physics: Searching for New Physics at Small and Large Scales (TASI 2012)", pp. 341–420 (2013).

[55] J. M. Campbell, R. K. Ellis and C. Williams, "Vector boson pair production at the LHC", *JHEP*, vol. 07, p. 018, 2011.

[56] S. Dittmaier *et al.*, "Handbook of LHC Higgs Cross Sections: 2. Differential Distributions", CERN-2012-002, 2012.

[57] A. D. Martin, W. J. Stirling, R. S. Thorne and G. Watt, "Parton distributions for the LHC", *Eur. Phys. J.*, vol. C63, pp. 189–285, 2009.

[58] R. D. Ball *et al.*, "Impact of heavy quark masses on parton distributions and LHC phenomenology", *Nuclear Physics B*, vol. 849(2), pp. 296 – 363, 2011.

[59] The ATLAS Collaboration, "Search for a CP-odd Higgs boson decaying to Zh in pp collisions at $\sqrt{s}$ = 8 TeV with the ATLAS detector", *Phys. Lett.*, vol. B744, pp. 163–183, 2015.

[60] S. Alioli, P. Nason, C. Oleari and E. Re, "NLO Higgs boson production via gluon fusion matched with shower in POWHEG", *JHEP*, vol. 2009(04), p. 002, 2009.

[61] T. Sjöstrand *et al.*, "An introduction to PYTHIA 8.2", *Comput. Phys. Commun.*, vol. 191, pp. 159 – 177, 2015.

[62] T. Sjöstrand, S. Mrenna and P. Skands, "PYTHIA 6.4 physics and manual", *JHEP*, vol. 2006(05), p. 026, 2006.

[63] J. Alwall *et al.*, "The automated computation of tree-level and next-to-leading order differential cross sections, and their matching to parton shower simulations", *JHEP*, vol. 2014(7), pp. 1–157, 2014.

[64] M. Wiesemann *et al.*, "Higgs production in association with bottom quarks", *JHEP*, vol. 2015(2), pp. 1–35, 2015.

[65] The ATLAS Collaboration, "The simulation principle and performance of the ATLAS fast calorimeter simulation FastCaloSim", ATL-PHYS-PUB-2010-013, CERN, Geneva, 2010.

[66] The ATLAS Collaboration, "Electron identification measurements in ATLAS using $\sqrt{s}$ = 13 TeV data with 50 ns bunch spacing", ATL-PHYS-PUB-2015-041, CERN, Geneva, 2015.

[67] The ATLAS Collaboration, "Muon reconstruction performance of the ATLAS detector in proton–proton collision data at $\sqrt{s}$ =13 TeV", *Eur. Phys. J.*, vol. C76(5), p. 292, 2016.

[68] The ATLAS Collaboration, "Pile-up subtraction and suppression for jets in ATLAS", ATLAS-CONF-2013-083, CERN, Geneva, 2013.

[69] The ATLAS Collaboration, "Commissioning of the ATLAS b-tagging algorithms using $t\bar{t}$ events in early Run-2 data", ATL-PHYS-PUB-2015-039, CERN, Geneva, 2015.

[70] The ATLAS Collaboration, "Performance of missing transverse momentum reconstruction for the ATLAS detector in the first proton-proton collisions at $\sqrt{s}$= 13 TeV", ATL-PHYS-PUB-2015-027, CERN, Geneva, 2015.

[71] D. Cavalli *et al.*, "Reconstruction of Soft Missing Transverse Momentum with Inner Detector Tracks", ATL-COM-PHYS-2015-209, CERN, Geneva, 2015.

[72] The ATLAS Collaboration, "Measurement of the Z/γ^* boson transverse momentum distribution in pp collisions at $\sqrt{s} = 7$ TeV with the ATLAS detector", *JHEP*, vol. 09, p. 145, 2014.

[73] The ATLAS Collaboration, "ATLAS Run 1 Pythia8 tunes", ATL-PHYS-PUB-2014-021, CERN, Geneva, 2014.

[74] The ATLAS Collaboration, "Search for neutral Higgs bosons of the minimal supersymmetric Standard Model in pp collisions at $\sqrt{s} = 8$ TeV with the ATLAS detector", *JHEP*, vol. 11, p. 056, 2014.

[75] The ATLAS Collaboration, "Search for Neutral Minimal Supersymmetric Standard Model Higgs Bosons $H/A \to \tau\tau$ produced in pp collisions at $\sqrt{s} = 13$ TeV with the ATLAS Detector", ATLAS-CONF-2015-061, CERN, Geneva, 2015.

[76] P. Fayet, "Supersymmetry and Weak, Electromagnetic and Strong Interactions", *Phys. Lett.*, vol. B64, p. 159, 1976.

[77] P. Fayet, "Relations between the masses of the superpartners of leptons and quarks, the goldstino coupling and the neutral currents", *Physics Letters B*, vol. 84(4), pp. 416 – 420, 1979.

[78] A. L. Read, "Presentation of search results: the CL s technique", *Journal of Physics G: Nuclear and Particle Physics*, vol. 28(10), p. 2693, 2002.

[79] L. Breiman, J. H. Friedman, R. A. Olshen and C. J. Stone, *Classification and Regression Trees* (Chapman & Hall, New York1984).

[80] A. Hoecker *et al.*, "TMVA: Toolkit for Multivariate Data Analysis", *PoS*, vol. ACAT, p. 040, 2007.

[81] K. Cranmer, "Practical Statistics for the LHC", in "Proceedings, 2011 European School of High-Energy Physics (ESHEP 2011)", pp. 267–308 (2015).

[82] G. Cowan, K. Cranmer, E. Gross and O. Vitells, "Asymptotic formulae for likelihood-based tests of new physics", *Eur. Phys. J.*, vol. C71, p. 1554, 2011. [Erratum: Eur. Phys. J.C73,2501(2013)].

Appendix A

TAU IDENTIFICATION

A description of the reconstruction procedure for hadronic taus in ATLAS is found in Sections 4.2 and 5.2. Unfortunately, generic overlap removal between hadronically decaying taus and QCD jets usually does not meet the jet → τ_{had} background rejection requirements of ATLAS analyses. Because the online reconstruction of hadronic taus and jets must be fast, it is easier to optimize the discrimination between the two with a dedicated offline algorithm. For the majority of ATLAS analyses that involve hadronic taus, this algorithm is the TauID [51]. This appendix will describe in more detail how the TauID is able to distinguish hadronic taus from QCD jets.

A.1 Overview

The discrimination provided by the TauID is achieved through the use of Boosted Decision Trees (BDTs), a type of multivariate classifer [79]. A decision tree is fundamentally a branching collection of if-statements that assigns a classification score to any input given the path in the if-statement sequence the input followed. Because of their topological and kinematic differences, separate BDTs are provided for 1-track and 3-track hadronic taus. The BDT development is done with the Toolkit for Multivariate Analysis (`TMVA`) [80].

One of the advantages of BDTs is that the decision tree trains itself on what each if-statement (called *nodes*) should be, as well as the branching sequences they are applied in. This is done by giving two samples to the classifier that are representative of the events the user wishes to separate. For the case of the TauID, one is a collection of truth-matched τ_{had} objects from a simulated $Z \rightarrow \tau\tau$ sample, and the other is made of nearly all Run-1 data events collected by jet triggers. The BDT is told to find the optimal set of cuts that give maximum separation between the reconstructed taus from those two sets. The rejection of background events is done by applying a cut on the classification score that the BDT outputs (referred to as the BDT score). True-τ_{had} sample events receive a signal-like score approaching 1, while the multi-jet events receive a background-like score close to 0. A BDT score distribution for the TauID can be seen in Figure A.1(a). To avoid biases due to differences in the p_T spectrum of the samples, the multi-jet events are reweighted according to the true-τ_{had} transverse momentum distribution. A similar reweighting is done for the distribution of the number of primary vertices, since the simulated samples do not perfectly match the pileup profile observed in data.

To improve the rejection performance, the BDT classifier is also subjected to a reweighting procedure called *boosting*. The TauID employs the most popular type of boosting algorithm, called adaptive boosting or *AdaBoost*. Adaptive boosting consists of applying the classifier sequentially and, at each iteration, reweighting previously misclassified events by a boosting weight. The boosting weight is defined as

$$\alpha = \frac{1 - \mathrm{err}}{\mathrm{err}}, \tag{A.1}$$

where err is the misclassification rate of the previous tree. Thus, a tree with a misclassification rate of 20% will have its misclassified events weighted by a factor of 4, forcing the next classifier to take these misclassified events into stronger consideration during its training. After the boosting weight is applied, the samples are renormalized to their original scale so that the event weight sum is constant. For *AdaBoost*, the classifier score of a boosted event is given by

$$y_{\mathrm{boost}} = \frac{1}{\mathrm{N}_{\mathrm{collection}}} \cdot \sum_{i}^{\mathrm{N}_{\mathrm{collection}}} \ln(\alpha_i) \cdot h_i(\boldsymbol{x}), \tag{A.2}$$

where $h_i(\boldsymbol{x})$ is the unboosted classification score of the i-th event using the input variable set $\boldsymbol{x}$.

It is important to note that one cannot give the BDT an endless number of variables to select on, or allow it to have too large branching sequences (i.e. large *depth*), otherwise one runs into the issue of overtraining. Overtraining occurs when the tree has excessive depth, too many input variables and not enough event population, as it will find progressively finer cuts that exploit statistical effects in the training variable distributions that are not representative of the physical processes trying to be separated. Since more depth and input variables generally lead to higher separation power, one must find the optimal training setup that is just short of causing overtrained behavior. One way to reduce overtraining is through the practice of pruning, which removes nodes and branches that have low separation power. We can check if the BDT classifier has been overtrained by comparing its performance on training events and events from the same input samples that were not used in the training (test events). For the TauID, roughly 1/3 of events of each sample are randomly selected for testing purposes and kept in reserve, while the remaining 2/3 are used for the training. Figure A.1(b) shows a comparison of the classification performance of an early TauID tuning that suffered from overtraining. The classification performance is displayed as the functional dependence of the rejection efficiency on the signal acceptance, i.e. the cut on the BDT score used.

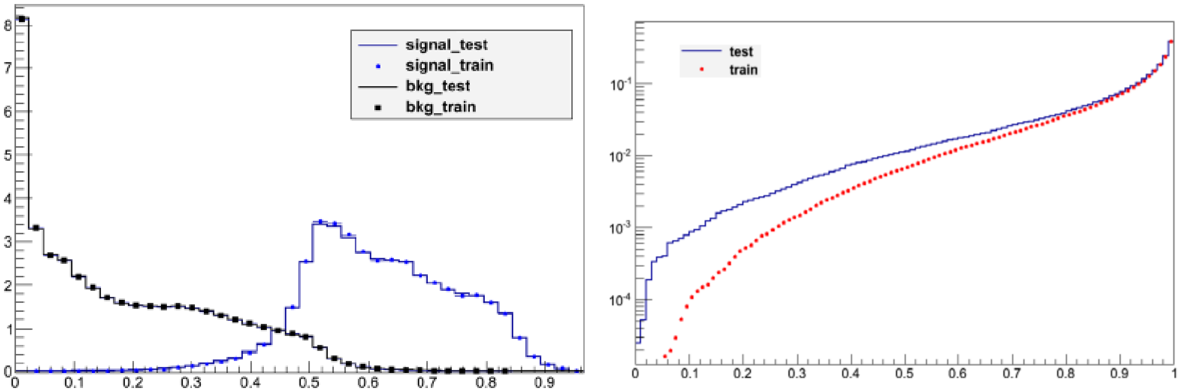

(a) (b)

Figure A.1: A typical BDT score distribution from the TauID classifier (left) and an overtrained BDT from an early iteration of the TauID (right), where the background rejection with events used for training was higher than for events used for testing.

A.2 Discriminating Variables

The chosen discriminating variables used to train the TauID BDT classifier are those that capture the differences between τ_{had} and QCD jets. Perhaps the most important difference between the two is that τ_{had}-jets are generally more collimated than QCD jets. The former has a cone angle of typically $\Delta R \lesssim 0.2$, compared to the latter's $\Delta R \sim 0.4$. Thus, it is useful to break down the shower cone into two regions: the $\Delta R \leq 0.2$ *core region* and the $0.2 < \Delta R < 0.4$ *isolation region*. With those two regions, it is easy to define several input variables centered around the energy or track distributions, such as the number of tracks in the isolated region N^{iso}_{track}, and the central energy fraction f_{cent}, defined below. Because taus have a finite lifetime, it is also possible to use variables that exploit the tau decay length.

The Run-1 TauID was the first time in ATLAS that information from π^0 mesons originating from the τ_{had} were used in τ_{had} identification. The π^0 identification was done by another BDT-based algorithm that used track and cluster information to identify deposits likely due to neutral pions. The number of π^0's in the jet is used as a discriminant variable, and their energy and transverse momenta helps define two others. The full list of input variables used to train the Run-1 TauID classifier is given below, with distributions shown in Figures A.2-A.5.

- Leading track momentum fraction (f_{track}): defined as the p_T of the leading track in the core region divided by the sum of all the energy in all TopoClusters in the core region. A correction based on the number of primary vertices is applied in order to remove biases due to pileup.

- Central energy fraction (f_{cent}): the fraction of the energy from topo clusters with $\Delta R < 0.1$ divided by that of the entire core region. Similarly to f_{track}, a correction based on the number of primary vertices is applied to remove biases due to pileup.

- Number of π^0 mesons (N_{π^0}): the number of neutral pions reconstructed in the core region.

- Number of tracks in the isolation region ($N_{\text{track}}^{\text{iso}}$): number of τ_{had}-associated tracks in the isolation region.

- Track radius (R_{track}): the p_T-weighted angular distance of all charged tracks to the reconstructed center of the hadronic tau cone in the core and isolation regions.

- Maximum ΔR (ΔR_{Max}): the ΔR between the reconstructed center of the τ_{had} cone and the the core region track with highest angular separation to it.

- Transverse flight path significance (S_T^{flight}): the decay length of the secondary vertex reconstructed from the core tracks associated with the τ_{had} decay divided by its estimated uncertainty.

- Leading track IP significance ($S_{\text{leadtrack}}$): the transverse impact parameter of the highest-p_T track with respect to the primary tau vertex divided by its estimated uncertainty.

- Track mass (m_{track}): the invariant mass from the sum of all tracks in the core and isolation regions, assuming the tracks have the mass of a charged pion.

- Track-plus-π^0-system mass ($m_{\pi^0+\text{track}}$): similar to m_{track} but also including all π^0 mesons reconstructed in the core region.

- Ratio of track-plus-π^0-system p_T ($p_T^{\pi^0+\text{track}}/p_T$): ratio of the transverse momentum estimated using both tracks and π^0's to the p_T measured using only the calorimeter information.

Not all variables are used for both 1-track and 3-track τ_{had}. Table A.1 summarizes which variables are used for each prong type.

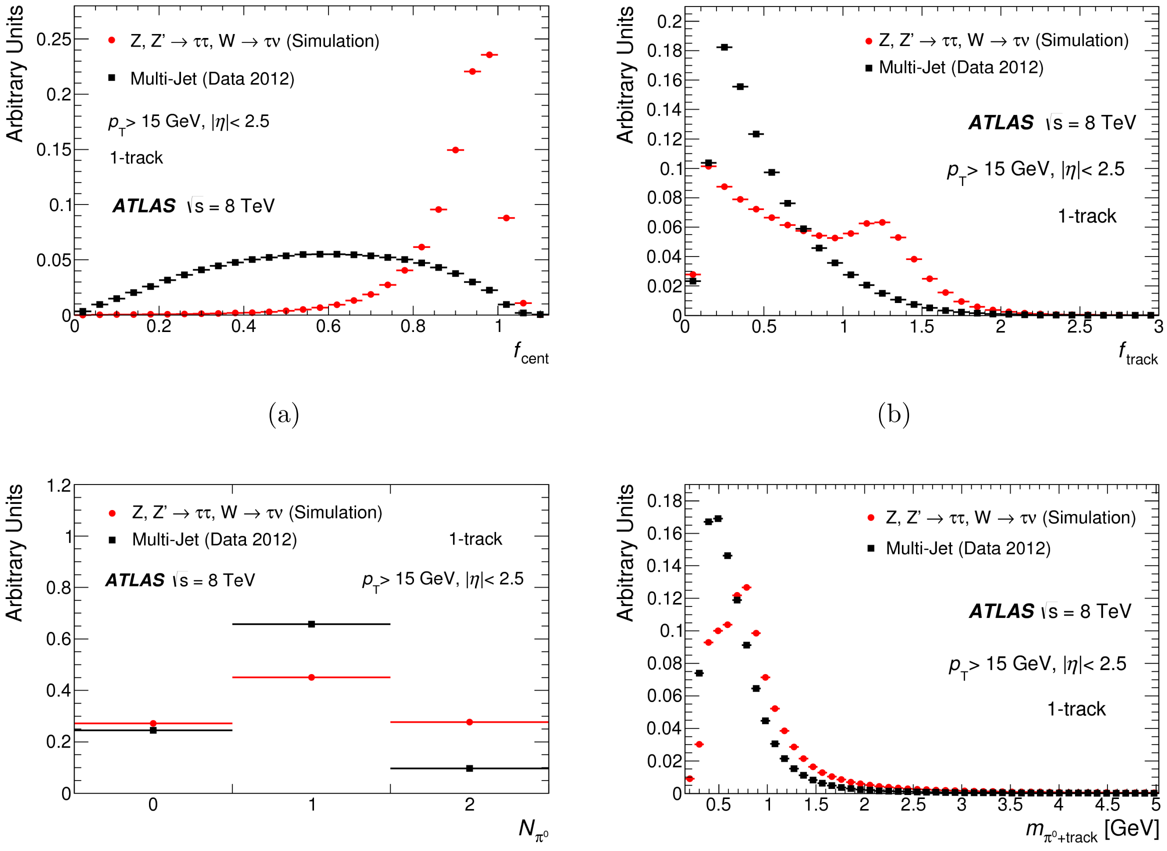

(a)

(b)

(c)

(d)

Figure A.2: Distributions of the variables used in the training of the Run-1 TauID classifier of 1-track hadronic taus.

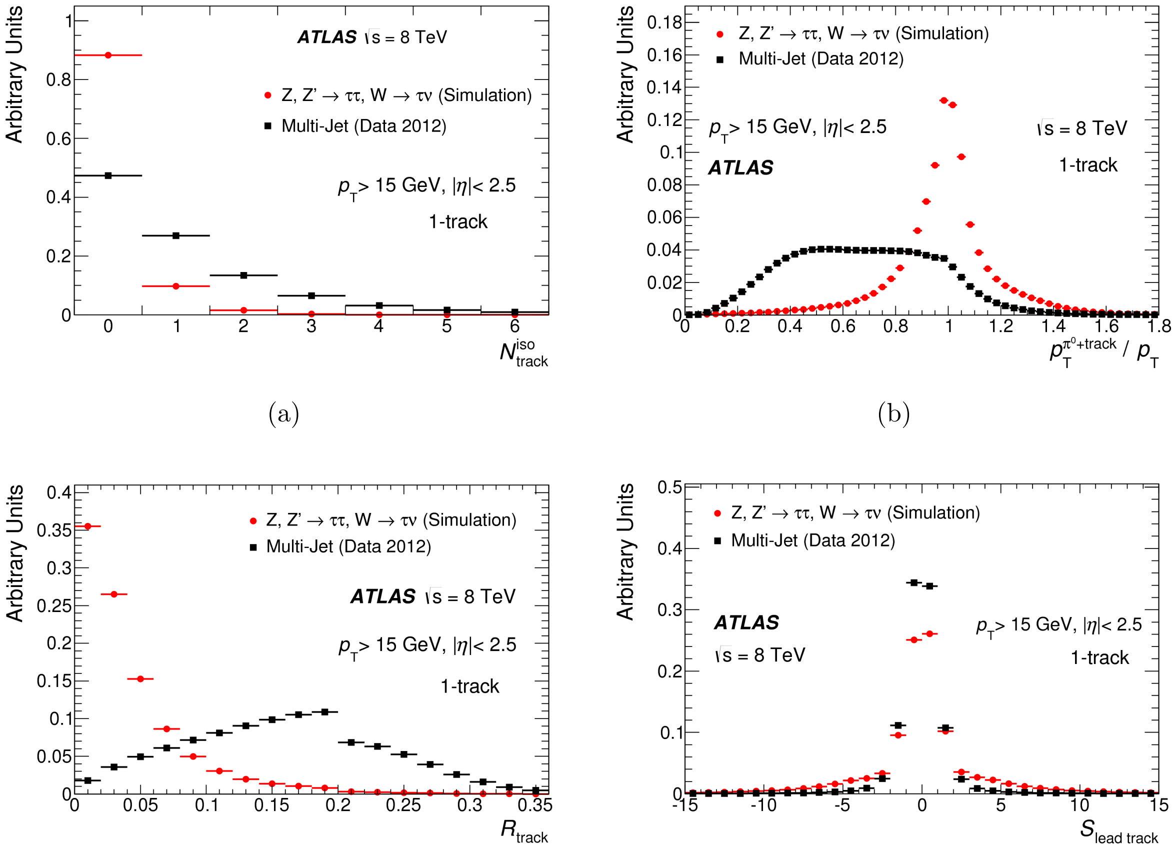

(a)

(b)

(c)

(d)

Figure A.3: Distributions of the variables used in the training of the Run-1 TauID classifier of 1-track hadronic taus.

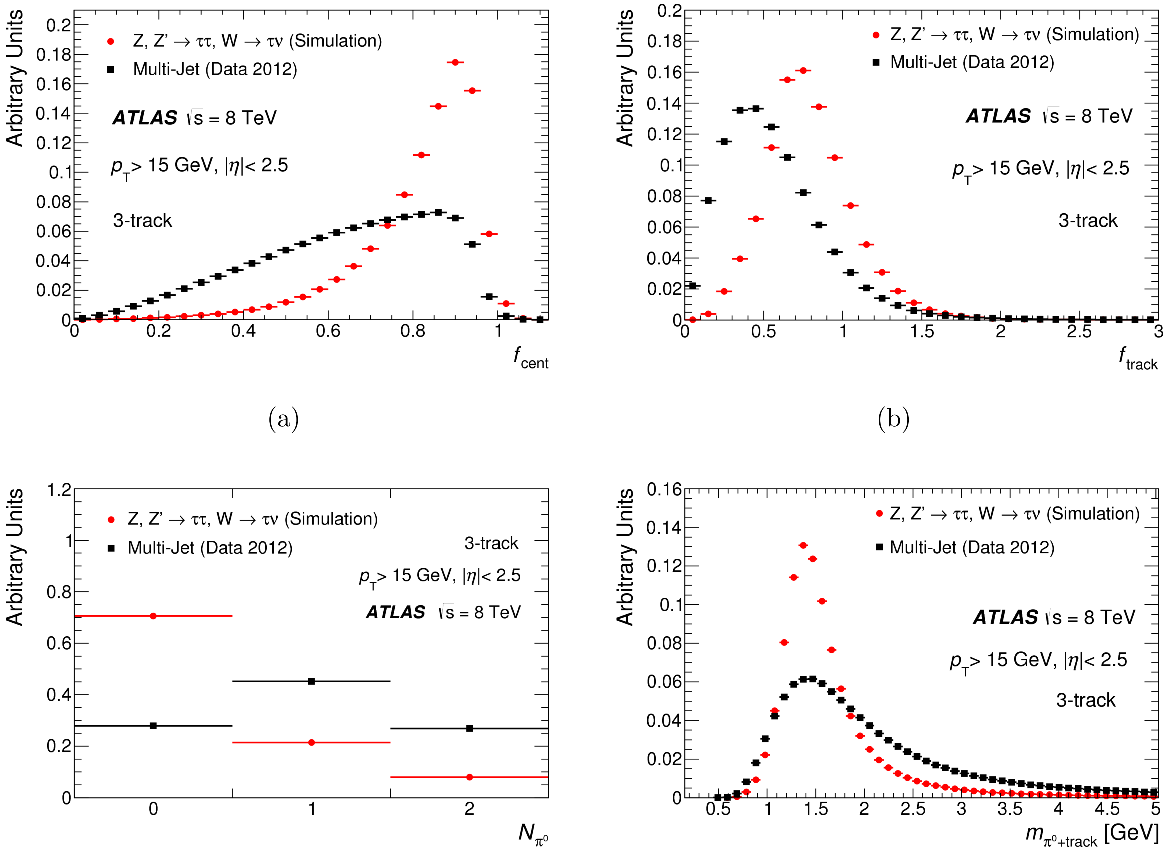

(a)

(b)

(c)

(d)

Figure A.4: Distributions of the variables used in the training of the Run-1 TauID classifier of 3-track hadronic taus.

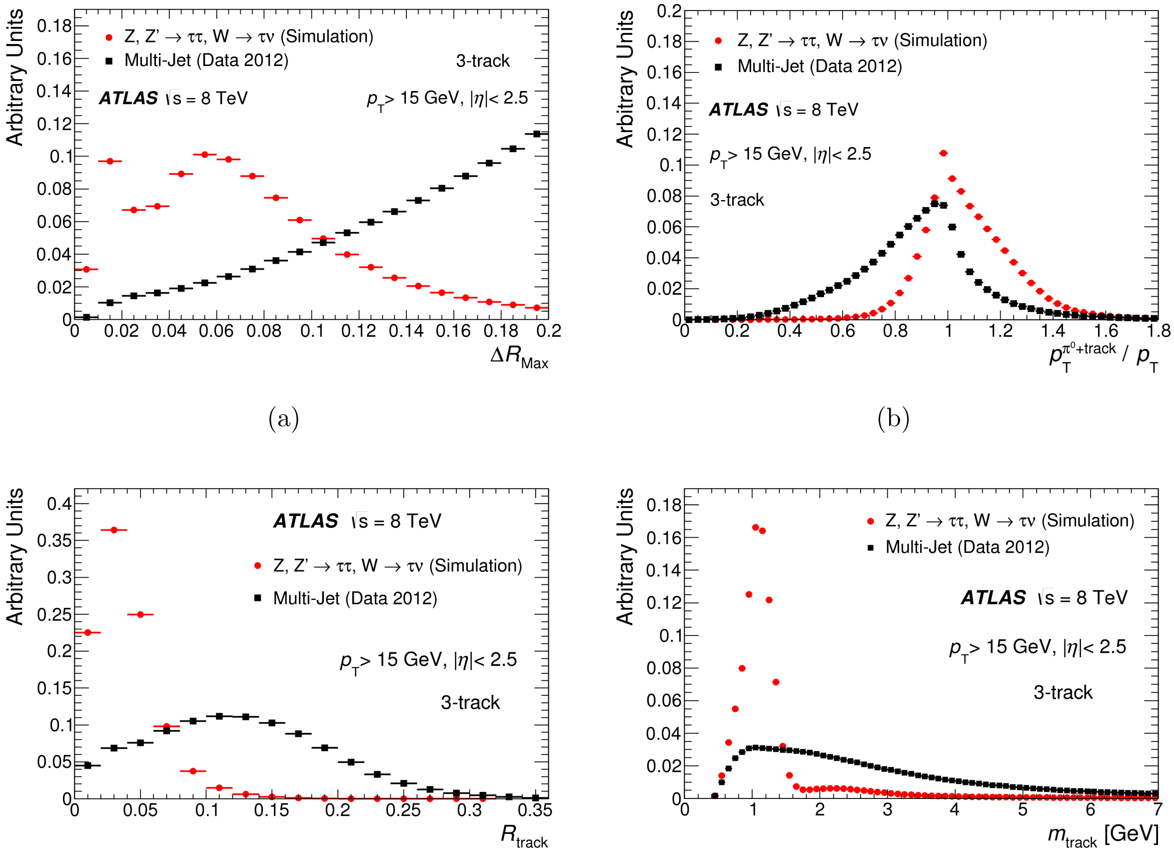

(a)

(b)

(c)

(d)

Figure A.5: Distributions of the variables used in the training of the Run-1 TauID classifier of 3-track hadronic taus.

Variable	1-track	3-track
f_{track}	●	●
f_{cent}	●	●
$S_{leadtrack}$	●	
N^{iso}_{track}	●	
R_{track}	●	●
ΔR_{Max}		●
S_T^{flight}		●
m_{track}		●
$p_T^{\pi^0+\text{track}}/p_T$	●	●
$m_{\pi^0+\text{track}}$	●	●
N_{π^0}	●	●

Table A.1: The list of variables used by the Run-1 TauID algorithm. The bullets indicate whether the variable is used in the training of the 1-track and/or 3-track classifier.

A.3 Final Performance and Working Points

Hadronic taus produced at the LHC have a large range of transverse momentum. Because the τ_{had} properties are correlated with p_T, using a single cut on the BDT score distribution would lead to a corresponding p_T-dependent selection efficiency of the classifier. However, it is often more convenient to have an identification requirement with constant signal efficiencies, so that analyses can have predictable signal acceptances across their region of interest. To achieve this, three working points representing different signal acceptance (and background rejection) profiles are defined (in order of higher to lower signal acceptance): "loose", "medium" and "tight", with identification eficiencies of 65% (70%), 55%(60%), 35%(40%) for 1-track (3-track) hadronic taus, shown in Figure A.6. The final performance of the Run-1 TauID classifier is shown in Figure A.7.

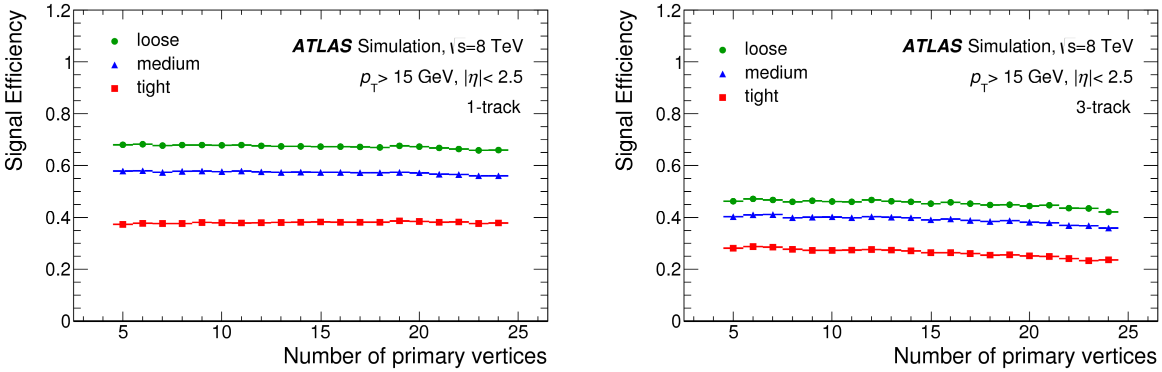

(a) (b)

Figure A.6: The signal efficiency as a function of the reconstructed number of primary vertices for 1-track (a) and 3-track (b) hadronic taus.

A.4 Updates for Run-2

The TauID used in early Run-2 analysis is very similar to the Run-1 tuning. Because not enough data was collected, the classifier is still trained on Run-1 data. The main difference is

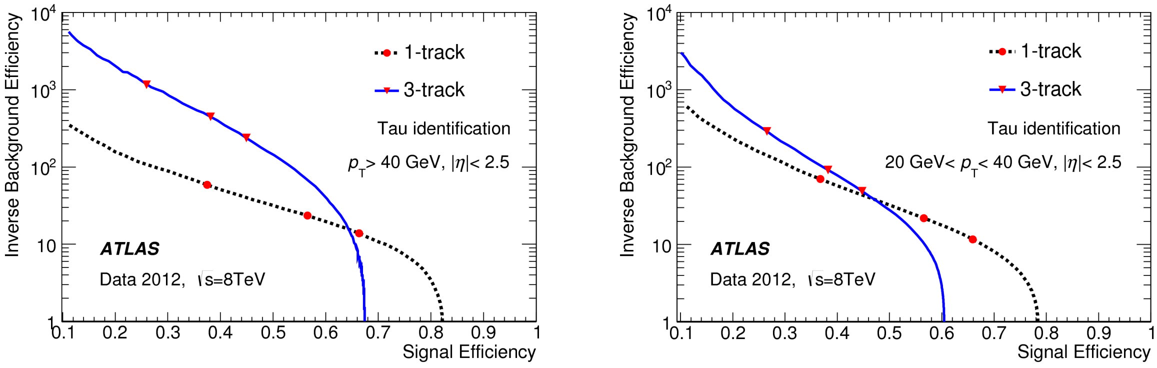

(a) (b)

Figure A.7: The background rejection as a function of the signal efficiency for low ($p_T < 40$ GeV) and high ($p_T > 40$ GeV). transverse momenta hadronic taus. Red markers indicate the three efficiency working points described in the text.

that variables defined using reconstructed π^0's were replaced with variables that contain the explicit low-level cluster energy information that were previously used in π^0 identification. These new low-level variables are:

- $E^{EM}_{\pi^\pm}/E^{EM}$: the ratio of the EM calorimeter clusters associated with charged tracks to the total total energy in the EM calorimeter associated with the tau decay.

- p_T^{EM}/p_T^{tracks}: the ratio of the transverse momentum reconstructed in the EM calorimeter divided by the transverse momentum of the track system.

The final performance was very similar to the Run-1 TauID. However, the new configuration is more flexible since it does not depend on a separate substructure algorithm to incorporate the neutral pion information.

Appendix B

STATISTICAL TREATMENT OF RESULTS

This Appendix aims to summarize the statistical methods used in interpreting the search results presented in this thesis. For a more detailed review, see Ref. [81]. The parameter of interest in both searches is the signal strength μ, given by the ratio of the fitted signal production cross section times branching ratio to its counterpart value predicted by the signal model being tested. Thus, the case $\mu = 0$ corresponds to signal events being absent, while $\mu = 1$ suggests a signal presence that is compatible with the assumption under study. The statistical compatibility of the result with different μ assumptions is done via a binned likelihood function from the product of Poisson probability terms. The different uncertainties are incorporated as nuisance parameters with gaussian distribution functions. Specifically, the likelihood for the signal strength μ is:

$$\mathcal{L}(\mu, \boldsymbol{\theta}) = \prod_{j=\text{bin and channel}} \mathcal{F}_P(N_j|\mu \cdot s_j(\boldsymbol{\theta}) + b_j(\boldsymbol{\theta})) \prod_{\theta_i} \mathcal{F}_G(\theta_i|0,1), \tag{B.1}$$

where the terms in the equation above are:

- the number of observed events in bin j of the m_T^{tot} distribution N_j;
- the number of *expected* signal and background events s_j and b_j;
- the Poisson distribution $\mathcal{F}_P(N_j|\mu \cdot s_j + b_j)$ of N_j events with mean $\mu \cdot s_j + b_j$;
- the nuisance parameter vector $\boldsymbol{\theta}$;
- the gaussian distribution $\mathcal{F}_G(\theta_i|0,1)$ of the nuisance parameter θ_i, with mean 0 and variance 1.

In case no excess of events is observed with regards to the background prediction, upper limits on the production cross section times branching ratio of the signal process being searched for are set. To derive this upper limit, the test statistic $\tilde{q}_\mu$ is defined:

$$\tilde{q}_\mu = \begin{cases} -2\ln(\mathcal{L}(\mu, \hat{\hat{\theta}}(\mu))/\mathcal{L}(0, \hat{\hat{\theta}}(0))) & \text{, if } \hat{\mu} < 0 \\ -2\ln(\mathcal{L}(\mu, \hat{\hat{\theta}}(\mu))/\mathcal{L}(\hat{\mu}, \hat{\theta})) & \text{, if } 0 \leq \hat{\mu} \leq \mu \\ 0 & \text{, if } \hat{\mu} > \mu \end{cases}$$

where $\mathcal{L}(\mu, \theta)$ denotes the binned likelihood function, μ is the parameter of interest (i.e. the signal strength parameter), and θ are the nuisance parameters. The pair $(\hat{\mu}, \hat{\theta})$ corresponds to the global maximum of the likelihood, while $(x, \hat{\hat{\theta}})$ corresponds to a maximum in which $\mu = x$. Similarly, the nuisance parameters that maximize the likelihood in the absence of signal or for a certain value of μ are denoted by $\hat{\theta}(0)$ and $\hat{\theta}(\mu)$, respectively. Thus, the test statistic compares the likelihood at a certain μ value to either the likelihood global maximum (if $\hat{\mu}$ is positive) or to the null hypothesis likelihood (if $\hat{\mu}$ is negative). Signal strengths smaller than the global maximum value can never be excluded. If some excess of events is observed, a similar test statistic is defined:

$$q_0 = \begin{cases} -2\ln(\mathcal{L}(0, \hat{\hat{\theta}})/\mathcal{L}(\hat{\mu}, \hat{\theta})) & \text{if } \hat{\mu} \geq 0, \\ 0 & \text{if } \hat{\mu} < 0. \end{cases}$$

In this case the test statistic measures how compatible the null hypothesis is to the signal strength that maximizes the likelihood.

In order to exclude a hypothesis based on the observed data, the p-value must be calculated. The p-value is the probabilty of obtaining an equal or more extreme outcome were the experiment to be repeated a large number of times. To reject signal hypotheses at 95% confidence-level, we must find μ^{upper} such that

$$p_\mu = \int_{\tilde{q}_\mu, obs}^{\infty} f(\tilde{q}_\mu | \mu, \theta) d\hat{q}_\mu = 5\%, \tag{B.2}$$

where $f(\hat{q}_\mu | \mu, \hat{\hat{\theta}}(\mu, \text{obs}))$ is the probability distribution function (*pdf*) for a test statistic $\tilde{q}_\mu$. However, it is possible that a downward fluctuation of the data causes μ^{upper} to become very small, beyond the sensitivity of the analysis being conducted. This problem is solved by using the modified frequentist approach known as `CL`$_S$ [78]. The `CL`$_S$ method uses the p-value ratio

$$p'_\mu \equiv \frac{p_\mu}{1 - p_b}, \tag{B.3}$$

where p_b is the p-value for the same test statistic but assuming a background-only hypothesis

$$p_b \equiv \int_{\tilde{q}_\mu,\mathrm{obs}}^{\infty} f(\tilde{q}_\mu | 0, \hat{\hat{\theta}}(\mu = 0, \mathrm{obs})) d\tilde{q}_\mu. \tag{B.4}$$

We can also interpret the results directly in terms of the signal models under consideration. This is done by computing the signal predictions for each point of the 2HDM and MSSM planes and checking that they are still allowed by the upper limits that were just set.

It is important to note that it is not necessary to conduct a large number of pseudo-experiments in order to get a probability distribution for the test statistic. It can be shown that for sufficiently large data samples, the likelihood ratios that appear in the definitions of the test statistic converge to specific analytical forms [82]. This result is called the *asymptotic approximation*, and has been used in both searches presented in this thesis. For illustration purposes, we write the asymptotic form of the *pdf* $f(\tilde{q}_\mu|\mu)$:

$$f(\tilde{q}_\mu|\mu) = \frac{1}{2}\delta(\tilde{q}_\mu) + \begin{cases} \frac{1}{2\sqrt{2\pi}} \frac{e^{-\tilde{q}_\mu/2}}{\sqrt{\tilde{q}_\mu}} & \text{if } 0 < \tilde{\mu} \leq \mu^2/\sigma^2, \\ \frac{1}{2\sqrt{2\pi}\sigma} \exp[-(\frac{\tilde{q}_\mu + \mu^2/\sigma^2)^2}{2(2\mu/\sigma)^2}] & \text{if } \tilde{q}_\mu > \mu^2/\sigma^2, \end{cases} \tag{B.5}$$

where σ is the variance of $\hat{\mu}$.

It is also useful to check the impact of the nuisance parameters on the likelihood fit. This is done by checking the shift in the signal strength, $\Delta\hat{\mu}$, due to $\pm 1\sigma$ variations of each nuisance parameter. Confirming that the fitted nuisance parameter values are compatible with their pre-fit assumptions is also a good indication that the systematic uncertainties used are adequate. Two typical fit scenarios are considered: an *unconditional* fit where μ is allowed to float, and a *conditional* fit where $\mu = 1$. The former allows one to find the signal strength that is most compatible with the observed data, while the latter allows one to see how the nuisance parameters change to accommodate the signal assumption. Figures B.1-B.3 show nuisance parameter rankings for the $A \to Zh \to \tau\tau$ and MSSM Higgs to ditau searches. The parameters are ranked according to their impact on $\hat{\mu}$, and black markers indicate the deviations of the fitted parameter values from their initial assumptions.

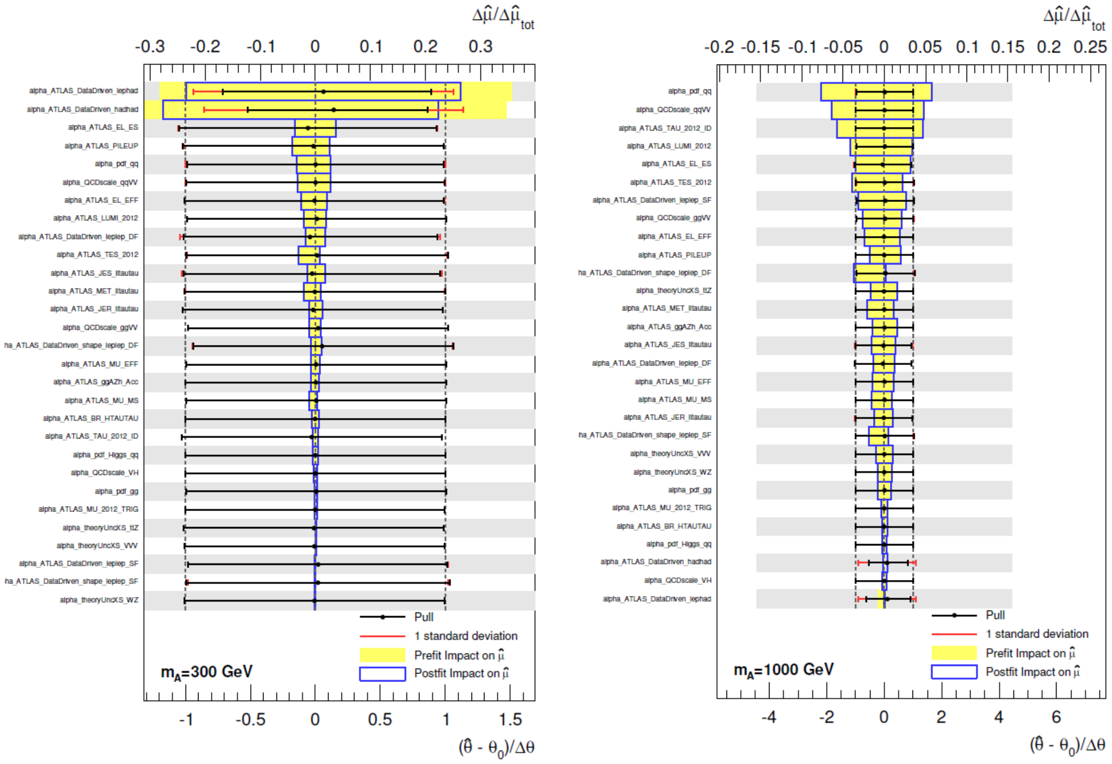

(a)

(b)

Figure B.1: Nuisance parameter rankings of the combined $A \to Zh \to \ell\ell\tau\tau$ search for signal mass hypothesis of 300 (a) and 1000 (b) GeV.

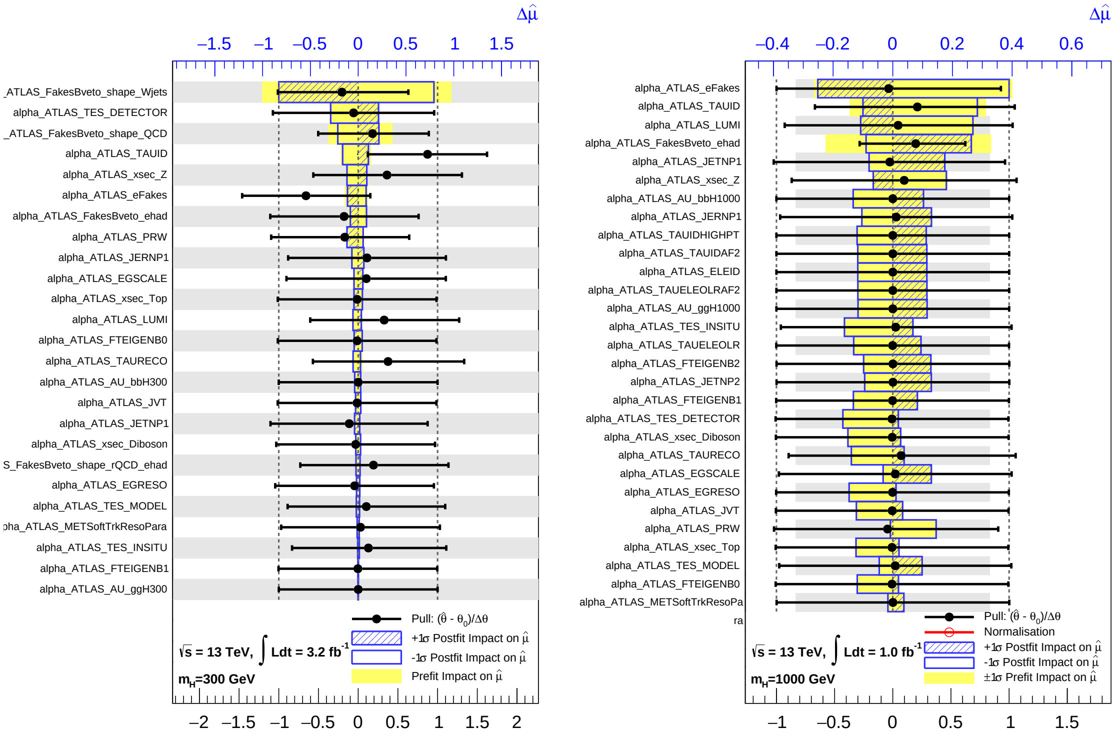

(a) (b)

Figure B.2: Nuisance parameter rankings in the MSSM $H/A \to e\tau_{had}$ channel for signal mass hypothesis of 300 (a) and 1000 (b) GeV.

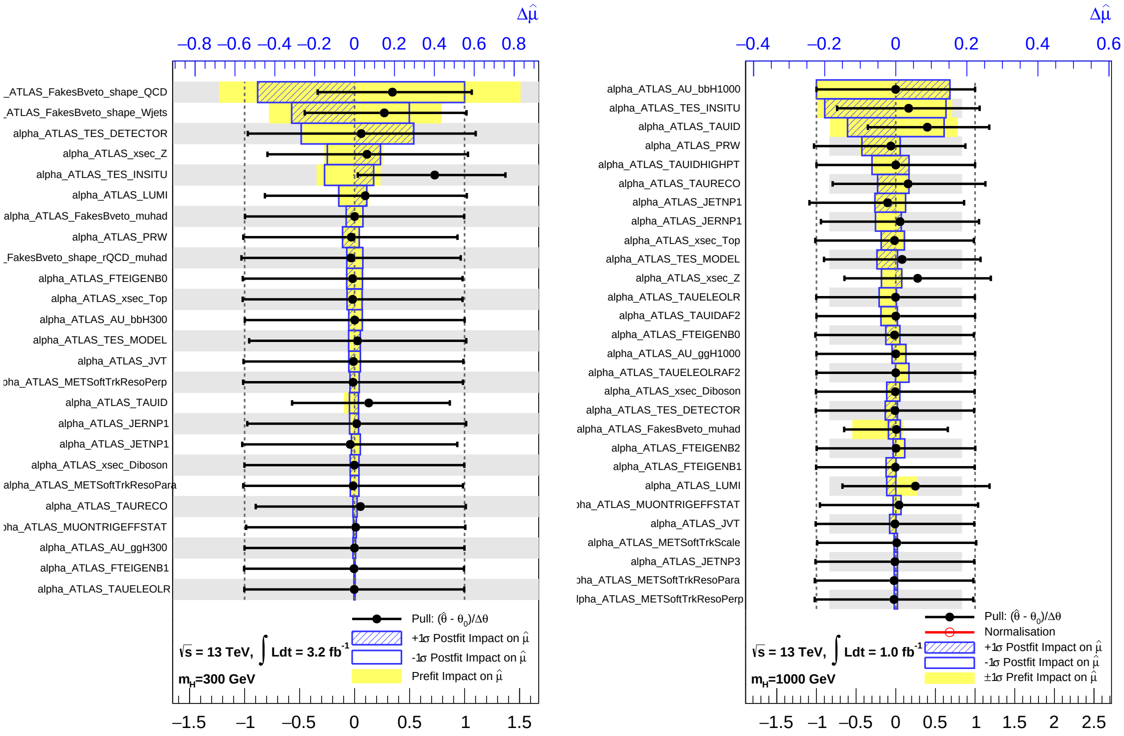

(a) (b)

Figure B.3: Nuisance parameter rankings in the $H/A \to \mu\tau_{had}$ channel for signal mass hypothesis of 300 (a) and 1000 (b) GeV.